Advanced Space Concepts Laboratory
Department of Mechanical and Aerospace Engineering
Faculty of Engineering
University of Strathclyde

Attitude Dynamics and Shape Control of Reflectivity Modulated Gossamer Spacecraft

Andreas J. Borggräfe

Submitted in fulfilment of the requirements for the degree of

Doctor of Philosophy

2015

This thesis is the result of the author's original research. It has been composed by the author and has not been previously submitted for examination which has led to the award of a degree.

A. Borggräfe

Andreas Jürgen Borggräfe
Glasgow, Scotland, April 2015

To my parents, who...

always saw potential, not obstacles
paved ways, where none existed, and
found words, whenever needed.

and

To my brother

who rarely complains about being
my closest friend.

Supervisors

Professor Colin R. McInnes
Advanced Space Concepts Laboratory, University of Strathclyde
Glasgow, United Kingdom

Dr. James D. Biggs
Advanced Space Concepts Laboratory, University of Strathclyde
Glasgow, United Kingdom

Additional Supervision:

Dr. Matteo Ceriotti
School of Engineering, University of Glasgow
Glasgow, United Kingdom

Dr. Jeannette Heiligers
Advanced Space Concepts Laboratory, University of Strathclyde
Glasgow, United Kingdom

Examiners

Professor Matthew P. Cartmell
Department of Mechanical Engineering, University of Sheffield
Sheffield, United Kingdom

Professor Massimiliano Vasile
Advanced Space Concepts Laboratory, University of Strathclyde
Glasgow, United Kingdom

"Two roads diverged in a wood, and I -
I took the one less travelled by,
And that has made all the difference."
– Robert Frost

Acknowledgement

Doing a Ph.D. in a different country truly is a challenge of its own for every early-stage career researcher. Being given the opportunity to research in Scotland at the University of Strathclyde, however, was the journey of a lifetime. From the beginning, the single most important element to make this journey a success were the outstanding researchers, colleagues, and friends, who I met along the way.

First of all, I wish to thank Professor Colin McInnes, for inviting me on this fantastic journey in the first place, and for his excellent supervision during my time in Glasgow. Colin, your guidance and imagination has been key to the successful completion of my thesis. Your visionary thinking is targeted towards building an innovative better future and will always be a great source of inspiration. Furthermore, I want to express my gratitude to Dr. Matteo Ceriotti, who I first met during a conference in New York in 2010. Matteo, your insights, knowledge and creative ideas have been invaluable for my progress, as well as your experience as a lecturer during my teaching time at the University of Glasgow. I would also like to thank Dr. Jeannette Heiligers, for her steady support and advice, which has helped me so much in developing my career as a researcher. Jeannette, working together with you desk-to-desk and our daily lunch breaks will truly be missed!

It has been a privilege to work with all of you over the past four years.

I would also like to thank Dr. James Biggs for his helpful advice and for the fruitful discussions we had, both in the office and in the pubs in Glasgow. My thanks also go to Professor Massimiliano Vasile, Professor Matthew Cartmell and Professor Donald Mackenzie for providing such a welcoming atmosphere and constructive feedback during my Viva.

Many thanks to all my colleagues and friends at the Advanced Space Concepts Laboratory, Dr. Daniel García Yárnoz and Dr. Garrie Mushet, who participated in this journey with me, making it a truly unforgettable time! In addition, my thanks go to Dr. Joan-Pau Sanchez Cuartielles, Dr. Camilla Colombo, Dr. Giorgio Mingotti, Dr. Thomas Sinn, Dr. Marcel Düring, Dr. Marta Ceccaroni, Dr. Charlotte Lücking, Dr. Russell Bewick, Dr. Pamela Anderson, and Dr. Giuliano Punzo; what an exquisite bunch of extremely capable researchers! Furthermore, I would like to thank all the members of staff at the Department of Mechanical & Aerospace Engineering, namely, Katrina May and Aileen Petrie, for their support and welcoming working atmosphere each day.

I would like to acknowledge the European Research Council, which funded my Ph.D. through the Advanced Investigator Grant - 227571: VISIONSPACE: Orbital Dynamics at Extremes of Spacecraft Length-Scale. Additionally, I would like to thank all organisations and institutions that provided conference funding and enabled me to disseminate my research. These include the Institution of Mechanical Engineers, the Royal Aeronautical Society, the Parliamentary and Scientific Committee and the Institution of Engineering and Technology.

Finally, I want to thank my parents, Jürgen and Margot, and my brother Michael, simply for believing in me. You probably have no idea how much this has made all the difference.

Andreas Borggräfe
Noordwijk, The Netherlands
July 2015

Abstract

The utilisation of space provides many opportunities to deliver pioneering innovations during the 21$^{\text{st}}$ century. One of these opportunities is the gossamer spacecraft, an emerging technology to achieve very low mass, large area and low stowage volume. Examples include large ultra-lightweight membrane reflectors and distributed tethered formations. Gossamer spacecraft offer the potential to deliver innovative new science and applications missions to aid our growing globalised societies: high-performing communications antennae, scientific telescopes and space-based solar power collectors. However, the ability to control such large structures in space is essential for their successful operation. To this aim, this thesis investigates a novel means to control large gossamer spacecraft by exploiting modulated solar radiation pressure (SRP), thus by modifying the nominal light pressure acting on the structure in space.

Various concepts have been proposed in the past to control the attitude of a gossamer spacecraft, employing complex mechanical systems or thrusters. Furthermore, methods to control the surface shape of a large membrane reflector using, for example, piezoelectric actuators, are being developed. Since on-board control systems need to be high-performance, reliable and importantly lightweight, this thesis investigates the use of thin-film reflectivity control devices across the spacecraft surface. Controlling the reflectivity modulates the Sun's light pressure acting on a thin membrane thus controlling its shape. In addition, body forces and torques become available to control the attitude of such a large structure 'optically', without using traditional mechanical systems.

The concept is demonstrated first by controlling a two-mass tethered formation in a Sun-centred orbit, showing that the spacecraft attitude can be stabilised around new equilibria created by controlling the surface reflectivity of the masses. Subsequently, the concept is applied to control the attitude of a large membrane reflector, which confirms the viability of reflectivity modulation by generating variable optical torques in the membrane plane. In particular, the nominal SRP forces are modified by introducing different surface reflectivity distributions across the membrane. It is shown that through these optical torques, the reflector can be steered, for example, to a Sun-pointing attitude from an arbitrary initial displacement. The analysis also considers the variation of the SRP force magnitude with changing light incidence angle towards the Sun during the manoeuvre, thereby presenting solutions to a challenging attitude control problem.

Furthermore, by adopting a highly-integrated multi-functional design approach, the concept of reflectivity modulation is also employed to control the surface shape of a large membrane reflector. First, the nominal (non-parabolic) deflection shapes due to uniform SRP across the surface are presented. Subsequently, a closed-form solution for the reflectivity function across the membrane required to create a true parabolic deflection shape is derived. In order to improve the quite large focal lengths of the deflected shapes that can be generated for a tensioned membrane, shape control of a slack suspended surface is also considered. The achievable (shorter) focal lengths support the feasibility of exploiting modulated SRP for controlled surface deflection.

In summary, this thesis demonstrates the potential of using surface reflectivity modulation to control the attitude and morphology of large gossamer spacecraft without using complex mechanical systems or thrusters. Therefore, the concept of optical control represents a major step towards highly-integrated adaptive gossamer structures and supports the development of this promising key-technology to deliver advanced space applications.

Contents

List of Symbols and Acronyms

Acronyms

AU	astronomical unit
BC	boundary condition
BVP	boundary value problem
c.m.	centre-of-mass
c.p.	centre-of-pressure
DES	differential equation system
EAP	electroactive polymer
EOM	equations of motion
FEM	finite element method
GEO	geostationary orbit
GG	gravity gradient
IAE	Inflatable Antenna Experiment
IKAROS	Interplanetary Kite-craft Accelerated by Radiation Of the Sun
IVP	initial value problem
JAXA	Japanese Aerospace Exploration Agency
JPL	Jet Propulsion Laboratory
JWST	James Webb Space Telescope
LEO	low earth orbit
MEMS	micro-electro-mechanical systems
MFC	macro-fibre composite
NASA	National Aeronautics and Space Administration
PV	photovoltaic

PVDF	polyvinylidene fluoride
PZT	piezoceramic lead zirconate titanate
RF	radio-frequency
RKN	Runge-Kutta Nyström
SAR	synthetic aperture radar
SPS	solar power satellite
SRP	solar radiation pressure
TRL	technology readiness level
TSS	tethered satellite system

Greek Symbols

α	cone angle
$\tilde{\alpha}$	absorptivity
β	lightness number
γ	attitude angle
δ	clock angle
ϵ	emissivity
ϵ_{k}	eigenvalues
η	angular size
θ	attitude angle
κ	mass ratio
λ	tether length ratio
μ	solar gravitational parameter
$\tilde{\mu}$	effective solar gravitational parameter
$\mu_{\oplus}$	Earth's gravitational parameter
ν	true anomaly
$\boldsymbol{\nu}$	cartesian ν-axis vector
ν	Poisson ratio (Chapter 5)
ξ	non-dimensional radial position
ρ	surface reflectivity coefficient
σ	tensile stress
σ_{lim}	ultimate tensile strength

τ	material density
$\tilde{\tau}$	transmittance
φ	local pitch angle
χ	non-dimensional deflection rate
ω_0	nominal orbital rate
$\tilde{\omega}_\mathrm{i}$	effective orbital rate
$\boldsymbol{\omega}$	angular velocity vector
ω_D	disk/hoop spin rate

Roman Symbols

a_0, a_1, a_2	function coefficients
a, b	boundary line coefficients
$a_\mathrm{G}, c_\mathrm{G}$	gravitational deflection curve coefficients
$a_\mathrm{p}, b_\mathrm{p}, c_\mathrm{p}$	parabolic deflection curve coefficients
a_SRP	SRP force coefficient
A, B, C	coefficients
$\mathbf{a}$	Euler axis of rotation
A	area
A_f	area in focal plane
b_w	beam width
c	speed of light
c_1, c_2, C_p	integration constants
C_CF	centrifugal force coefficient
C_n	number of reflectivity combinations
C_r	light concentration ratio
d_S	Sun diameter
D	flexural rigidity (Chapter 5)
D	hoop diameter
E	Young's modulus
f	focal length
$\mathbf{F}$	force vector
$\mathbf{g}$	force field vector

g	gravitational acceleration
$\mathbf{G}$	gravitational force vector
h	string depth
$h_{\oplus}$	Earth orbit altitude (previously h)
H	Hamiltonian
i	electro-chromic cell (element) number
$\mathbf{i}, \mathbf{j}, \mathbf{k}$	Cartesian basis vectors
$[I]$	inertia tensor
$I = [a, b]$	integration interval
$I_{\mathrm{xx}}, I_{\mathrm{yy}}, I_{\mathrm{zz}}$	principal mass moments of inertia
$[J]$	Jacobian matrix
k	initial tension parameter
K	kinetic energy
l	tether length
L	Lagrangian (Chapter 3)
L	edge length
L_1	Lagrange point
m	mass
M	total mass
M_{B}	central mass
$[M]$	electro-chromic cell matrix
n	number of electro-chromic cells per side
N	total number of electro-chromic cells
$\mathbf{n}$	normal vector
N_r	radial in-plane tension
N_θ	circumferential in-plane tension
N_0	initial in-plane tension
p_{j}	generalised momentum
p	generic pressure
p_{SRP}	solar radiation pressure
P_{SRP}	non-dimensional solar radiation pressure
$\bar{p}_0$	scaled solar radiation pressure

p_0	solar radiation pressure at 1 AU
P_ω, P_q	proportional gains
q_j	generalised coordinate
$\bar{q}$	attitude quaternion vector
r	radial position
$\mathbf{r}$	cartesian r-axis vector
R	circular orbit radius (Chapter 3 and 4)
R	circular membrane/hoop radius
R_S	solar distance
$\mathbf{R}_\oplus$	Earth radial direction
$r_\oplus$	Earth radius
$\mathbf{R}, \mathbf{R}_1, \mathbf{R}_2$	position vectors
s	string length
S	total slack string length
S_r	non-dimensional radial tension
S_θ	non-dimensional circumferential tension
t	thickness
t	time (Chapter 3 and 4)
$\mathbf{T}_\mathrm{SRP}$	SRP torque vector
T	string tension force (Chapter 6)
V	potential energy
$\mathbf{w}$	vertical w-axis vector
w	vertical out-of-plane deflection
w_c	central deflection
W	non-dimensional out-of-plane deflection
W_S	solar energy flux (renamed from W, Ch. 2)
$\mathbf{x}$	cartesian x-axis vector
x	coordinate along x-axis
$\mathbf{X}$	cartesian X-axis vector
$\mathbf{y}$	cartesian y-axis vector
y	coordinate along y-axis
$\mathbf{Y}$	cartesian Y-axis vector

$\mathbf{z}$	cartesian z-axis vector
z	coordinate along z-axis

Subscripts

$\oplus$	Earth
0	at initial/mean value
b	back
BL	boundary line
c	constrained
CF	centrifugal
d	diffuse
dec	decoupled
err	error
eq	equilibrium
E	Ecliptic
final	final value
G	gravity
lim	threshold
p	parabolic
P	Pressure
ref	reference value
req	required
rot	rotational
s	specular
S	Sun
SRP	solar radiation pressure
tot	total
transl	translational

Superscripts

$*$	optimal/scaled

Other Symbols and Notations

Δ	difference
∇	vector differential operator
$\hat{\square}$	unit vector
$\dot{\square}$	first time derivative of $\square$
$\square'$	first derivative of $\square$ w.r.t. position
$\bar{\square}$	quaternion vector
∂	partial (derivative)
$\otimes$	quaternion product operator
$\mathcal{B}$	body-fixed Cartesian reference frame $(\mathbf{x}, \mathbf{y}, \mathbf{z})$
$\mathcal{E}$	ecliptic reference frame $(\mathbf{x}_\mathrm{E}, \mathbf{y}_\mathrm{E}, \mathbf{z}_\mathrm{E})$
$\mathcal{I}$	Sun-centred inertial reference frame $(\mathbf{X}, \mathbf{Y})$
$\mathcal{O}$	rotating orbit reference frame $(\mathbf{r}, \nu)$

List of Figures

List of Tables

Chapter 1

Introduction

In this first chapter, the scientific framework and the research objectives of the thesis will be defined. The development of large gossamer space structures as an architecture for a range of space-based applications will be discussed in Section 1.1, in the context of the limitations and challenges of this technology to date. The section will highlight envisaged space-based applications, give a brief description of the required key technologies, and review current methods for control. This discussion is then used to define the research objectives in Section 1.2. The contributions of this thesis will be highlighted in Section 1.3, while Section 1.4 will provide an overview of published work. Finally, in Section 1.5, an outline of the thesis will be presented.

1.1 Large gossamer spacecraft

Since the early days of human flight, the fundamental challenge has been to achieve ultra-lightweight designs to reach beyond the sphere of our planet. Besides the goal of becoming 'lighter-than-air', as first seen in Chinese hot-air balloons ('sky lanterns') in the 3rd century B.C., pioneering inventors such as Otto Lilienthal and the Wright brothers based their designs on wooden trusses, bracing tethers and fabric surfaces in the early 20th century [1]. In 1971, the first human-powered aircraft to cross the English channel was aptly termed the 'Gossamer Albatross' (see Fig. 1.1). Today, modern aircraft are built with composite materials to reduce weight, while at the same time, meeting the requirements of structural integrity. With the dawn of modern rocketry and spaceflight, early pioneers such as Konstantin Tsiolkovsky and Hermann Oberth knew that propulsive thrust alone could not 'outweigh' the importance of realising low-mass designs.

Figure 1.1: Gossamer Albatross crossing the English Channel in 1971 (image credit: AeroVironment Inc.)

Being synonymous for something thin, delicate, or light, the word ‘gossamer’ relates to the Middle English term ‘goose summer’. At this time of the year in late summer, when geese were sold at local markets, spider ballooning (so-called ‘angel hair’) was at its peak, covering bushes and grass in the setting Sun. Having adopted this analogy, the term ‘gossamer structure’ in modern engineering refers to a category of ultra-low-mass structures in, for example, automotive design, architecture and aerospace technology. Especially in space-related applications, the term ‘gossamer spacecraft’ is commonly referred to as a particular type of spacecraft, which has found considerable interest over the last decades.

In general, gossamer spacecraft are large ultra-light structures envisaged to accomplish a wide range of space-based applications, as will be detailed in Subsection 1.1.1. Uniquely, gossamer space systems provide an opportunity to reduce the high launch volume and launch cost of existing space technologies. Solar sails are a major category of gossamer spacecraft [2], however, they also include deployables such as strings, tethers, booms, and trusses, as well as inflatable or pressurised structures, lenses, antennae and meshes [3]. The largest category of gossamer spacecraft are deployable or inflatable membrane structures. Such membrane reflectors usually consist of a highly-reflective thin film, folded into a packed configuration during lunch. Once delivered into orbit, the membrane is deployed from a support structure to form a large reflecting surface, as shown in Fig. 1.2. The surface can be used to collect and/or emit electro-magnetic radiation for a wide range of applications such as, for example, science, communications,

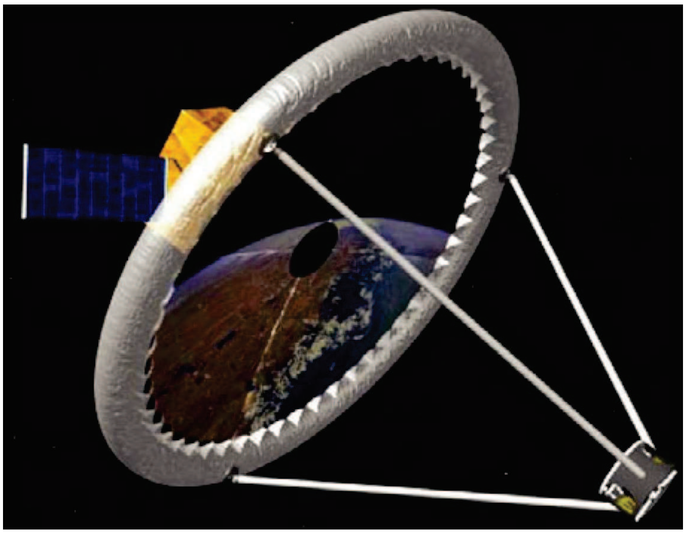

Figure 1.2: Inflatable circular membrane reflector, including subsystems (back) and receiver unit in the aperture focus [4].

and the collection of (solar) energy.

Clearly, increasing the mirror aperture size of existing spacecraft provides significant benefits for Earth observation, scientific telescopes and even surveillance and military utilisation. Space reflectors with diameters of 30 m and more potentially enable more accurate remote sensing, spectroscopy of fainter objects and imaging with higher resolution [4]. However, considering all current and proposed launch technologies, traditional monolithic mirrors above 8 m in diameter are prohibitively large to be delivered into orbit [5]. The only exception are segmented, deployable designs such as the 6.5 m primary mirror of the James Webb Space Telescope (JWST) [6]. To overcome this severe packaging limitation, various flexible mirror configurations such as deployable membrane reflectors, supported by collapsible expandable booms [7, 8] or surrounded by tensioning web cables [9], have been proposed to fulfil this need. Furthermore, membranes supported by inflatable/rigidisable support structures [10] or pressurised lenticular parabolic reflectors [11, 12] are being developed.

Research and development of large, lightweight membrane structures emerged in the late 1950s [13], with the prospect of exploiting their potential to realise low-cost space technology and low stowed volume. Indeed, early flight experiments with large inflatable and/or deployable structures have been conducted since the early 1960s (Echo Balloon) [14]. More recent developments include the in-space demonstration of the 14 m diameter L'Garde 'Inflatable Antenna Experiment' (IAE) in 1996 [15], as shown in Fig. 1.3, and the 12.2×18 m Sun-shield membrane of the JWST. Further examples of inflatable gossamer structures include inflatable solar arrays [16], human habitats [17],

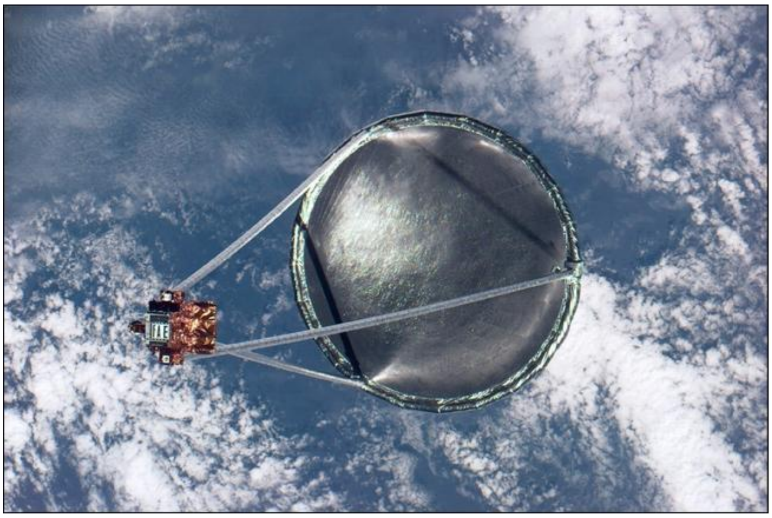

Figure 1.3: L'Garde 'Inflatable Antenna Experiment' (IAE) after deployment in 1996 (image credit: NASA)

and impact systems for planetary landers (Mars Pathfinder) [18]. Typical examples of deployable gossamer systems also include thin-film solar arrays [19] and mesh antennae [20]. A comprehensive review of recent trends in the analysis, experimentation, and control of gossamer spacecraft has been provided in Ref. [21].

Tethered spacecraft configurations are similar to deployable membrane spacecraft, since both are fabricated from continuous material which carries tension loads, but cannot resist compression or shear stresses [13]. Furthermore, both types of gossamer structures are envisioned to be extremely large in surface area or tether length, respectively, while both are being deployed from extremely compact configurations. Almost uniquely, and with the only alternative being a constellation of satellites flying in formation, tethered spacecraft offer an opportunity to considerably improve applications such as radio/optical interferometry [22]. For wavelengths in the sub-millimetre spectrum, for example, a very large telescope with an effective aperture diameter in the kilometre range would be required to obtain high quality angular resolution [23]. However, a tethered configuration could enable much larger (synthetic) aperture diameters for science applications than can practically be achieved by a monolithic mirror/membrane surface. For example, a spin-stabilised tethered system, flying in precise formation, could be employed to collect enough light from distant faint celestial objects. Light collecting mirrors, mounted on separate members of the formation, provide access to kilometre baselines. Slow spin rates then produce a centripetal acceleration, which keeps the tethered arrangement tight, thus maintaining the shape of the formation [24]. In comparison to purely formation-flying concepts, without tethers, this removes the propulsive need for station-keeping [22].

Finally, the concept of a ‘space tether’ was initially introduced by the Russian space pioneer Konstantin Tsiolkovsky in 1895 [25] and reemerged in the 1960s [26] due to its numerous applications in space exploration and exploitation, such as the space elevator [27] and generating artificial gravity during NASA’s Gemini program from 1962-1966 [28]. Several missions have been proposed [29] and launched to verify the concept of space tethers since the 1970s. The coupled orbit/attitude dynamics, stability properties, and the control of tethered satellite systems (TSS) have been extensively studied over recent decades [30, 31, 32]. In particular, the classical dumbbell problem, namely two masses connected by a rigid massless tether, has been discussed extensively, for example in Refs. [33, 34, 35, 36]. A comprehensive review of space tether research has been provided in Refs. [37, 38].

1.1.1 Applications

Ultra-lightweight gossamer structures have been developed with the prospect of accomplishing, or even enabling, compelling new science and application missions. In order to give an overview of the full range of technology applications envisaged for this type of spacecraft, the different space applications will be introduced briefly in this subsection.

Communication

The reflective surface of a gossamer spacecraft can be used as a large antenna for radio-frequency (RF) communications [39]. Although deployable mesh antennae and phased arrays with projected aperture sizes of up to 25 m are already operational for broadcasting and mobile satellite services [20], concepts based on a large parabolic membrane antenna offer several advantages. In particular, antenna efficiency, bandwidth, power consumption, complexity, mass and cost can be improved. Further examples for Earth communication services that may see considerable growth over the next decade include (air) traffic management, but also emergency and disaster management, and communication with the Earth’s high latitudes and polar regions (e.g. science stations, shipping). In terms of space communication, example applications include the support of the Deep Space Network by installing relay-satellites to communicate with the far side of the Moon and the Martian surface, especially during periods of solar occultation.

Remote sensing

This category of applications includes Earth observation as well as observational astronomy and astrophysics using space telescopes [40]. With respect to Earth observation, there is a growing demand for high-resolution imagers for resource and biomass monitoring, climate science and weather analysis, (natural) hazard assessment and disaster management, and even reconnaissance and surveillance. One particular imaging concept is synthetic-aperture radar (SAR), which is a novel form of radar used to create images of objects and landscapes. The SAR concept uses the motion of the antenna over a target region for sequential imaging, providing finer spatial resolution than is possible with conventional beam-scanning radars using a physical aperture antenna [41]. However, SAR satellites require large and long antennae which in turn require a large launcher fairing. The cost for SAR missions could therefore be reduced significantly, if the antenna and its support structure is as large as possible, lightweight and foldable during launch. Possible applications for interferometric SAR include tectonic mapping of seismic activity, volcanism, glacier flow, and sounding of the Arctic and Antarctic ice shields [42]. Membrane reflector spacecraft could achieve similar resolution/accuracy as LEO satellites, while orbiting at much higher altitudes. For example, a single 30 m membrane mirror in a 5000 km equatorial orbit would obtain the same (10 cm) accuracy as current LEO satellites, but could provide full (sub-polar) coverage [43].

Solar power collection

Early studies of solar concentrators for high temperature space power systems have been conducted since the 1960's [44]. Commonly termed 'Solar Power Satellites' (SPS), the idea behind SPS is to collect solar energy in space and transmit a concentrated microwave or laser beam to receivers on Earth [45]. The main advantages are the unobstructed view of the Sun, independent of the day/night cycle, weather or seasons. Furthermore, collecting solar energy above the atmosphere of Earth is more effective than for ground-based photovoltaic (PV) systems due to the attenuation of the solar flux density in the atmosphere.

A solar power collector essentially consists of four parts: (i) a large surface area to collect solar energy, for example via PV cells or a parabolic (membrane) collector, (ii) a subsequent heat engine at the aperture focus, (iii) a system for transmitting power to Earth, and (iv) a ground-based receiver unit [46]. The main disadvantages of SPS are the high launch cost to deliver the required platforms into orbit and the still low technology readiness level (TRL) of the systems involved. For example, the energy beam transmitter on-board and the receiver on Earth must operate such that energy losses are minimal, while at the same time, losses due to transmitting the beam through the atmosphere are inevitable. Further utilisation of the collected energy could be, for example, to heat propellant for in-orbit spacecraft manoeuvres, station-keeping of Earth satellites or even interplanetary propulsion [45].

Sun shield

As noted previously, the large Sun-shield membrane of the JWST is a prominent example of employing large and ultra-lightweight membrane structures for thermal control of space systems. In general, a Sun shield (or 'Sun shade') is a protective surface that blocks, diverts or otherwise reduces some of the Sun's electro-magnetic radiation, preventing it from impinging on a spacecraft or particular (sensitive) subsystems. In the longer term, such devices may also be used above planetary surfaces, thereby reducing solar insolation [47]. In this regard, large deployable membranes are of particular interest towards mitigating global warming through solar radiation management. At the same time, the shades could also be used to produce space solar power, as discussed above.

1.1.2 Technology

In order to realise ultra-low-mass large-area space structures, a variety of materials and technologies have been developed over the last decades. In simulation-based approaches, different models have been developed to predict the behaviour of such structures in space. Several design concepts have also been tested in ground-based experimental campaigns and during in-space technology demonstration missions. This section focusses on the key technologies required to enable reliable, robust, and low-cost operation of gossamer space structures, briefly highlighting current innovations and challenges involved in ongoing developments.

Deployable/inflatable membrane structures

Again, as noted previously, achieving ultra-lightweight designs for gossamer spacecraft poses engineering challenges in terms of low mass deployable or inflatable structures, thin membrane films as well as subsystem miniaturisation.

One of the main drivers to reduce the spacecraft mass is the membrane thickness. In principle, potential candidate materials for gossamer membranes have the following characteristics: high flexibility (low Young's modulus) and low packaging volume, which is commonly found in thin polymer films [13]. While a polymer substrate is required to provide adequate tensile strength for handling during manufacture, packing and deployment, the final membrane is usually vapour coated on one or both sides with Aluminium. The metal improves the resistance of the film to thermal loads and radiation in the space environment, as well as providing a greater resistance to atomic oxygen in LEO. Furthermore, the coating realises a smooth reflective surface with low surface roughness. One of the earliest materials used in space-related applications was Mylar (material density $\tau = 1,350\,\mathrm{kg/m^3}$), a coated polyester film used to construct, for example, the Echo balloon series in the 1960s. For recent space applications, the more advanced polyimide Kapton is usually employed (material density $\tau = 1,572\,\mathrm{kg/m^3}$) [48].

A common problem associated with operating thin membranes in space is wrinkling [49]. This effect is due to many factors such as imperfections generated in the material during manufacture, non-uniform mechanical and thermal loads, non-uniform tensioning, in-plane compressive loads, and the dynamic response of the structure. Further analyses consider the billowing of solar sail films attached to, for example, deployable booms or web cables [9], an effect undesirable for sail propulsion due to the losses in thrust magnitude. However, exploiting this effect to generate specific, for example, parabolic deflection shapes of large gossamer membrane structures could be an advantage, as will be discussed in this thesis.

In order to realise a rigid support assembly for large gossamer systems such as space antennae and solar arrays, deployable structures such as foldable trusses, expandable booms and unfurlable meshes are common established space technologies [20]. However, they typically rely on a large number of mechanisms (hinges, bars, cables). These support structures and their associated deployment mechanisms, launch restraints and controls, comprise sometimes more than 90 percent of the total mass budget for a deployed assembly [50]. Therefore, inflatable support structures have been established as a promising technology to deploy and support the membrane over recent decades. A common design concept suggests a toroidal polymer hoop that is pressurised in orbit to induce self-inflation, after which the material is self-rigidised. A comprehensive review of analysis and simulation methodologies is given in Ref. [51]. A study of useful inflatables is also provided in Ref. [52].

Solar sails

Solar sailing uses large deployable reflective membranes for propulsion by exploiting solar radiation pressure (SRP) [53]. The main limitation of solar sailing, and challenge for the coming years, is the development of high area-to-mass ratio (high 'lightness number', see Section 2.1) spacecraft, in which the sail can provide a useful acceleration, while carrying a reasonable payload mass and other spacecraft subsystems. A second, but no less important issue is the attitude control of the large, thin membrane, as well as its surface degradation during the mission. While an anomaly in pointing results in the wrong thrust vector direction, the presence of wrinkles diminishes the efficiency of the sail [54]. A recent overview contains several mission concept studies and the current technology roadmap for solar sails [55].

Attitude control

Attitude control systems for gossamer spacecraft are required to compensate for various disturbances acting on the structure in orbit such as aerodynamic drag, gravity-gradient and magnetic torques [56]. Furthermore, the control system needs to counteract any excess spacecraft angular momentum, for example, during launcher separation or (non-ideal) deployment. In addition, internal torques are created by spacecraft subsystems such as mechanisms, outgassing and attitude thruster misalignments. Another source for disturbing torques is an offset between the centre-of-pressure (c.p.) and the centre-of-mass (c.m.) of the structure, caused by SRP. However, this effect can also be *exploited* for attitude control, by employing moving masses that can slide, for example, along support booms or tethers to change the position of the spacecraft c.m. with respect to the c.p. [57]. Conventional attitude systems include thrusters, reaction wheels, magnetic torquers or spin-stabilisation [58]. In addition, other concepts propose articulated tip vanes mounted on the edges of the structure [59]. A comprehensive study of attitude control systems, dynamic modelling and control analyses can be found in Refs. [60, 61].

1.1.3 Smart, multifunctional and adaptive gossamer spacecraft

The key requirement for gossamer structures to achieve ultra-low-mass suggests the introduction of concepts such as multi-functionality to its components. Novel innovative space technologies could integrate functions of previously separate subsystems into one. For example, it has been proposed to use the large membrane of a solar sail for other applications than providing propulsion during a mission [62]. Although a solar sail is less efficient further from the Sun, a multi-functional sail membrane could still be used otherwise, e.g. as a telecommunications antenna or remote sensing device. For example, after reaching its target (e.g. an asteroid or the outer solar system), the membrane could be re-configured as an antenna for data return or a science instrument, such as a radar sounder for scanning the asteroid surface or characterising the Kuiper belt [62].

Furthermore, highly integrated membrane structures could host, for example, distributed power systems and active/passive thermal control systems [13]. This could be achieved by embedding polymer MEMS actuators into the membrane material or into a composite support structure, or by printing foldable graphene circuit boards on the surface [63]. Further examples include inflatable shape changing colonies actuated using MEMS devices to enable smart adaptive space structures [64].

However, future 'smart' gossamer spacecraft could use highly distributed sensing and actuation not only to reduce the system mass. Of further importance is the requirement for membrane reflectors to reliably maintain their surface precision during the mission lifetime, in particular for remote sensing and telescope applications. This has driven the concept of adaptability in recent developments of gossamer membrane spacecraft. Such systems could adapt to changing, highly dynamic environments and load cases such as, for example, electrostatic switched radiators for thermal control [65]. Several examples of adaptive 'morphing' aircraft exist (e.g. variable-sweep wing aircraft), however, very little research has been done in this area for spacecraft [66, 67].

Integrating actuators and sensors into the surface and support structure of a membrane reflector is necessary to evaluate the surface accuracy on orbit in terms of surface distortion caused by thermal effects, imperfections in the manufacturing process, and long-term changes in the material properties (degradation) [13]. The following summary outlines various lightweight methods for active surface control of large space structures, which have been developed in the past.

Surface shape control methods

Different technology concepts for adaptive compensation of surface shape error exist to improve the aperture efficiency of membrane reflectors and thus, performance: for example, through boundary displacements [68], active temperature gradients [69] or pressurised lenticulars with transparent canopies [70]. More recent control techniques employ electroactive materials such as piezoceramic lead zirconate titanate (PZT) actuators for shape correction of thin membrane mirrors for space telescopes [71, 72].

Piezoceramic macro-fiber composites (MFC) have also been used for excitation and control of out-of-plane modes of solar sail membranes [73]. Employing electroactive polymer (EAP) films such as polyvinylidene fluoride (PVDF) for surface control of space membrane reflectors is currently being investigated [74]. Dielectric elastomers, a type of EAP employing electrostatic forces between two electrodes to squeeze a polymer film have been tested on the back of flexible mirrors [75]. A comprehensive review of membrane shape control for gossamer structures has been conducted in Ref. [21].

1.1.4 Optical control of gossamer spacecraft

Currently developed methods for attitude control of large gossamer structures, as outlined in Section 1.1.2, will potentially be complex (moving masses), fragile (articulated tip vanes), or will add considerable mass to the spacecraft (reaction wheels). In addition, recent developments in shape control methods for thin membranes indicate that the efficiency of actuators is still limited. Therefore, a different concept will be adopted in this thesis. Based on the principle of exploiting in-situ resources to achieve crucial mass savings, SRP has the potential to replace traditional systems in a radically new way. Although relatively small in magnitude, about $10\,\mu\mathrm{N/m^2}$ at the Earth's distance from the Sun, SRP has already been used successfully for passive attitude control of satellites [76] and for continuous propulsion of solar sail spacecraft [77]. Since the aperture size of future gossamer spacecraft is expected to be in the order of 100 m in diameter for membrane reflectors, and possibly in the kilometre range for tethered spacecraft, light pressure applies a reasonable force sufficient to control the structure in space.

Attitude stabilization of a satellite by SRP was first proposed in 1959 [78], and later in 1965 [79], where the latter considered differential reflectivity on the spacecraft due to local surface irregularities. Since then, the concept of employing an SRP gradient for stabilisation and control of satellites has been investigated, for example, using articulated reflective surfaces [80, 81, 82], where the latter also considered the combined effect of gravity-gradient torques. SRP has already been used successfully for passive attitude control in both Earth orbit and for inner solar system missions, where the effect of SRP increases significantly due to the inverse square variation with solar distance [2]. Both the Mariner-10 [76] and MESSENGER spacecraft [83] used SRP by design to reduce propellant requirements for attitude thrusters, while the Hayabusa spacecraft was able to use SRP to recover from a partial failure of its attitude control systems [84]. Today, so-called 'trim tabs' are commonly used to aid attitude control of large spacecraft in GEO, thereby reducing propellant requirements and extending mission lifetime. Trim tabs are typically mounted on the tips of solar arrays in order to maximize the torque delivered [85]. A review of attitude dynamics of spacecraft in the presence of environmental forces, with particular emphasis on SRP, is presented in Ref. [86].

As will be demonstrated in this thesis, manipulating the surface reflectivity of gossamer spacecraft offers the possibility of controlling the attitude without employing additional mechanical systems or thrusters. Furthermore, by adopting a highly-integrated multi-functional design approach, reflectivity modulation is also envisaged in this thesis to control the surface deflection of gossamer membranes through SRP. In principle, this can be achieved using materials with controllable surface properties that, when combined with integrated control electronics, could adapt to changing environmental conditions or mission needs. For example, so-called ‘electro-chromic devices’ have already been employed successfully for attitude control on the IKAROS solar sail demonstrator mission (JAXA) in 2010 [77]. In addition, such devices have been considered to stabilise the orbit of a solar sail with a fixed attitude about an artificial Lagrange point [87]. Such devices will be described in more detail in Section 2.4. In summary, the concept of ‘optical control’ has the potential to provide a unique competitive advantage to gossamer spacecraft over previously developed control techniques.

1.2 Thesis objectives

From the discussion of large gossamer space structures in Section 1.1 and their requirement to achieve low mass, high surface precision and robust control in Section 1.1.3, the following research objectives can be defined:

Optical attitude control

- Investigate the use of SRP to control the attitude of large gossamer spacecraft through the manipulation of their surface reflectivity
- In order to assess this type of control, develop and compare different reflectivity distribution models across the surface
- Demonstrate the potential of optical control by applying these models to attitude manoeuvres

Optical shape control

- Investigate the effect of SRP loads on the surface shape of large gossamer membrane reflectors
- Investigate the manipulation of the nominal deflection profile of the membrane by controlling the reflectivity across the surface
- Demonstrate the potential of optical shape control by realising particular deflection shapes and investigating their performance

1.3 Contributions of thesis

In this thesis, the potential of exploiting SRP for the control of large gossamer spacecraft is demonstrated, in order to improve their performance by minimising the overall system mass, system complexity and stowed volume during launch. To this aim, different mathematical tools are developed, which consider the control of gossamer structures by modulating the optical surface properties. Two different gossamer spacecraft concepts are investigated: a two-mass tethered 'dumbbell' configuration and a large gossamer membrane reflector, deployed by extendible booms (square surface) or by a circular (spin-stabilised) hoop structure. In all the analyses, closed-form mathematical approaches are employed, wherever possible, in order to seek for general analytic solutions to the problems investigated, rather than finding individual solutions to specific geometries in a finite element method (FEM) approach.

Optical attitude control

The feasibility of using optical attitude control for large gossamer spacecraft is demonstrated first by considering a simple (non-spinning) long-baseline tethered formation on a circular Sun-centred orbit.

As a first approximation, the spacecraft is modelled as two separate point masses, connected by a rigid massless link to represent the objective of achieving an ultra-low-mass spacecraft design. SRP is introduced to the system by assigning a variable surface reflectivity to the tip masses, through the use of lightness numbers. The equations of motion of the system in the combined gravitational and SRP force field are derived using a Hamiltonian approach. The system's dynamics and stability properties are analysed and optical control of the spacecraft attitude is demonstrated through changing the lightness numbers, exploiting the heteroclinic connections in the phase space of the problem. It is shown that introducing SRP creates artificial unstable equilibria that are different from those of the pure gravity gradient dumbbell. In particular, by controlling the lightness numbers of the tip masses, equilibrium attitudes at an arbitrary angle, relative to the local vertical, can be created.

The additional SRP forces perturb the circular Keplerian motion of the system around the central body. Accordingly, coupling of the orbit and attitude dynamics is reintroduced by deriving constraints for the lightness numbers, showing that the dumbbell can be maintained on a circular non-Keplerian orbit for arbitrary attitudes using light pressure. This analysis supports the concept of using modulated SRP for attitude station-keeping of tethered gossamer systems at relatively low cost, since the lightness numbers, or surface reflectivities, respectively, can in principle be changed using electro-chromic coatings. Therefore, no mechanical systems or thrusters are required to maintain, for example, a fixed observation attitude.

Following these results, the concept of modulating the surface reflectivity for efficient low-mass attitude control is further demonstrated for large gossamer membrane reflectors. The literature has considered electro-chromic devices across the surface of a solar sail for orbit stabilisation. However, using this concept for attitude control of the membrane has not been investigated before. In this thesis, the nominal SRP forces acting on a flat rigid reflector surface are controlled by introducing different surface reflectivity models across the membrane. This generates variable optical torques about the in-plane spacecraft axes. For the first time, this analysis is used to investigate two-axis optical steering of large gossamer spacecraft.

Each reflectivity distribution model is applied to perform basic attitude manoeuvres, for example, under the effect of gravity-gradient torques in LEO. To this aim, a quaternion-based control framework is developed, which controls the reflectivity distribution across the membrane surface, hence generating variable optical torques sufficient to steer the spacecraft. It is shown that through these torques, the reflector can be brought, for example, to a Sun-pointing attitude from an arbitrary initial displacement. The control framework also considers the variation of SRP force magnitude with changing light incidence angle towards the Sun during the manoeuvre, hereby presenting solutions to a challenging attitude control problem.

Optical shape control

Again, for the first time, reflectivity modulation is also applied to control the shape of large membrane surfaces, thereby replacing mechanical or piezoelectric systems. Previously, the feasibility of exploiting SRP has only been validated for spacecraft attitude stabilisation and control, as highlighted in Section 1.1.4. Limited electro-chromic coatings have been applied during the IKAROS mission to demonstrate the concept for attitude control of solar sails. In this thesis, a novel approach is developed that uses modulated SRP to enable optical shape control of large gossamer membranes. Therefore, this thesis supports the ongoing engineering effort to realise ultra-lightweight low-cost spacecraft configurations for a variety of future space applications.

In particular, the nominal deflection profiles due to uniform SRP are calculated for different elastic, tensioned membranes, in terms of surface diameter and solar distance, using equations of non-linear thin membrane theory. Subsequently, the nominal (non-parabolic) deflection shapes obtained are optimised by applying suitable reflectivity distributions across the surface, hence generating a true parabolic profile. The required reflectivity function is derived semi-analytically using an inverse problem approach. Since the reflectivity function found does not depend on membrane size, thickness or solar distance, these results indicate that a parabolic profile can be generated with relatively low optical actuation effort.

In order to improve the quite large focal lengths of the deflected shapes that can be generated for a tensioned membrane, possible ways to increase the deflection magnitude are investigated. Accordingly, a slack untensioned surface is further investigated, through deploying an excess of film material from the supporting structure. The literature has considered the billowing of large solar sail films attached to, for example, deployable booms. As summarised in Section 1.1.2, corresponding research focussed on capturing the effect of non-ideal flatness on the SRP thrust produced by a solar sail for in-space propulsion. However, in all cases, slack reflective films have not been used intentionally to create specific (parabolic) surface deflections, as is the case here.

In summary, this thesis demonstrates the potential of controlling the spacecraft's attitude and morphology without using complex mechanical systems or thrusters. Under the assumption that further development will allow future distribution of ultra-thin (micron-level) electro-chromic coatings across large membranes, these findings represent a major step towards highly-integrated adaptive membrane reflectors and support the development of this promising key-technology to deliver advanced space technology applications.

1.4 Published work

1.4.1 Peer-rewieved journal publications

- Borggräfe, A., Heiligers, J., Ceriotti, M., and McInnes, C.R., *Shape Control of Slack Space Reflectors using Modulated Solar Pressure*, Proceedings of the Royal Society, Part A, 471: 20150119, **2015**, DOI: 10.1098/rspa.2015.0119.

- Borggräfe, A., Heiligers, J., McInnes, C. R., and Ceriotti, M., *Attitude Dynamics of the Classical Dumbbell Problem with Solar Radiation Pressure*, Journal of Guidance, Control, and Dynamics, 38(1), 168-173, **2015**, DOI: 10.2514/1.g000392.

- Borggräfe, A., Heiligers, J., Ceriotti, M., and McInnes, C. R. *Inverse problem for shape control of flexible space reflectors using distributed solar pressure*, Smart Materials and Structures, Vol. 23, No. 7, p. 075026, **2014**, DOI: 10.1088/0964-1726/23/7/075026.

1.4.2 Conference papers

- Borggräfe, A., Heiligers, J., Ceriotti, M., McInnes, C.R., *Attitude Control of Large Gossamer Spacecraft using Surface Reflectivity Modulation*, 65th International Astronautical Congress (IAC), Toronto, Canada, 29 Sept - 3 Oct, **2014** (IAC-14,C1,3.4x25229).

- Borggräfe, A., Heiligers, J., Ceriotti, M., and McInnes, C.R., *Optical Control of Solar Sails using Distributed Reflectivity*, in Spacecraft Structures Conference, 13 - 17 Jan, **2014**, American Institute of Aeronautics and Astronautics, DOI: 10.2514/6.2014-0833.

- Borggräfe, A., Heiligers, J., Ceriotti, M., and McInnes, C.R., *Distributed Reflectivity Solar Sails for Extended Mission Applications*, in Advances in Solar Sailing, **2014**, Springer Berlin Heidelberg, p. 331-350, DOI: 10.1007/978-3-642-34907-2_22.

- Borggräfe, A., Heiligers, J., Ceriotti, M., McInnes, C.R., *Shape-Changing Solar Sails for Novel Mission Applications*, 64th International Astronautical Congress (IAC), Beijing, China, 23 - 27 Sept, **2013** (IAC-13,C2.5,4x19175).

- Borggräfe, A., Ceriotti, M., Heiligers, J., McInnes, C.R., *Coupled Orbit and Attitude Dynamics of a Reconfigurable Spacecraft with Solar Radiation Pressure*, 63rd

International Astronautical Congress (IAC), Naples, Italy, 1 - 5 October **2012** (IAC-12,C1,9,10,x14125).

1.5 Thesis structure

In order to pursue the research objectives defined in Section 1.2, Chapter 2 will provide the necessary background information on SRP, including an overview of different SRP force models, the concept of surface reflectivity control and a brief description of electrochromic devices. The remainder of this thesis can be divided into two main parts: the first part covers Chapter 3 and Chapter 4, focussing on optical attitude control of gossamer spacecraft. In particular, a two-mass tethered 'dumbbell' spacecraft and a large membrane reflector will be considered. In the second part, Chapter 5 and Chapter 6, modulated SRP will be employed to control the shape of large gossamer membrane structures.

In **Chapter 3** the concept of optical attitude control will be considered for a long-baseline tethered spacecraft. In particular, the analysis will extend the attitude dynamics of the classical planar dumbbell problem by introducing SRP. The system will be modelled as a rigid body subject to central gravity and SRP acting on the tip masses. To this aim, lightness numbers will be assigned to the tip masses to demonstrate the effect of a SRP gradient on the equilibria of the system and its stability properties. An analytical Hamiltonian approach will be employed to describe the planar motion of the system in Sun-centred orbits. The stability of the decoupled problem on a circular Keplerian orbit will be investigated and control is considered by modulating the lightness numbers. The character of new unstable equilibria, due to the SRP gradient, and heteroclinic connections in the phase space of the problem will be investigated. Finally, since SRP is perturbing the Keplerian motion of the system, the attitude/orbit coupling is reintroduced by deriving constraints for the lightness numbers to maintain the system on a circular non-Keplerian orbit.

In the following, **Chapter 4**, the attitude dynamics and the control of a large gossamer membrane reflector with a variable surface reflectivity distribution will be investigated. When modulating the reflectivity across the surface, the SRP forces and torques across the membrane can be controlled. Three different reflectivity models, of increasing complexity, will be presented. First, a continuous reflectivity function will be considered to maintain a fixed Sun-pointing attitude under the effect of, for example, gravity gradient torques in Earth orbit. The second approach will assume constrained high/low reflectivity regions across the surface. Finally, a discrete reflectivity array of electro-chromic cells will be employed to generate a wide range of torques in the reflector plane. A quaternion-based attitude control framework will be developed to address each individual cell, which will enable two-axis attitude control of the spacecraft in a Sun-centred orbit. This will demonstrate the potential of manipulating the SRP to realise flexible attitude control of large gossamer spacecraft, while minimising the actuation effort.

In **Chapter 5**, a non-uniform surface reflectivity will be considered for controlled elastic deflection of a large circular membrane reflector. First, the nominal deflection profile due to uniform vertical SRP will be investigated using the equations of non-linear thin membrane theory. When changing the surface reflectivity across the membrane, the nominal SRP loads can be manipulated optically, thus controlling the surface shape without using mechanical or piezo-electric actuators. An analytic solution will be presented to the inverse problem of finding the necessary reflectivity distribution in order to create a specific, for example, parabolic membrane deflection. The required reflectivity distribution as a function of membrane size, thickness and solar distance will be investigated. The resulting parabolic shapes will be evaluated in terms of the achievable focal lengths as a function of aperture size and solar distance.

As a next step, the deflection profile of a large slack membrane surface, suspended from its supporting hoop structure, will be considered in **Chapter 6**. This investigation will be required to reduce the focal lengths found for a tensioned elastic membrane in Chapter 5. To this aim, the circular film will be modelled using 'catenary-type' radial strings, suspended in between the rigid hoop. This approach is adopted from natural spider webs and assumes that a slack ideal surface can be approximated by a collection of inextensible, infinitely flexible strings. This approximation enables a semi-analytic investigation of slack suspended surfaces involving very large deflections. The governing equations of the string, subject to various distributed loads, will be presented. In addition, the effect of centrifugal forces on a spin-stabilised reflector disk will be considered. The nominal deflection profiles will be manipulated using suitable reflectivity functions across the string. Finally, an inverse method, similar to that developed in Chapter 5 will be employed to find the reflectivity distribution that generates a parabolic deflection profile. As will be demonstrated, short focal lengths of the reflector can be obtained when large slack lengths of the membrane are employed.

Each chapter finishes with a summary and highlights the conclusions, which come together in the overall conclusions at the end of this thesis as well as a discussion on future work.

Chapter 2

Physical Background

In this chapter, the mathematical models employed throughout this thesis will be presented and discussed. The overarching principle exploited in this thesis is solar radiation pressure, which will be briefly discussed in Section 2.1, followed by an overview of the different SRP models considered in this thesis in Section 2.2. Finally, the concept of the lightness number will be introduced in Section 2.3, while the chapter finishes with a discussion of the concept of surface reflectivity control using electro-chromic devices.

2.1 Solar Radiation Pressure

The Sun constantly emits a vast amount of electro-magnetic radiation, or photons, into space. When the photons interact with, for example, a surface or the atmosphere of a planet, the photonic momentum is transferred and applies a pressure. Originating from the combination of Max Planck's quantum mechanics with Alberst Einstein's special relativity [2], the solar radiation pressure is defined as

$$p = \frac{W_{\mathrm{S}}}{c} \tag{2.1}$$

with W_{S} the solar energy flux (energy crossing unit area in unit time) and c the speed of light in vacuum. When further introducing the radial distance from the Sun R_{S}, scaled with the Earth's mean distance $R_{\mathrm{S},0} = 149,597,871$ km $= 1$ AU (Astronomical Unit), the standard inverse square law for the SRP yields

$$p = \frac{W_{\mathrm{S},0}}{c}\left(\frac{R_{\mathrm{S},0}}{R_{\mathrm{S}}}\right)^2 \tag{2.2}$$

where $W_{\mathrm{S},0} = 1368\,\mathrm{W/m^2}$ denotes the mean value of the solar energy flux at 1 AU, commonly termed the 'solar constant'. Since the Earth's orbit is slightly elliptic, the energy flux varies by approx. 3.5 % during the year, but at the Earth's mean distance from the Sun, the SRP can be computed to be

$$p_0 = \frac{W_{\mathrm{S},0}}{c} = 4.563\,\frac{\mu\mathrm{N}}{\mathrm{m}^2} \tag{2.3}$$

The range of physical effects associated with SRP, and with the space environment in general, are quite complex. Therefore, the following assumptions are adopted throughout this thesis [2]:

- The optical surface properties of an object do not change over time. Therefore, the degradation of the material caused by space environmental effects is not considered (see Section 2.2.5)
- Other forms of momentum transport such as solar wind or atmospheric drag are neglected
- Other forms of radiation such as planetary albedo, thermal or cosmic microwave background radiation are neglected
- At the solar distances considered in this thesis, the Sun's rays are assumed to be parallel. This assumption is adequate as the effect of the Sun being a disc of finite angular size (causing non-parallel rays), is only relevant in close proximity to the Sun ($R_\mathrm{S} \leq 0.05$ AU)
- The effects of the limb-darkened solar disc and the decreased intensity in the Sun's outer regions are neglected

Further assumptions will be defined with respect to the optical surface properties, which will be introduced in the next section.

2.2 SRP models

In order to describe, as well as to simplify, the rather complex interaction between the solar photons and a surface in space, several SRP models are reported in the literature [2]. Primarily, such models are derived from an analytical point of view, while some are also complemented by empirical data resulting from experiments. All models commonly express the resulting SRP acting on a surface as a function of, for example, the light

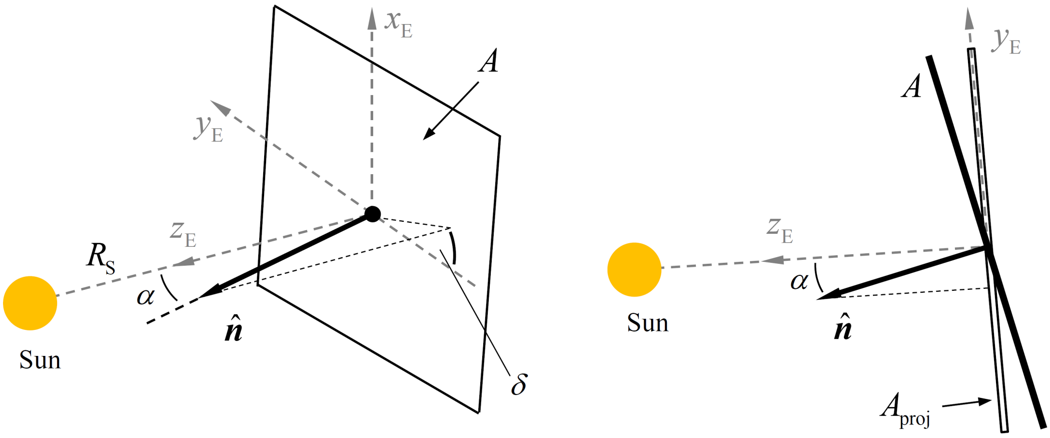

Figure 2.1: Surface attitude with respect to the Sun in an orbit-fixed reference frame $\mathcal{E} := (\mathbf{x}_E, \mathbf{y}_E, \mathbf{z}_E)$

incidence angle. For this reason, the attitude of a surface in space has to be defined first.

As shown in Fig. 2.1, the attitude of a surface of area A can be described by the surface normal vector $\hat{\mathbf{n}}$, the unit vector perpendicular to the surface in the direction of the Sun. This vector can be described with respect to, for example, a right-handed orbit reference frame $\mathcal{E} := (\mathbf{x}_E, \mathbf{y}_E, \mathbf{z}_E)$, centred at the c.m. of the surface, with the z_E-axis oriented towards the Sun. This coordinate system will be described in more detail in Section 4.2.1. The direction of $\hat{\mathbf{n}}$ with respect to frame $\mathcal{E}$ can be described by the surface cone angle α and the surface clock angle δ, which are both defined in Fig. 2.1. As the figure shows, α is the angle between the $\mathbf{z}_E$-axis and the surface normal direction $\hat{\mathbf{n}}$. The clock angle δ is the angle between the negative $\mathbf{y}_E$-axis and the projection of $\hat{\mathbf{n}}$ in the $(\mathbf{x}_E, \mathbf{y}_E)$-plane. Note that solar radiation pressure is only effected by the cone angle as a change in clock angle does not affect the projected sail area $A_{\mathrm{proj}} = A \cdot \cos\alpha$, which is encountered by the solar photons.

2.2.1 Ideal SRP Model

The so-called ideal SRP model assumes that the surface is a perfectly (specular) reflecting mirror and neglects all other forms of optical interactions between the solar photons and the surface such as diffuse reflection (scattering), absorption, and thermal re-emission. The model also does not account for wrinkles or a non-zero surface roughness. Furthermore, Eq. (2.2) only accounts for the SRP induced by the incoming photons, while a perfectly reflecting mirror doubles the pressure due to the additional momentum created by the reflected photons. The light pressure exerted on a perfectly reflecting surface at 1 AU and perpendicular to the Sun then becomes

$$p = 2p_0 = 9.126\,\frac{\mu\mathrm{N}}{\mathrm{m}^2} \tag{2.4}$$

In addition, accounting for other solar distances and the surface cone angle, the SRP can be written as [2]

$$p_{\mathrm{SRP}} = 2p_0\left(\frac{R_{\mathrm{S},0}}{R_{\mathrm{S}}}\right)^2 \cos^2\alpha \tag{2.5}$$

Finally, the total SRP force vector $\mathbf{F}_{\mathrm{SRP}}$ acting on a surface area A equals

$$\mathbf{F}_{\mathrm{SRP}} = -p_{\mathrm{SRP}} A\,\hat{\mathbf{n}} \tag{2.6}$$

Note that, due to the assumptions made in the ideal SRP model, the direction of the resulting SRP force is always along the surface norm, $-\hat{\mathbf{n}}$. In addition, no material properties have been accounted for in this model. However, more complex SRP models exist, which will be introduced in the following.

2.2.2 Simplified SRP model

The so-called 'simplified SRP model' considers a non-perfectly reflecting surface, by introducing the surface reflectivity coefficient ρ in the interval $\rho = [0, 1]$. Here, the maximum reflectivity $\rho = 1$ represents a perfectly reflecting mirror that experiences the maximum possible SRP $p_{\mathrm{SRP,max}} = 2p_0$, as seen in Eq. (2.5), when further assuming a surface cone angle $\alpha = 0$ at 1 AU solar distance. Contrary to this, the minimum reflectivity, $\rho = 0$, represents an ideal absorber. This reduces the SRP to $p_{\mathrm{SRP,min}} = p_0$, under the assumption that (ideally) no photons are reflected and only the momentum of the incoming photons exerts a pressure onto the surface.

Considering these assumptions, the SRP exerted on a surface of reflectivity ρ now becomes

$$p_{\mathrm{SRP}} = p_0(1+\rho)\left(\frac{R_{\mathrm{S},0}}{R_{\mathrm{S}}}\right)^2 \cos^2\alpha \tag{2.7}$$

Throughout this thesis, the simplified SRP model will be used to describe the effect of electro-chromic coatings on the optical surface properties, which will be discussed in Section 2.4.

2.2.3 Standard SRP Model

To complete the overview of commonly used SRP models, although not used in this thesis, the 'standard SRP model' accounts for additional optical properties of a non-ideal surface: diffuse reflection, absorption and emission [2]. In particular, the optical surface is characterised by three thermo-optical parameters: the reflectivity ρ, the absorptivity $\tilde{\alpha} = 1 - \rho$ and the transmittance $\tilde{\tau}$, fulfilling the constraint

$$\rho + \tilde{\alpha} + \tilde{\tau} = 1 \tag{2.8}$$

where the tilde notations $\tilde{\alpha}$ and $\tilde{\tau}$ are used to avoid confusion with the symbols for the cone angle α and the material density τ, which will be used later in Chapter 5. Usually, the transmittance is zero (opaque surface), such that the previous equation reduces to

$$\tilde{\alpha} = 1 - \rho. \tag{2.9}$$

Since a real surface is not an ideal mirror, not all photons are reflected specularly. Therefore, the reflectivity coefficient ρ is further divided into the fraction of photons undergoing specular reflection ρ_{s}, diffuse reflection ρ_{d} and back reflection ρ_{b} (in direction of the incident photons) with

$$\rho_{\mathrm{s}} + \rho_{\mathrm{d}} + \rho_{\mathrm{b}} = 1. \tag{2.10}$$

Conclusively, all the aforementioned effects are summarised in Fig. 2.2. Each type of photonic interaction results in a different fraction of the total SRP force $\mathbf{F}_{\mathrm{SRP}}$, as discussed in detail in Ref. [2]. For example, as a result of the non-ideal reflection of the surface, the total SRP force vector does not act perpendicular to the surface, because the force due to reflected photons is smaller than the force due to the incoming photons.

2.2.4 Refined SRP model

Despite considering the optical properties of the surface, the standard SRP model can not necessarily be regarded as 'realistic', since all optical coefficients are assumed to be constants. In reality, these coefficients depend on, for example, the surface cone angle or the surface roughness of the material employed. To this aim, the so-called 'refined SRP model' has been developed, which introduces variable optical coefficients to the standard SRP model [89]. The central refinement of the model is the variation of the reflectivity ρ and the specular reflectivity ρ_{s} with the light incidence angle α.

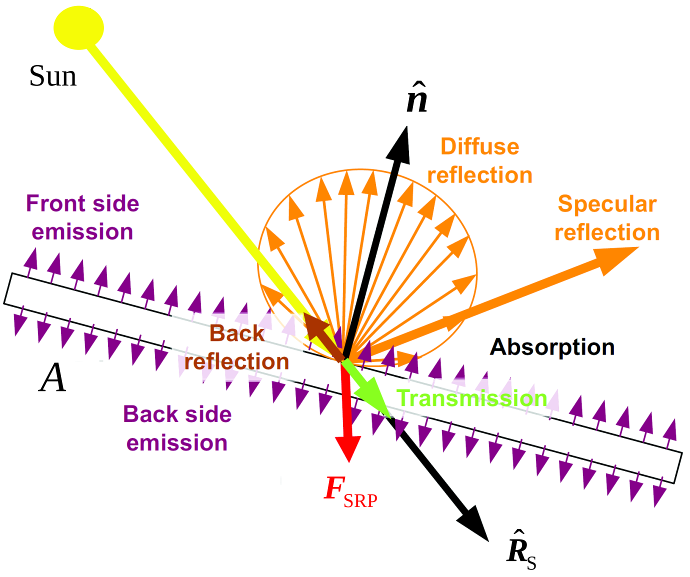

Figure 2.2: Interactions of solar photons (from direction of the Sun S) with an optical surface [88]

In addition, the model also considers the surface roughness, representing a mechanical property of the surface. In addition, the emissivity ϵ depends on the current surface equilibrium temperature and thus on the surface attitude with respect to the Sun, as well as on the solar distance.

2.2.5 SRP surface degradation model

Finally, all previous models assume that the optical and mechanical properties of the surface material are constant over time. Long term, however, the surface is affected by the severe space environment. To account for this, a parametric SRP model has been developed that describes the surface degradation over time. In particular, the optical coefficients are assumed to depend on the radiation dose that the material absorbs during a mission. This parametric model is termed 'optical solar sail degradation' model (OSSD) [90].

2.3 Lightness number

The lightness number β of an object describes the ratio of the SRP force or acceleration to the solar gravitation force/acceleration:

$$\beta = \frac{a_{\mathrm{c}}}{a_0} \tag{2.11}$$

Objects with a high surface reflectivity and a high area-to-mass ratio have a large lightness number. In Eq. (2.11), a_0 is the Sun's gravitational acceleration at the Earth's distance from the Sun

$$a_0 = \frac{\mu}{R_{\mathrm{S},0}^2} = 5.930 \ \frac{\mathrm{mm}}{\mathrm{s}^2} \tag{2.12}$$

where $\mu = 1.3272 \times 10^{11}\ \mathrm{km}^3/\mathrm{s}^2$ denotes the Sun's gravitational parameter. Furthermore, a_c in Eq. (2.11) is the so-called characteristic acceleration, which is defined as the SRP acceleration experienced by an object of mass m and surface area A, oriented perpendicular to the Sun at 1 AU. Therefore, according to Eq. (2.5), the characteristic acceleration is defined as

$$a_c = \frac{F_{\mathrm{SRP},0}}{m} = \frac{p_{\mathrm{SRP},0} A}{m} = \frac{2 p_0 A}{m} \tag{2.13}$$

2.4 Electro-chromic devices

As shown in Section 2.2.2, the SRP force acting on a surface essentially depends on the reflectivity coefficient of the material. According to Eq. (2.7), increasing the reflectivity increases the total force, since fewer photons are absorbed or diffusely scattered by the material. From a technical point of view, the surface reflectivity can in principle be modified using thin-film electro-chromic coatings, which consist of an electro-active material that changes its surface reflectivity according to an applied electric potential [91, 92]. Such coatings are commonly termed 'reflectivity control devices' (RCDs). As noted in Section 1.3, limited RCD cells have already been employed for attitude control on the IKAROS solar sail in 2010 [77].

In view of applying RCD coatings to the surface of large gossamer membranes, the mass per unit area of existing RCD coatings (thickness $d = 70\,\mu\mathrm{m}$) is expected to be higher than that of the reflector film itself. Therefore, future technology developments are assumed whereby the mass per unit area of the membrane with integrated optical control is similar to conventional films (see Section 1.1.2). For example, polymer-based electro-chromic coatings of total thickness below a micrometre, using single-walled carbon nanotubes, have recently been assembled for ultra-thin touch-screen panels [93]. Therefore, the mass budget for a gossamer structure using optical control compared to one using conventional thrusters and reaction wheels is not explicitly considered. The focus of the thesis is on novel actuation and control methods.

The concept of reflectivity modulation using RCD cells is shown in Fig. 2.3. The cell is actuated by electrodes to maintain either a low reflectivity state ('off', left-hand

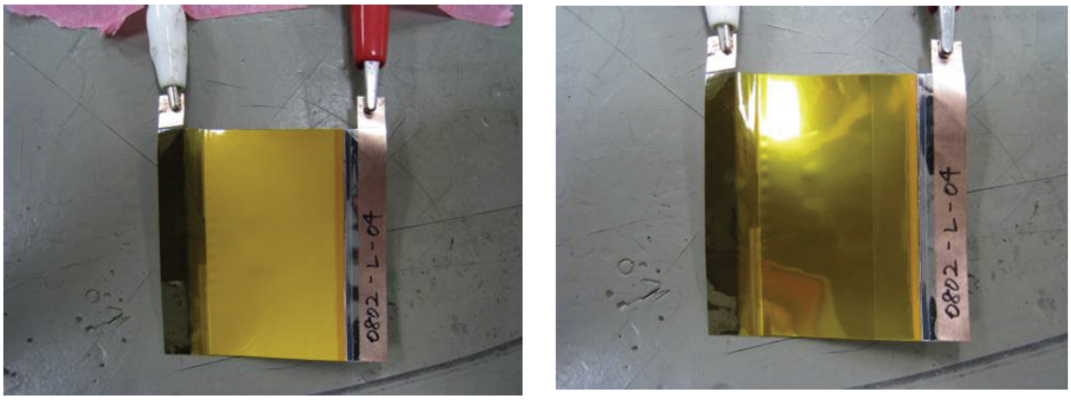

Figure 2.3: Reflectivity control device (RCD) actuated using an electric potential and two reflectivity states: 'off' (low reflectivity, left) and 'on' (high reflectivity, right) [94]

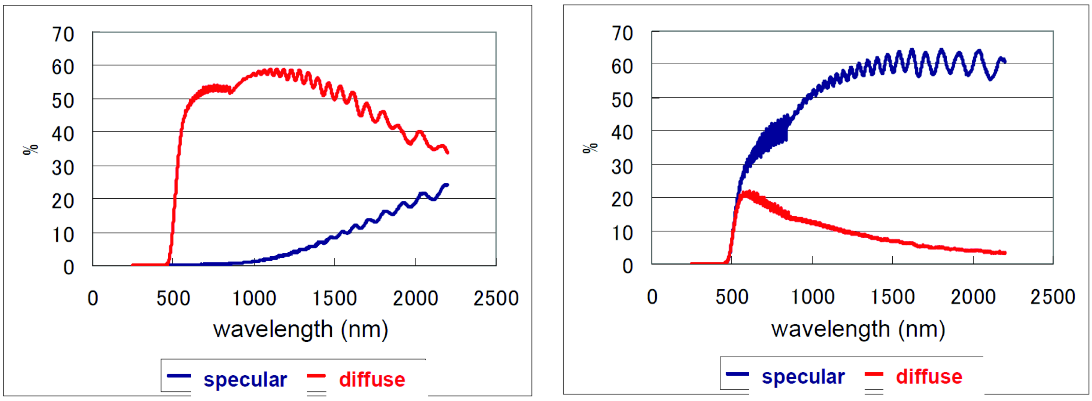

Figure 2.4: Achievable specular and diffuse surface reflectivity of RCD cells operated in two states: 'off' (low reflectivity, left) and 'on' (high reflectivity, right) [94]

side) or a high reflectivity state ('on', right-hand side). Throughout this thesis, it is assumed that RCD coatings are able to modulate the surface reflectivity in the interval $\rho = [0, 1]$. However, as shown in Fig. 2.4, currently developed RCDs can achieve a maximum reflectivity $\rho_{\max} = 0.6$, depending on the wavelength of the incoming light.

Chapter 3

Two-body tethered spacecraft dynamics with SRP

In order to investigate the potential of using modulated SRP to control gossamer spacecraft, this chapter will provide an initial demonstration of the concept by considering a tethered spacecraft configuration. As a first approximation, a gossamer spacecraft will be modelled as a collection of distributed point masses, connected by massless links to represent an ultra-low-mass gossamer spacecraft. In the simplest case, two masses are linked by a rigid massless rod, rather than a flexible tether. Ideally, such a 'dumbbell' system represents a simple long-baseline formation for many future space applications, as detailed in Section 1.1.2. The concept and the problem definition will be introduced in Section 3.1. After deriving the equations of motion of the system using a Hamiltonian approach in Section 3.2, the system's dynamics and stability properties will be analysed in Section 3.3. In Section 3.4, the attitude dynamics and control of the system through SRP will be demonstrated in the phase space of the problem. Finally, Section 3.5 will summarise the chapter.

3.1 Classical dumbbell problem with SRP

This chapter extends the attitude dynamics and stability properties of the classical planar dumbbell problem, i.e. two masses connected by a rigid massless tether (see Section 1.1.2), by considering the effect of a solar pressure gradient between the tip masses. To this aim, the widely used model of a tethered satellite system is adapted by introducing SRP forces to each mass. These SRP forces act in the radial direction from the Sun and are created by assigning a variable surface reflectivity to the tip masses through the use of lightness numbers, according to Section 2.3. Modulating the surface reflectivity can be achieved, for example, using electro-chromic coatings, as discussed in Section 2.4.

When a long tether is orbiting a central body, the relative attitude of the system affects the total force acting on the dumbbell's c.m.This means that the equations of motion (EOM) describing the orbit and attitude of the system are coupled [95]. This chapter will therefore start by defining the system's Hamiltonian and the EOM for the coupled orbit/attitude motion. By subsequently introducing a large central mass, the satellite motion is constrained to a circular orbit such that the EOM become decoupled. This allows for a stability analysis of the system's equilibrium attitudes, thereby investigating the connection between the relative equilibria and light pressure. The dynamical behaviour of the system is investigated through iso-energy curves of the Hamiltonian in phase space. Finally, motion between, and controllability around, equilibria is demonstrated through the use of heteroclinic connections and by changing the lightness numbers of the tip masses.

3.2 Equations of motion of the system

The planar motion of the dumbbell system is described with respect to a Sun-centred inertial frame $\mathcal{I}:(\mathbf{X},\mathbf{Y})$ in the case of the coupled orbit/attitude problem and relative to a rotating orbit frame $\mathcal{O}:(\mathbf{r},\boldsymbol{\nu})$, with the origin at the c.m. of the system, for the decoupled attitude dynamics (Fig. 3.1). The axes of frame $\mathcal{O}$ are aligned with the local vertical and the local horizontal relative to the Sun.

The system is modelled as a rigid body with a central mass M_B located at the c.m. and two tip masses m_1 and m_2 at each end of a massless tether. The tether length ratio $\lambda = l/R$ describes the ratio of total tether length l to orbit radius R. The three masses are approximated as point masses, with the mass ratio $\kappa = m_1/(m_1 + m_2)$ and the total mass $M = m_1 + m_2 + M_\mathrm{B}$. The Sun's gravitational force is augmented by introducing SRP forces to the tip masses, assigning arbitrary lightness numbers in the interval $\beta_i = [0, 1]$ (with $i = 1, 2$) to each of the masses, according to Section 2.3. Compared to the tip masses, the area-to-mass ratio of the central mass is assumed to be small, and therefore the lightness number of M_B can be neglected.

For a rigid body, the position vector $\mathbf{R}$ of the c.m. is defined as

$$\mathbf{R} = \frac{1}{M}\sum_{i=1}^{2} m_i \mathbf{R}_i \tag{3.1}$$

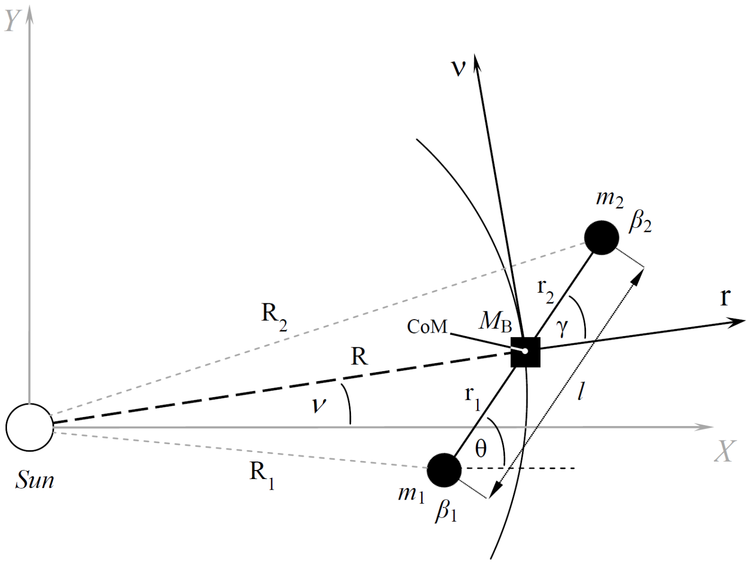

Figure 3.1: Geometry of dumbbell system in Sun-centred orbit with lightness numbers β_1 and β_2, representing SRP forces acting on the tip masses.

With respect to the inertial frame $\mathcal{I}$, the position vectors of the three masses are described as $\mathbf{R} = R(\cos\nu, \sin\nu)^{\mathrm{T}}$, $\mathbf{R}_1 = \mathbf{R} + \mathbf{r}_1$ and $\mathbf{R}_2 = \mathbf{R} + \mathbf{r}_2$. Here, $\mathbf{r}_1 = (\kappa - 1)\, l\, (\cos\theta, \sin\theta)^{\mathrm{T}}$ and $\mathbf{r}_2 = \kappa\, l\, (\cos\theta, \sin\theta)^{\mathrm{T}}$ are the position vectors of the tip masses with respect to the c.m., using the constraint that $l = r_1 + r_2$ is constant. In the above equations, ν denotes the true anomaly and θ the attitude angle relative to the inertial $\mathbf{X}$-axis, according to Fig. 3.1. The norms of the position vectors are

$$R_1 = R\left[1 - 2\lambda(1-\kappa)\cos(\theta-\nu) + \lambda^2(1-\kappa)^2\right]^{1/2} \tag{3.2a}$$

$$R_2 = R\left[1 + 2\lambda\kappa\cos(\theta-\nu) + \left(\lambda\kappa\right)^2\right]^{1/2} \tag{3.2b}$$

The planar EOM for the tethered satellite system including SRP can now be formulated using a Hamiltonian approach [96].

3.2.1 Coupled orbit/attitude EOM

The SRP forces can be included into the potential energy function V of the system, because they act in the radial direction and thus originate from a conservative force field

$$\mathbf{g} = -\frac{\mu M_{\mathrm{B}}}{R^2}\mathbf{R} - \sum_{i=1}^{2}\frac{\tilde{\mu}_i m_i}{R_i^2}\mathbf{R}_i = -\nabla V \tag{3.3}$$

where $\mu = 1.3272\times10^{11}$ km^3/s^2 denotes the Sun's gravitational parameter. The so-called effective gravitational parameter $\tilde{\mu}_i = \mu(1-\beta_i)$ for each mass is introduced to represent the reduced effect of the gravitational force due to a radially outward SRP force [2]. The effective potential energy of the system can now be written as

$$V = -\frac{\mu M_\mathrm{B}}{R} - \sum_{i=1}^{2} \frac{\tilde{\mu}_i m_i}{R_i} = -\frac{\mu M_\mathrm{B}}{R} - \frac{\mu m_1(1-\beta_1)}{R_1} - \frac{\mu m_2(1-\beta_2)}{R_2} \tag{3.4}$$

The kinetic energy of the system is split into a translational part K_transl attached to the c.m. and a rotational part K_rot, representing the contribution of the two rotating masses to the total kinetic energy such that

$$K_\mathrm{transl} = \frac{1}{2} M \dot{\mathbf{R}}\cdot\dot{\mathbf{R}} = \frac{1}{2}(m_1+m_2+M_\mathrm{B})(\dot{R}^2 + R^2\dot{\nu}^2) \tag{3.5a}$$

$$K_\mathrm{rot} = \frac{1}{2}\sum_{i=1}^{2} m_i \dot{\mathbf{r}}_i \dot{\mathbf{r}}_i = \frac{1}{2}\frac{m_1 m_2 l^2}{m_1 + m_2}\dot{\theta}^2 \tag{3.5b}$$

Using the Lagrangian $L = K - V$ and introducing three generalised coordinates $q_j = (R, \nu, \theta)$, which describe the degrees of freedom of the system, the coupled Hamiltonian function of the dynamical system can be written as [97]

$$H = \sum_{j=1}^{3} \frac{\partial L}{\partial \dot{q}_j}\dot{q}_j - L = \dot{R}\frac{\partial L}{\partial \dot{R}} + \dot{\nu}\frac{\partial L}{\partial \dot{\nu}} + \dot{\theta}\frac{\partial L}{\partial \dot{\theta}} - L \tag{3.6}$$

After calculating the generalised momenta p_j

$$p_1 = \frac{\partial L}{\partial \dot{R}} = (m_1+m_2+M_\mathrm{B})\dot{R} \tag{3.7a}$$

$$p_2 = \frac{\partial L}{\partial \dot{\nu}} = (m_1+m_2+M_\mathrm{B})R^2\dot{\nu} \tag{3.7b}$$

$$p_3 = \frac{\partial L}{\partial \dot{\theta}} = \frac{m_1 m_2 l^2}{m_1+m_2}\dot{\theta} \tag{3.7c}$$

the coupled Hamiltonian function of the system is found as

$$H = \frac{1}{2}M(\dot{R}^2 + R^2\dot{\nu}^2) + \frac{1}{2}\frac{m_1 m_2 l^2}{m_1+m_2}\dot{\theta}^2 - \frac{\mu M_\mathrm{B}}{R} - \frac{\mu m_1(1-\beta_1)}{R_1} - \frac{\mu m_2(1-\beta_2)}{R_2} \tag{3.8}$$

It is well-known that for generalised coordinates $q_j(t)$, $j = 1, ..., n$, the trajectory of $\mathbf{q}(t) = (q_1(t),\ ...,\ q_n(t))$ through the configuration space satisfies the Euler-Lagrange equations [96]

$$\frac{\mathrm{d}}{\mathrm{d}t}\left(\frac{\partial L}{\partial \dot{q}_j}\right) - \frac{\partial L}{\partial q_j} = 0 \tag{3.9}$$

Using the above equation, the coupled EOM of the three-mass system including SRP can be formulated in terms of the free parameters κ, λ, β_1 and β_2 as

$$\begin{aligned}\ddot{R} - R\dot{\nu}^2 + \frac{\mu M_\mathrm{B}}{MR^2} &+ \frac{\mu R\, m_1(1-\beta_1)\Big(1 - \lambda(1-\kappa)\cos(\theta-\nu)\Big)}{MR_1^3} \\ &+ \frac{\mu R\, m_2(1-\beta_2)\Big(1 + \lambda\kappa\cos(\theta-\nu)\Big)}{MR_2^3} = 0\end{aligned} \tag{3.10a}$$

$$\ddot{\nu} + \frac{2\dot{R}\dot{\nu}}{R} + \frac{\mu\,\kappa\, m_2\lambda\sin(\theta-\nu)}{M}\left(\frac{(1-\beta_2)}{R_2^3} - \frac{(1-\beta_1)}{R_1^3}\right) = 0 \tag{3.10b}$$

$$\ddot{\theta} + \frac{\mu\sin(\theta-\nu)}{\lambda}\left(\frac{(1-\beta_1)}{R_1^3} - \frac{(1-\beta_2)}{R_2^3}\right) = 0 \tag{3.10c}$$

3.2.2 Decoupled attitude EOM

Assuming a central mass $M_\mathrm{B} \gg m_i$, the attitude motion of the system decouples from the orbit dynamics, thus Eqs. (3.10a) and (3.10b) reduce to the common two-body problem and no longer depend on θ. Introducing the above condition for M_B into Eq. (3.10) results in the decoupled EOM of the dumbbell including SRP, given by

$$\ddot{R} + \frac{\mu}{R^2} - R\dot{\nu}^2 = 0 \tag{3.11a}$$

$$\ddot{\nu} + \frac{2\dot{R}\dot{\nu}}{R} = 0 \tag{3.11b}$$

$$\ddot{\theta} + \frac{\mu\sin(\theta-\nu)}{\lambda}\left(\frac{(1-\beta_1)}{R_1^3} - \frac{(1-\beta_2)}{R_2^3}\right) = 0 \tag{3.11c}$$

When the c.m. of the system initially follows a circular orbit with $\dot{\nu} = \sqrt{\mu/R^3}$ and $\dot{R} = 0$, Eqs. (3.11a) and (3.11b) further reduce to $\ddot{R} = 0$ and $\ddot{\nu} = 0$, respectively. When considering again Fig. 3.1, γ represents the angle between the dumbbell axis and the local vertical, thus it can be seen from the geometry that $\theta - \nu = \gamma$. Since $\ddot{\nu} = 0$, it follows that $\ddot{\theta} = \ddot{\gamma}$. Inserting this identity into Eq. (3.11c) together with the norms of the position vectors, Eq. (3.2), the decoupled attitude EOM can now be written as

$$\ddot{\gamma} + \frac{\mu \sin\gamma}{\lambda}\left[\frac{1-\beta_1}{R^3\left[1-2\lambda(1-\kappa)\cos\gamma+\lambda^2(1-\kappa)^2\right]^{3/2}} - \frac{1-\beta_2}{R^3\left[1+2\lambda\kappa\cos\gamma+(\lambda\kappa)^2\right]^{3/2}}\right] = 0 \tag{3.12}$$

3.3 Relative equilibria and stability

The dumbbell is in an equilibrium state whenever $\dot{\gamma} = 0$ and the total torque on the system is zero, thus $\ddot{\gamma} = 0$. Solving the decoupled attitude EOM, Eq. (3.12), for $\ddot{\gamma} = 0$ gives the equilibrium angles as a function of the four parameters κ, λ, β_1 and β_2. The condition $\ddot{\gamma} = 0$ has two invariant solutions for $\sin(\gamma_{\text{eq}}) = 0$ and two further solutions as

$$\cos(\gamma_{\text{eq}}) = \left[\frac{(1-\beta_2)^{\frac{2}{3}}\left(1+(1-\kappa)^2\lambda^2\right) - (1-\beta_1)^{\frac{2}{3}}\left(1+(\kappa\lambda)^2\right)}{\left[(1-\beta_1)^{\frac{2}{3}}(2\kappa\lambda)+(1-\beta_2)^{\frac{2}{3}}2(1-\kappa)\lambda\right]}\right] \tag{3.13}$$

Equation (3.13) shows that the relative equilibria γ_{eq} of the system are a function of the free parameters β_1 and β_2. When both lightness numbers are zero and for a mass ratio of $\kappa = 0.5$, the stable equilibria are 0 and ±180 degrees, while the unstable equilibria are located at ±90 degrees, corresponding to the classical gravity gradient dumbbell [98].

The stable/unstable character of the new equilibria can be evaluated through a stability analysis for which the eigenvalues of the Jacobian of the linearised system are considered [99]. In general, linearisation of a non-linear 2nd order differential equation $f(\ddot{\gamma}, \dot{\gamma}, \gamma) = 0$, evaluated at a point γ_{eq} through a Taylor series expansion up to 1st order terms, can be written as

$$\left.\frac{\partial f(\ddot{\gamma},\gamma)}{\partial\ddot{\gamma}}\right|_{\gamma_{\text{eq}}}\partial\ddot{\gamma} + \left.\frac{\partial f(\ddot{\gamma},\gamma)}{\partial\dot{\gamma}}\right|_{\gamma_{\text{eq}}}\partial\dot{\gamma} + \left.\frac{\partial f(\ddot{\gamma},\gamma)}{\partial\gamma}\right|_{\gamma_{\text{eq}}}\partial\gamma = 0 \tag{3.14}$$

When further using three coefficients A, B and C, representing the partial derivatives, Eq. (3.14) yields

$$A\,\partial\ddot{\gamma} + B\,\partial\dot{\gamma} + C\,\partial\gamma = 0 \tag{3.15}$$

Since the decoupled attitude EOM is not a function of $\dot{\gamma}$, the partial derivative B is zero. Furthermore, the coefficient $A = \partial\mathrm{f}(\ddot{\gamma},\gamma)/\partial\ddot{\gamma}$ is unity. The 2nd order linearised equation is transformed into a linear differential equation system (DES) of 1^{st} order as

$$\begin{pmatrix} \partial\dot{\gamma} \\ \partial\ddot{\gamma} \end{pmatrix} = \begin{bmatrix} 0 & 1 \\ -C & 0 \end{bmatrix} \begin{pmatrix} \partial\gamma \\ \partial\dot{\gamma} \end{pmatrix} = [J] \begin{pmatrix} \partial\gamma \\ \partial\dot{\gamma} \end{pmatrix} \tag{3.16}$$

with the Jacobian $[J]$. The partial derivative C, evaluated at an equilibrium angle γ_{eq}, can be written as

$$\begin{aligned} C = \left.\frac{\partial \mathrm{f}(\gamma,\ddot{\gamma})}{\partial\gamma}\right|_{\gamma_{\text{eq}}} &= \frac{\mu\cos(\gamma_{\text{eq}})}{\lambda}\left(\frac{(1-\beta_1)}{R_1^3} - \frac{(1-\beta_2)}{R_2^3}\right) \\ &\quad - 3\mu\sin^2(\gamma_{\text{eq}})\left(\frac{(1-\beta_1)(1-\kappa)}{R_1^5} + \frac{(1-\beta_2)\kappa}{R_2^5}\right) \end{aligned} \tag{3.17}$$

thus the Jacobian is a function of $\mu, \lambda, \kappa, \beta_1, \beta_2$ and γ_{eq}. The eigenvalues ϵ_k of the Jacobian are calculated through evaluation of its characteristic equation $\epsilon_k^2 + C = 0$, thus $\epsilon_k = \pm\sqrt{-C}$. The nature of the eigenvalues determines the type of equilibrium: 1) real, opposite sign: saddle point, 2) purely imaginary, with zero real part: centre, and 3) real, same sign: stable/unstable node. Here, the eigenvalues of $[J]$ with $\beta_1, \beta_2 \in [0,1]$ for a given dumbbell configuration are either stable centres or unstable saddles.

Figure 3.2 shows the stable (grey) and unstable (black) regions of γ_{eq} as a function of β_1 and β_2 for a chosen reference dumbbell with equal masses $m_1 = m_2$ and tether length $l = 100\,\text{km}$ on a circular orbit at $R = 1\,\text{AU}$ (i.e. Earth's distance from the Sun), thus $\lambda = 6.685 \times 10^{-7}$. The lightness numbers are scaled in both figures using $\beta_i = \beta_i^*\, 2\times10^{-6}$ with $\beta_i^* = [0,1]$ to improve readability, since the differential SRP and gravity gradient forces on the dumbbell are very small at the 1 AU distance from the Sun. In the figure, the grey plane indicates the stable equilibrium at 0 degrees. The two black curved planes indicate new unstable equilibria created by introducing SRP to the classical dumbbell problem. The system can now obtain an arbitrary equilibrium state in the range ±180 degrees for a maximum difference between the lightness number on each of the two tip masses of $\Delta\beta = |\beta_2 - \beta_1| = 2\times10^{-6}$. Although achieving such a small difference in lightness number may be technically very challenging, the results illustrate the possibility of controlling a tethered satellite system using an SRP gradient.

When solving Eq. (3.13) for β_2, the possible combinations $(\beta_1, \beta_2)_{\gamma_{\text{eq}}}$ for a given equilibrium angle, hereafter referred to as 'β-sets', can be obtained as

$$\beta_2(\beta_1, \gamma_{\text{eq}}) = 1 - \left[\frac{[1 + (\kappa\lambda)^2](1-\beta_1)^{\frac{2}{3}} - 2\kappa\lambda\cos\gamma\,(1-\beta_1)^{\frac{2}{3}}}{1 - 2(1-\kappa)\lambda\cos\gamma + ((1-\kappa)\lambda)^2}\right]^{\frac{3}{2}} \tag{3.18}$$

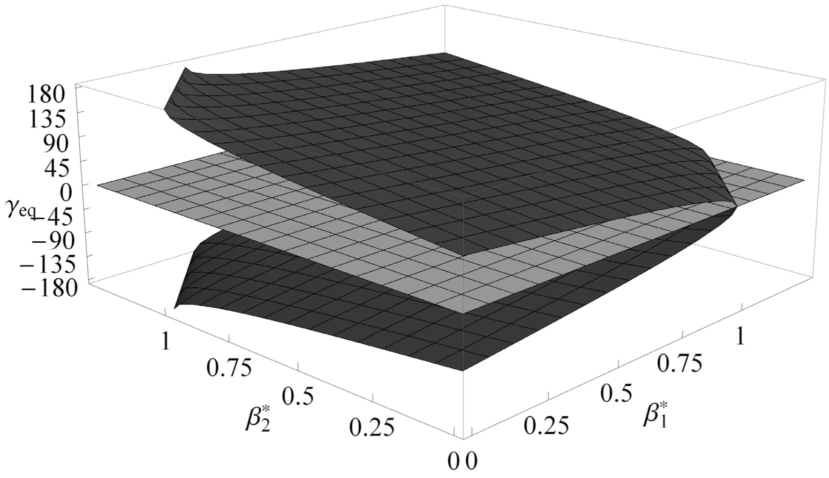

(a) Centred view

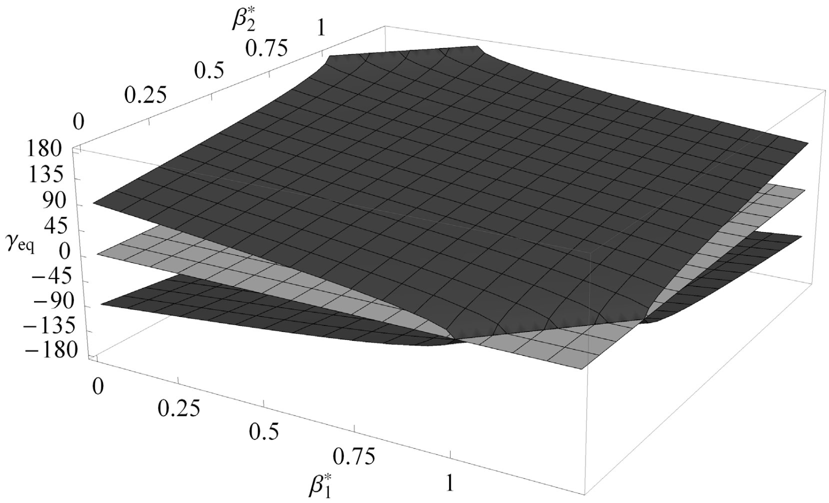

(b) Rotated view

Figure 3.2: Stable (grey) and unstable (black) equilibria γ_{eq} as function of lightness numbers β_1^* and β_2^* for dumbbell with equal masses.

Please note that the previous equation is also valid for unequal masses. For the chosen reference dumbbell and for equilibrium angles in the interval $[0, 180]$ degrees, the possible $(\beta_1, \beta_2)_{\gamma_{\mathrm{eq}}}$ sets are shown in Fig. 3.3, parameterised in steps of $\Delta\gamma = 10$ degrees. Each point on one of the curves can be chosen to create the respective unstable equilibrium attitude γ_{eq}.

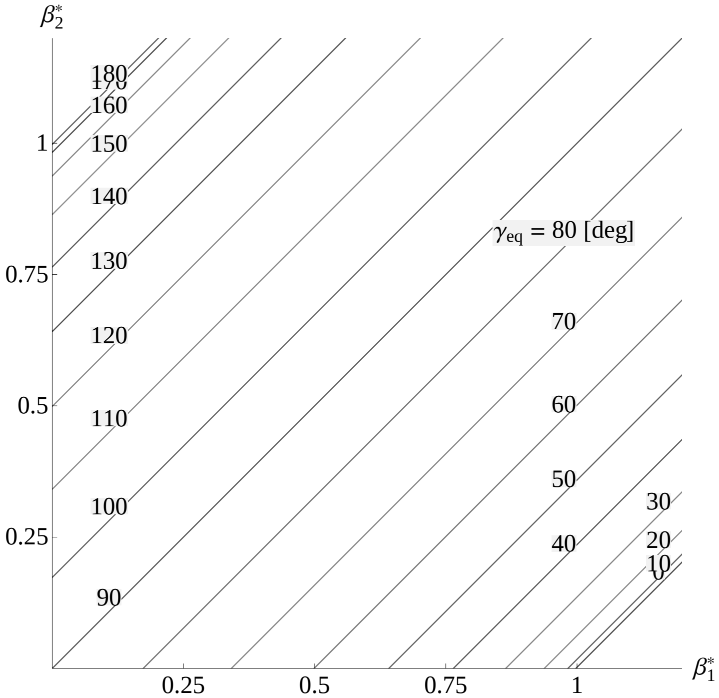

Figure 3.3: Possible lightness number sets $(\beta_1^*, \beta_2^*)_{\gamma_{eq}}$ to create unstable equilibria γ_{eq} for dumbbell with equal masses.

As a side note, without SRP, the equilibrium equation, Eq. (3.13), reduces to

$$\cos\left(\gamma_{eq,GG}\right) = \left[\frac{\lambda}{2} - \kappa\lambda\right] \tag{3.19}$$

describing the unstable equilibria $\gamma_{eq,GG}$ of the pure gravity gradient (GG) dumbbell. By removing the effect of SRP, the present analysis is no longer limited to Sun-centred orbits and the scope of potential applications can be extended to orbits around small bodies such as asteroids. Figure 3.4 shows the equilibria as a function of the mass ratio κ and tether length ratio λ. In order to magnify the effect of the gravity gradient on unequal masses, very high values of λ are chosen for the purpose of illustration. The tether length is set to be in the same order of magnitude as the orbit radius and a set of different tether length ratios $\lambda = 0.1, 0.5, 1, 2, 3, 4, 5, 20$ is chosen. As can be seen in the figure, for a relatively small tether length ($\lambda = 0.1$), $\gamma_{eq,GG}$ deviates only slightly from ±90 degrees, even for small/high mass ratios. However, when increasing λ, the effect of unequal masses ($\kappa \neq 0.5$) is to shift the unstable equilibria within the range of $[\pm 75.52, \pm 104.48]$ degrees in the case of $\lambda = 0.5$ and within $[\pm 60, \pm 120]$ degrees in the case of $\lambda = 1$. When further increasing the tether length ratio to $\lambda \geq 2$, the dumbbell can even obtain any unstable equilibrium $\gamma_{eq,GG} \in [-180, 180]$ degrees, depending on the chosen mass ratio. Clearly, due to the planar problem investigated in this chapter,

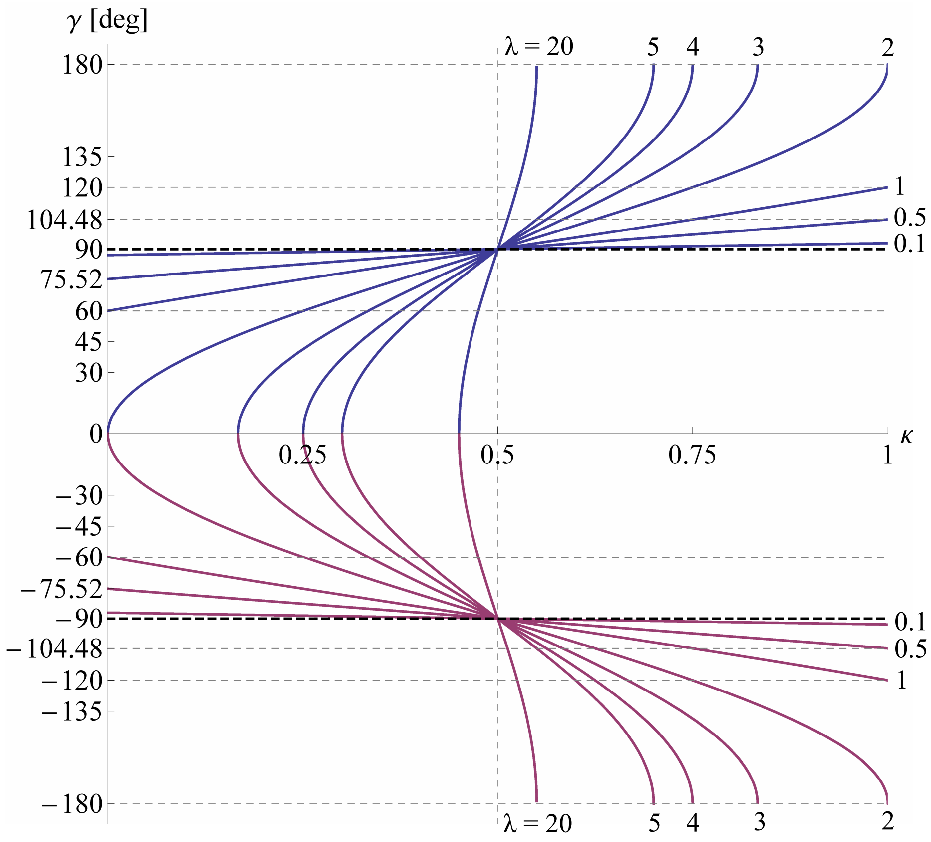

Figure 3.4: Unstable equilibria $\gamma_{\mathrm{eq,GG}}$ of the pure gravity gradient dumbbell as a function of mass ratio κ and for different tether length ratios $\lambda = 0.1, 0.5, 1, 2, 3, 4, 5, 20$.

values of $\lambda \geq 1$ are theoretical due to the high risk of collision with the central body. The effect of large values of λ on the unstable equilibria is usually not accounted for in the literature investigating the pure gravity gradient dumbbell [100]. However, for orbits centred around an asteroid, the tether length would only have to be in the range of a few kilometres.

3.3.1 Maintaining dumbbell system on circular orbit using SRP

The decoupled attitude EOM, Eq. (3.12), is only valid under the assumption that the c.m. remains on a circular orbit with uniform orbital rate $\omega_0 = \dot{\nu}_0$. This condition is satisfied when introducing a large central mass, as shown above, or approximated when assuming a small tether length, thus $\lambda \ll 1$. However, regardless of the tether length, the radial outward SRP force will always perturb the circular Keplerian motion of the dumbbell: the SRP forces decrease the effective solar gravity experienced by the two masses, as shown earlier by the introduction of the effective gravitational parameter

$\tilde{\mu} = \mu(1-\beta_i)$. The effective orbital rate $\tilde{\omega} = \sqrt{\tilde{\mu}/R_0^3} < \omega_0$ now corresponds to a circular non-Keplerian orbit in the combined gravitational and SRP forces [2]. For the dumbbell to remain on this non-Keplerian orbit constraints on β_1 and β_2 are derived that allow circular orbital motion for any given attitude γ. This reintroduces the coupling of the orbit and attitude dynamics of the system.

Considering the coupled EOM, Eq. (3.10), without the central mass, thus $M_\mathrm{B} = 0$, and introducing the conditions $\ddot{R} = \dot{R} = 0$, $\ddot{\nu} = 0$ and $\dot{\nu} = \tilde{\omega}$ results in two constraint equations for β_1 and β_2

$$\beta_1 = 1 - \frac{\tilde{\omega}^2}{\mu} R_1^3 \left[\frac{1}{\kappa[1-\lambda(1-\kappa)\cos\gamma] + (1-\kappa)[1+\lambda\kappa\cos\gamma]} \right] = \beta_1(\gamma) \tag{3.20a}$$

$$\beta_2 = 1 - \frac{\tilde{\omega}^2}{\mu} R_2^3 \left[\frac{1}{\kappa[1-\lambda(1-\kappa)\cos\gamma] + (1-\kappa)[1+\lambda\kappa\cos\gamma]} \right] = \beta_2(\gamma) \tag{3.20b}$$

Note that the above equations are coupled through the angle γ. Figures 3.5 and 3.6 show the constrained $(\beta_1, \beta_2)_\gamma$ sets over the range of attitude angles $\gamma \in [-180, 180]$ degrees for the reference dumbbell. The concept is further illustrated by a family of circular non-Keplerian orbits with decreasing orbital rates $\tilde{\omega}_i \leq \omega_0$, starting with the nominal rate $\omega_0 = \sqrt{\mu/R_0^3}$ for the circular Keplerian orbit. The figures show that for ω_0 the orbit cannot be maintained for any given attitude, since β_i becomes negative for some intervals of γ, which is not a physical solution. When decreasing the orbital rate to $\tilde{\omega}_1 = (1-1.5\times10^{-7})\,\omega_0$, $\tilde{\omega}_2 = (1-3.5\times10^{-7})\,\omega_0$ and $\tilde{\omega}_3 = (1-5.0\times10^{-7})\,\omega_0$, the region of feasible attitudes can be increased gradually, as can be seen in Figs. 3.5 and 3.6. For $\tilde{\omega} \leq \tilde{\omega}_3$, all equilibrium attitudes are possible.

Adding the new β-constraints to the previously defined β-sets that create a respective unstable equilibrium attitude γ_eq, as seen before in Fig. 3.3, results in Fig. 3.7. While the original $(\beta_1, \beta_2)_{\gamma_\mathrm{eq}}$ sets in the decoupled problem are lines for $\beta_i \in [0, 1]$, the constraints that reintroduce the orbit/attitude coupling now restrict the sets to a single point for each γ_eq, depending on the chosen orbit rate $\tilde{\omega}$ of the non-Keplerian circular orbit.

3.4 Attitude dynamics and control of dumbbell using SRP

This section further analyses the decoupled problem, Eq. (3.12), for lightness numbers that satisfy the constraints in Eq. (3.20) such that the c.m. of the dumbbell will remain on a circular non-Keplerian orbit with orbital rate $\tilde{\omega} < \omega_0$.

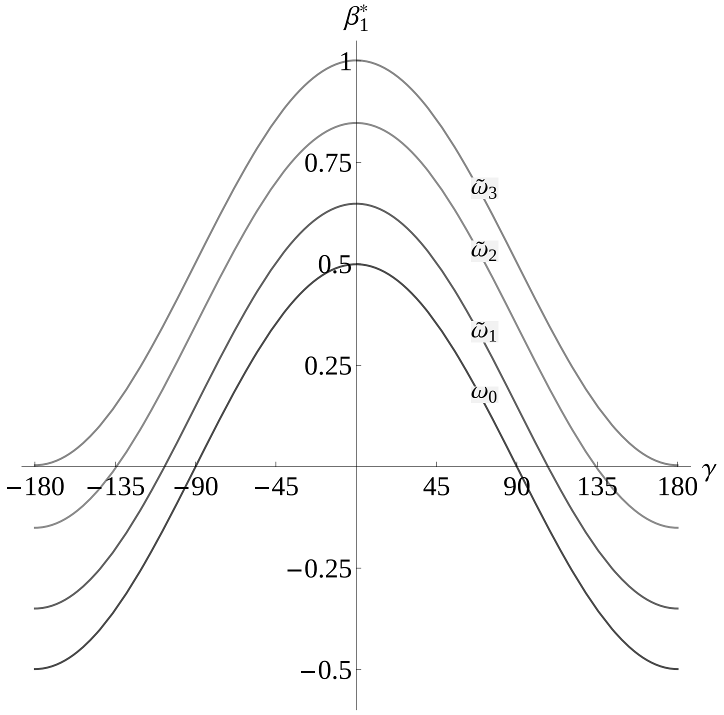

Figure 3.5: Constrained β_1^* for reference dumbbell to maintain a circular non-Keplerian orbit with orbital rates $\tilde{\omega}_i$ for given attitude γ.

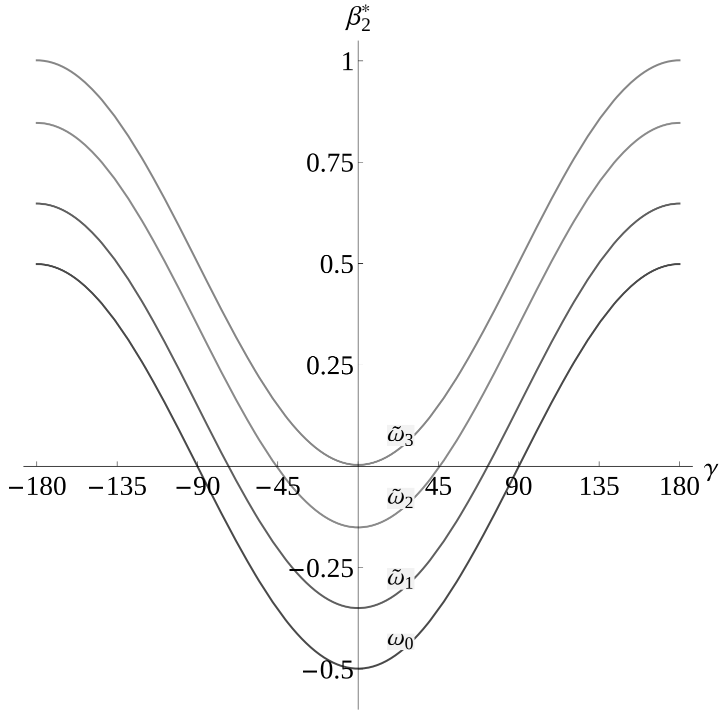

Figure 3.6: Constrained β_2^* for reference dumbbell to maintain a circular non-Keplerian orbit with orbital rates $\tilde{\omega}_i$ for given attitude γ.

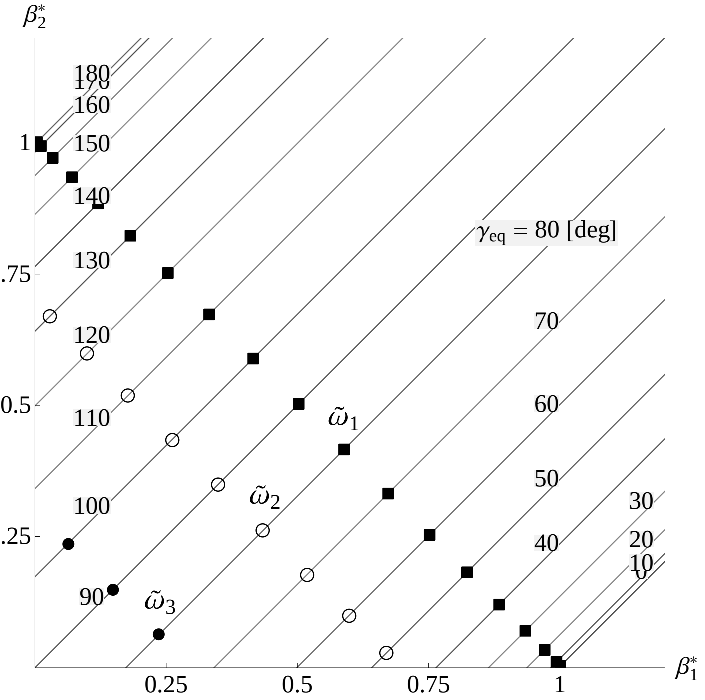

Figure 3.7: Possible $(\beta_1^*, \beta_2^*)_{\gamma_{\mathrm{eq}}}$ sets for reference dumbbell to create a respective γ_{eq} and superimposed β-constraints for different circular non-Keplerian orbits with reduced orbital rates.

3.4.1 Phase space of the decoupled problem

The Hamiltonian of the decoupled system is found using one generalised coordinate $q_{1,\mathrm{dec}} = \gamma$ in the rotating orbit frame $\mathcal{O}\colon(\mathbf{r}, \boldsymbol{\nu})$, according to Fig. 3.1. After dividing by $\frac{1}{2}(m_1+m_2)\omega_0^2 l^2$, the non-dimensional Hamiltonian can be written as [36]

$$\hat{H}_{\mathrm{dec}} = \frac{2}{(m_1+m_2)\omega_0^2 l^2}\left[\frac{1}{2}\frac{m_1 m_2 l^2}{m_1+m_2}(\dot{\gamma}^2-\omega_0^2) - \frac{\mu m_1(1-\beta_1)}{R_1} - \frac{\mu m_2(1-\beta_2)}{R_2}\right] \tag{3.21}$$

Since the decoupled Hamiltonian is a constant of motion, for each value of $\hat{H}_{\mathrm{dec}}$, the motion of the system is represented by a two-dimensional phase space $(\gamma, \dot{\gamma})$ [96] with free parameters β_1 and β_2. Figure 3.8 shows the iso-energy curves in the phase space for the reference dumbbell and for particular values of the lightness numbers. The arrows indicate the direction of motion along a curve. Whenever the curves are closed, they correspond to librations around the equilibrium point, while open curves correspond to rotations. Two superimposed phase spaces for different β-sets and the respective location of the stable and unstable equilibria are visible. The first set $(\beta_1, \beta_2)_{\mathrm{A}} = (0, 0)$ (black solid curves) corresponds to the pure gravity gradient dumbbell without SRP, showing the well-known unstable equilibria at +/-90 degrees and the stable equilibria

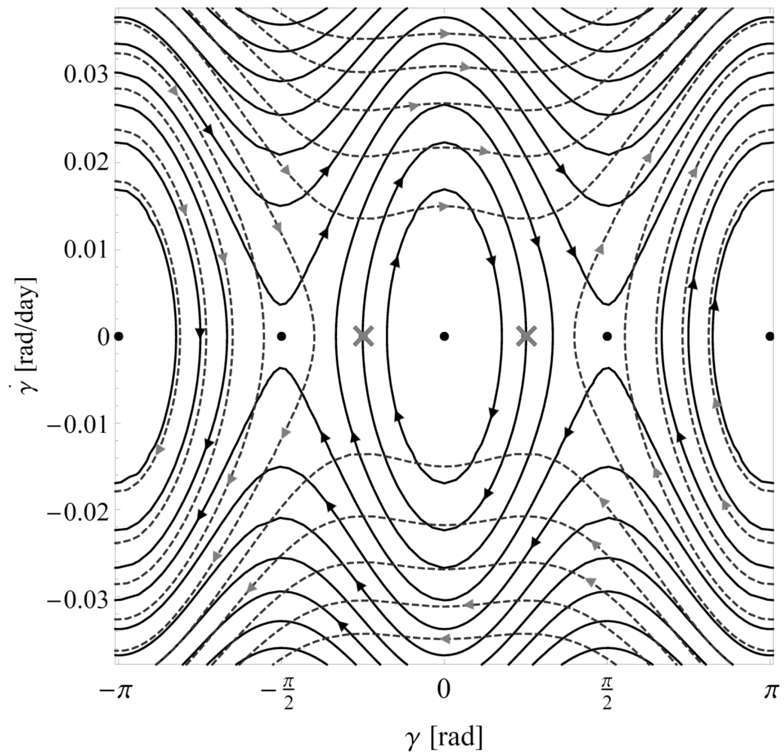

Figure 3.8: Superimposed phase spaces $(\gamma, \dot{\gamma})$ of pure gravity gradient dumbbell with $(\beta_1, \beta_2)_\mathrm{A} = (0, 0)$ (black solid curves) and including SRP with lightness numbers $(\beta_1^*, \beta_2^*)_\mathrm{B} = (0.86, 0.15)$ (dashed grey curves).

at 0 and ±180 degrees (black points). The second set B (grey dashed curves) is chosen according to the derived β-constraints. Here, as an example, the lightness numbers are selected such that they shift the unstable equilibria to ±45 degrees (grey crosses). For a chosen orbit of radius $R_0 = 1\,\mathrm{AU}$ and orbital rate $\omega_0 = 0.0172$ rad/day, the non-Keplerian orbit in terms of orbital rate $\tilde{\omega}$ and the corresponding set $(\beta_1, \beta_2)_\mathrm{B}$ that creates the ±45 degree equilibria can be obtained from Fig. 3.7, or likewise Eq. (3.20). As found above, an orbit rate of $\tilde{\omega}_3 = (1{-}5.0{\times}10^{-7})\,\omega_0$ allows for positive β-sets in the full range of attitudes between $[-180, 180]$ degrees. Accordingly, the resulting β-set is $(\beta_1^*, \beta_2^*)_\mathrm{B} = (0.86, 0.15)$.

3.4.2 Motion in phase space

The phase space of the system is characteristic for a particular β-set. Switching to another set, the phase space and the respective equilibria change accordingly, as shown above. This property of the system can be exploited to find heteroclinic connections between equilibria of different phase spaces. By providing a qualitative switching law

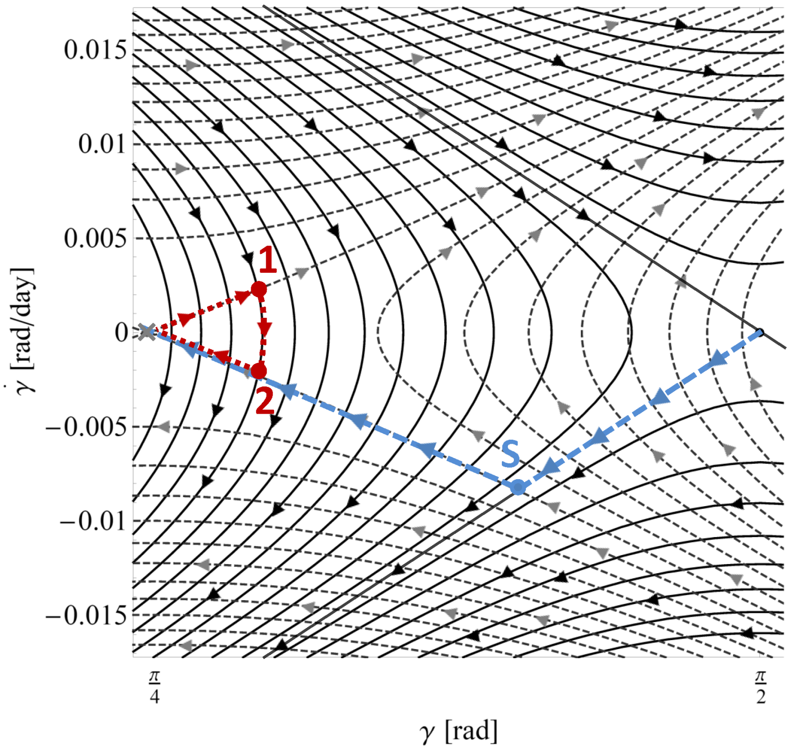

Figure 3.9: Detail view of superimposed phase spaces A and B from Fig. 3.8. Two possible sequences are highlighted: attitude change between unstable equilibria (blue dashed path) and control sequence around an unstable equilibrium (red dotted path).

between different β-sets, this section shows how the attitude of the dumbbell can be changed and controlled in the vicinity of a desired (unstable) attitude.

When again inspecting Fig. 3.8, possible controlled sequences in the phase space in order to change the dumbbell attitude can be identified. Whenever the dumbbell is in a state at (or close to) an unstable equilibrium (saddle), there a two unstable manifolds for the system to move away from the saddle. The other two stable manifolds always lead towards the unstable point, as can be seen in Fig. 3.9, which shows a detail view of the two superimposed phase spaces A and B from Fig. 3.8. For example, the system can move along the bold dashed path away from the $\pi/2$ saddle, as indicated through the arrows in the figure. Likewise, there are also two stable manifolds leading towards the $\pi/4$ saddle of the second phase space (dashed grey lines). When switching between the previously chosen sets $(\beta_1, \beta_2)_\mathrm{A}$ and $(\beta_1, \beta_2)_\mathrm{B}$, at the point in phase space indicated with a bold ‘S’, the dumbbell will consequently change its equilibrium attitude from $\pi/2$ to $\pi/4$, when following the dashed path. In this way, intersections between manifolds of different phase spaces can be exploited. In order to further control the dumbbell in the vicinity of an unstable saddle point, a control sequence such as the one indicated with the dark dotted path can be used. When the system initially moves away from the saddle on one of the outgoing manifolds (within phase space B), switching to set A (black solid curves) at the point marked with a bold '**1**' will let it move along a closed path around the stable centre of phase space A. When it reaches point '**2**', which is the crossing with the ingoing manifold, switching back to set B will complete a closed loop around the desired unstable equilibrium of $\pi/4$.

3.5 Chapter summary

In this chapter, the concept of optical control has been considered for a long-baseline tethered spacecraft configuration. By using an analytical Hamiltonian approach, the planar attitude dynamics of the classical rigid-body dumbbell system including SRP forces on the tip masses have been investigated for Sun-centred orbits. The equations of motion for the coupled orbit/attitude dynamics of the system have been derived and decoupled through the use of a large central mass. The additional mass enabled a stability analysis of the system's attitude, with the lightness numbers of the tip masses as free control parameters. It has been shown that introducing SRP creates artificial unstable equilibria that are different from those of the pure gravity gradient dumbbell. In particular, by controlling the lightness numbers of the tip masses, equilibrium attitudes at an arbitrary angle, relative to the local vertical, can be created.

In addition, the influence of unequal tip masses and extremely long tethers on the attitude dynamics of the pure gravity gradient dumbbell without SRP have been analysed for orbits around small celestial bodies such as asteroids. For tether lengths up to the same order of magnitude as the orbit radius, the imbalance of gravity forces again creates unstable equilibrium attitudes in the interval of $[\pm 60, \pm 120]$ degrees. Such long tethers are usually not accounted for in the literature. However, for orbits centred around an asteroid, the tether length would only have to be in the range of a few kilometres.

For the dumbbell problem including SRP, optical control of the dumbbell attitude has been demonstrated through changing the lightness numbers, exploiting the heteroclinic connections in the phase space of the problem. The additional SRP forces perturb the circular Keplerian motion of the system around the central body. Accordingly, coupling of the orbit and attitude dynamics has been reintroduced by deriving constraints for the lightness numbers, showing that the dumbbell can be maintained on a circular non-Keplerian orbit for arbitrary attitudes using light pressure. This supports the concept of using SRP for attitude control of tethered gossamer systems at relatively low cost, since the lightness numbers, or surface reflectivities, respectively, can in principle be changed using electro-chromic coatings. Therefore, no mechanical systems or thrusters are required to maintain, for example, a fixed observation attitude. This chapter therefore provides the basis for more complex models developed later in the thesis.

Chapter 4

Optical attitude control of membrane reflectors

In Chapter 3, a reflectivity gradient between the surfaces of two separate, but connected units has been used to demonstrate the potential of manipulating SRP for optical control of a spacecraft attitude. Following these results, the concept of exploiting variable optical surface properties to modulate light pressure shall now be introduced for a large gossamer membrane spacecraft. In particular, the attitude dynamics of a flat rigid membrane with a variable surface reflectivity distribution will be investigated in this chapter. When changing the reflectivity coefficient across the surface, the SRP forces (and torques) acting on this type of spacecraft can be exploited to control the spacecraft attitude without the use of mechanical actuators or thrusters, as proposed in Section 1.1.4. Three different reflectivity distribution models, of increasing complexity, will be considered for the surface reflectivity: the first model introduces a continuous reflectivity distribution across the surface (Section 4.1); the second divides the surface into two regions of high and low reflectivity (Section 4.2); and the third models the surface as a discrete array of multiple reflectivity cells (Section 4.3). Each distribution model will be applied to perform basic attitude manoeuvres and the conclusions will be summarised in Section 4.4.

4.1 Continuous reflectivity distribution

In this first section, a continuous reflectivity distribution across the surface of a large gossamer membrane structure is considered for optical control of the spacecraft attitude. To this end, a square membrane reflector is modelled as an ideally flat rigid surface, as

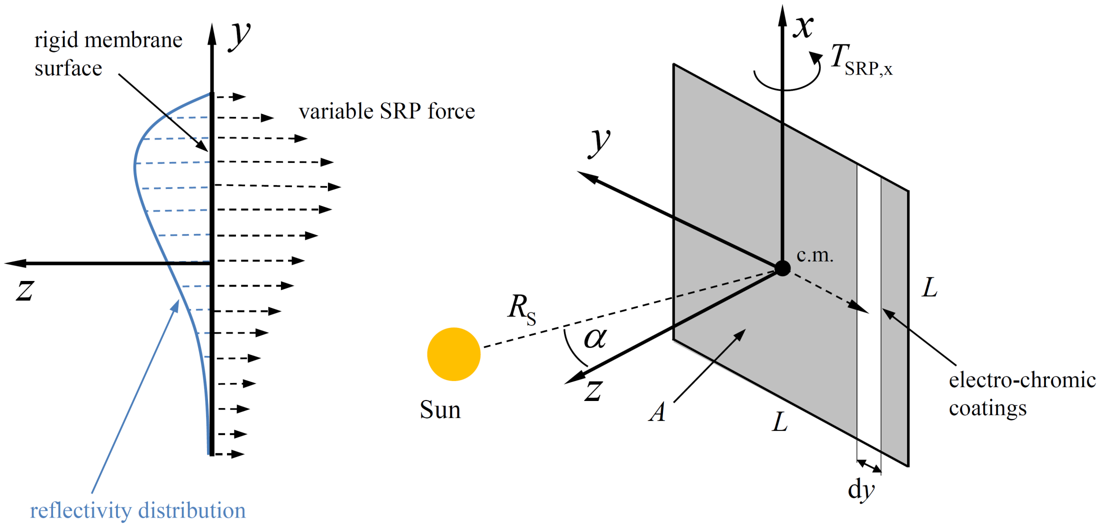

Figure 4.1: Square membrane reflector with continuous reflectivity distribution across the surface (left) and membrane reflector model with infinitesimal electro-chromic strip (right).

shown in Fig. 4.1. A continuous reflectivity distribution is approximated through the assumption that the entire membrane surface A is covered with strips of infinitesimally narrow electro-chromic coating elements, as introduced in Section 2.4. Each strip can change its reflectivity in the interval $\rho \in [0, 1]$ and thus, continuously between diffuse and specular reflection, as previously introduced in Section 2.2.2, while the additional mass and thickness of the coating elements are neglected.

Throughout this chapter, a body-fixed Cartesian coordinate frame $\mathcal{B} := (\mathbf{x}, \mathbf{y}, \mathbf{z})$, aligned with the body's principal axes of inertia, is used to represent the reflector spacecraft, with $(\mathbf{x}, \mathbf{y})$ in the membrane plane and $\mathbf{z}$ along the surface normal, according to Fig. 4.1. The surface cone angle α denotes the angle between the Sun-reflector line R_{S} and the membrane plane normal. When changing the reflectivity of a rectangular surface element of area $\mathrm{d}A = L\,\mathrm{d}y$, the difference in SRP force across the surface creates a torque $T_{\mathrm{SRP,x}}$ about the spacecraft $\mathbf{x}$-axis. For now, a constant reflectivity is assumed in the element's $\mathbf{x}$-axis such that no torque is generated about the spacecraft $\mathbf{y}$-axis.

This optical steering method is further demonstrated by controlling the spacecraft attitude in a planar low Earth orbit (LEO). In particular, the concept is applied to counteract the gravity-gradient torques acting on the structure in orbit. It shall be demonstrated that a constant Sun-pointing attitude can be maintained along the orbit, using the proposed concept. To this aim, the c.m. is assumed to move on a fixed circular LEO in the ecliptic plane, as shown in Fig. 4.2, while air drag and solar eclipses are

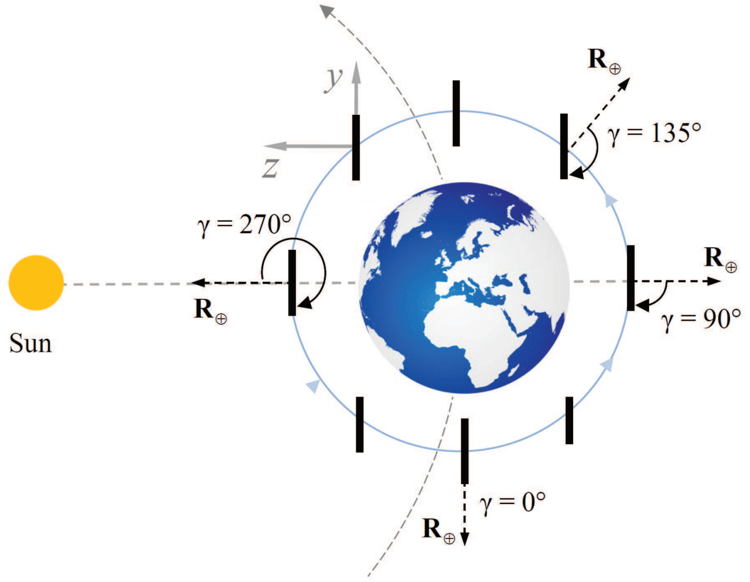

Figure 4.2: Constant Sun-pointing attitude of membrane reflector spacecraft on Earth-centred circular LEO of 400 km altitude in the ecliptic plane.

ignored for illustration. The reflector shall be always Sun-pointing along the orbit, hence a constant surface cone angle $\alpha = 0$ deg is assumed. In this preliminary analysis, the spacecraft **x**-axis is constrained to be always perpendicular to the ecliptic plane. This allows only one degree of rotational freedom, while rotation about the **y** and **z** axes is omitted.

4.1.1 Gravity-gradient torque compensation on planar circular orbit

The GG torque along the orbit depends on the angle γ between the reflector plane and the Earth radial direction $\mathbf{R}_{\oplus}$, according to Fig. 4.2, where γ coincides with the dumbbell attitude angle used in Section 3.2.2. The GG torque can be approximated using the well-known relation [101]

$$T_{\mathrm{GG,x}} = 3\frac{\mu_{\mathrm{E}}}{R^3}\sin\gamma\cos\gamma\,(I_{\mathrm{zz}} - I_{\mathrm{yy}}) \tag{4.1}$$

with $\mu_{\oplus} = 3.9860 \times 10^6\ \mathrm{km}^3/\mathrm{s}^2$ the Earth's gravitational parameter and $R = r_{\oplus} + h_{\oplus}$ the radial distance of the spacecraft c.m. from the Earth's centre, where $r_{\oplus} = 6,371\,\mathrm{km}$ is the Earth's radius and $h_{\oplus}$ the orbit altitude. A variable reflectivity distribution $\rho(y)$ in the surface **y**-direction is now assumed to counteract this torque. The SRP force and torque about the spacecraft c.m. are calculated using the simplified SRP model, as previously introduced in Section 2.2.2. According to Eq. (2.7) and assuming a constant solar distance $R_{\mathrm{S}} = 1$ AU along the orbit, the solar radiation pressure p_{SRP} can be

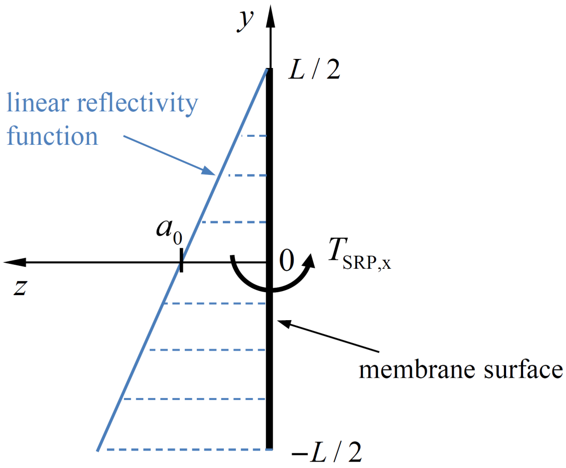

Figure 4.3: Linear reflectivity function (in y-direction) across the membrane surface.

written as

$$p_{\mathrm{SRP}} = p_0 \left[1 + \rho(y)\right] \cos^2 \alpha \tag{4.2}$$

As seen before, the forces induced by SRP can now be modified directly when changing the surface reflectivity. When considering again Fig. 4.1, the incremental SRP force and torque acting on a rectangular surface element can be written as

$$\mathrm{d}F_{\mathrm{SRP}} = p_0 L \left[1 + \rho(y)\right] \cos^2 \alpha \; \mathrm{d}y \tag{4.3a}$$

$$\mathrm{d}T_{\mathrm{SRP,x}} = p_0 L y \left[1 + \rho(y)\right] \cos^2 \alpha \; \mathrm{d}y \tag{4.3b}$$

When further introducing a linear reflectivity function in the **y**-direction of the form

$$\rho(y) = a_0 + a_1 \, y \tag{4.4}$$

according to Fig. 4.3, Eqs. (4.3a) and (4.3b) can be integrated over the interval $[-L/2, L/2]$, while assuming $\alpha = 0$ along the orbit due to the Sun-pointing constraint. The resulting SRP force and torque are found to be

$$F_{\mathrm{SRP}} = p_0 L \int_{-L/2}^{L/2} \left[1 + a_0 + a_1 \, y\right] \mathrm{d}y \; = p_0 L^2 \left[1 + a_0\right] \tag{4.5}$$

$$T_{\mathrm{SRP,x}} = p_0 L \int_{-L/2}^{L/2} y \left[1 + a_0 + a_1 \, y\right] \, \mathrm{d}y = \frac{1}{12} p_0 L^4 a_1 \tag{4.6}$$

It can be seen that the magnitude of the SRP force is only a function of the coefficient a_0. Furthermore, the SRP torque only depends on the slope a_1 of the linear reflectivity function, thus on the difference of the SRP force on the left and right hand side of the reflector. If the forces are equal on both sides ($a_1 = 0$), the torque on the spacecraft is zero, regardless of the absolute value of the SRP force, as determined by a_0. Clearly, the maximum torque occurs when the reflectivity reaches its maximum, $\rho = 1$, at one surface edge, while $\rho = 0$ at the other edge. Accordingly, the absolute coefficient is $a_0 = 0.5$, since it is the intersection with the $\mathbf{z}$-axis at the centre of the surface. Inserting this into Eq. (4.4), together with the condition at the edge, results in $a_1 = 1/L$. Furthermore, inserting into Eq. (4.6) yields the maximum optical torque

$$T_{\mathrm{SRP,x,max}} = \frac{1}{12} p_0 L^3 \tag{4.7}$$

Equation (4.6) represents the SRP torque that must be generated in order to counteract the gravity-gradient torque $T_{\mathrm{GG,x}}$ along the orbit, thus $T_{\mathrm{SRP,x}}$ must always be equal to $T_{\mathrm{GG,x}}$. As a result, the coefficients a_0 and a_1 of the linear function $\rho(y)$ that are required to counteract the gravity-gradient torque (or any other disturbance torque about the spacecraft $\mathbf{x}$-axis) can be calculated using the following equations

$$a_1 = \frac{12 T_{\mathrm{GG,x}}}{p_0 L^4}, \qquad a_0 = \frac{F_{\mathrm{SRP}}}{p_0 L^2} - 1 \tag{4.8}$$

While a_1 is determined by the local torque $T_{\mathrm{GG,x}}$ that needs to be compensated, a_0 is in principle only constrained by the maximum possible SRP force $F_{\mathrm{SRP,\,max}} = 2p_0L^2$, for which $a_0 = 1$ and thus, $\rho(y) = 1$ and is constant across the surface (assuming $a_1 = 0$). However, a reflectivity gradient $a_1 \neq 0$ is necessary to create a torque, while at the same time $\rho(y) \leq 1$ (maximum reflectivity) must be satisfied across the entire surface. The minimum value of a_0 is determined by the additional condition $\rho(L/2) = 0$ or $\rho(-L/2) = 0$ at the edge of the reflector. Inserting this into the linear reflectivity function, Eq. (4.4), results in $a_{0,\mathrm{min}} = \pm a_1 L/2$, depending on the sign of the torque that needs to be created. Since a_1 only depends on the external torque, $a_{0,\mathrm{min}}$ defines the minimum reflectivity distribution in terms of the smallest values of ρ across the surface.

In order to demonstrate the concept, a sample reflector configuration with an arbitrary membrane thickness $t = 2.5 \times 10^{-6}$ m and edge length $L = 50$ m is chosen, ideally without assembly or payload masses in this initial analysis. The film material employed is Kapton, as previously introduced in Section 1.1.2. Using the density of this film material ($\tau = 1,572$ kg/m^3), the membrane mass m results in only 9.83 kg, with quite low mass moments of inertia $I_{\mathrm{xx}} = I_{yy} = 2046.9$ kg m^2 and $I_{\mathrm{zz}} = 4093.8$ kg m^2 about the principal body axes. This preliminary configuration is orbiting on a fixed circular

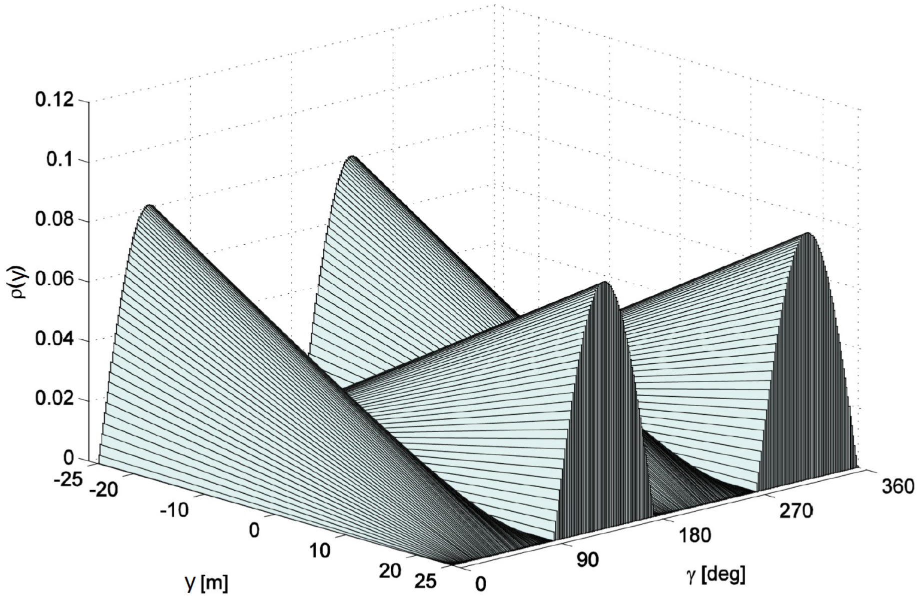

Figure 4.4: Minimum reflectivity distribution across 50 m edge-length membrane surface (in y-direction) to counteract gravity gradient in LEO during one orbit

LEO of 400 km altitude, where the maximum GG torque acting on the membrane is of the order $T_{\mathrm{GG,x}} = 4\times10^{-3}$ Nm about the x-axis, according to Eq. (4.1).

Figure 4.4 shows the resulting reflectivity distribution $\rho(y)$ across the membrane as a function of the spacecraft attitude angle γ during one revolution along the orbit. It can be seen that the necessary reflectivity to balance the gravity-gradient torque is relatively small compared to the maximum reflectivity $\rho_{\mathrm{max}} = 0.6$ that can be achieved with currently developed electro-chromic devices (Section 2.4). This indicates that for the chosen application to counteract gravity gradient torques, the proposed optical steering method has not reached its full potential. According to Eq. (4.7), the maximum control torque that can be achieved for the current reflector, is $T_{\mathrm{SRP,x}} = 0.048$ Nm, thus 12 times larger than the maximum gravity gradient torque in LEO. However, it shall be noted that only the membrane's mass moments of inertia have been considered in this preliminary analysis. Therefore, the final mass moments of inertia of the real reflector spacecraft, including all subsystems, membrane support structure and payload, are expected to be much larger. This investigation in terms of counteracting gravity gradient torques in LEO shall be subject to future analysis. However, in the following sections 4.2 and 4.3, respectively, more complex reflectivity distribution models will be introduced and demonstrated on a realistic reflector spacecraft configuration with much larger mass moments of inertia.

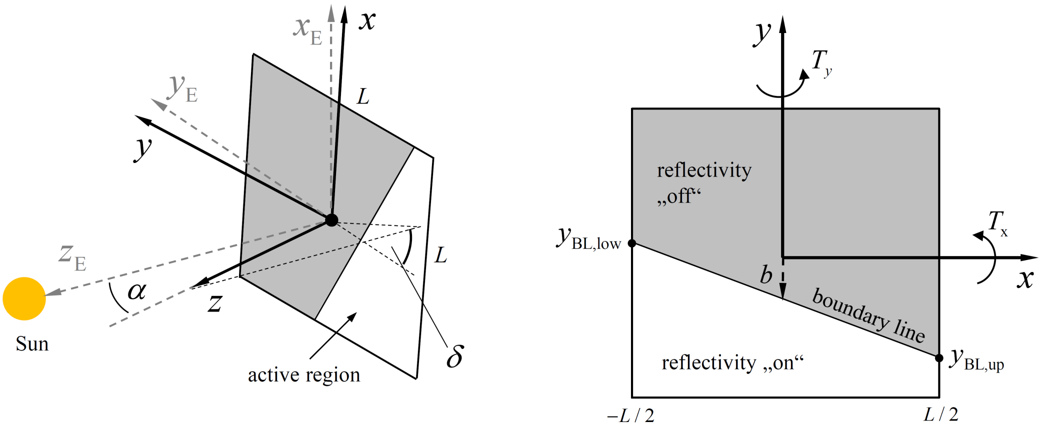

Figure 4.5: Square membrane reflector with two constrained reflectivity regions controlled by moving a boundary line between two states, 'on' (specular reflection) and 'off' (diffuse reflection), and torques created about the in-plane spacecraft axes.

4.2 Constrained high/low reflectivity region

In this section, a more realistic approach is considered, using two constrained regions of active and inactive (on/off) surface reflectivity, separated by a variable boundary line, as shown in Fig. 4.5. Instead of varying ρ in the interval $[0, 1]$, as assumed in Section 4.1, the electro-chromic coatings in each region are now restricted between two states, either 'on' ($\rho_{\max} = 1$) or 'off' ($\rho_{\min} = 0$). By controlling the position of the boundary line across the surface, a wide range of torque vector directions in the reflector plane $(\mathbf{x}, \mathbf{y})$ can be generated. However, torques perpendicular to the surface are not possible. This is due to the simplified SRP model employed, which assumes that the forces due to light pressure are always perpendicular to the surface, according to Section 2.2.2. The potential of this approach is demonstrated in this section for two-axis attitude control of the spacecraft in a Sun-centred orbit.

The on/off boundary line is described by a linear function

$$y_{\mathrm{BL}}(x) = ax + b \tag{4.9}$$

in the x-direction across the membrane, with an arbitrary slope coefficient a and offset coefficient b, describing its vertical offset from the x-axis. Furthermore, two geometrically mirrored on/off cases can be chosen for the electro-chromic coatings above and below the boundary line, as shown in Fig. 4.6. The first case represents an active reflectivity state above the boundary line and inactive below (further named as the 'upper case'), or vice versa, the second case indicates reflectivity 'off' above y_{BL} and 'on' below (termed the 'lower case'). Switching between the two cases only changes the sign of the torques, not their magnitude. The SRP torques now depend on the two coefficients a and b, the cone angle α (i.e. the current surface attitude), and the considered on/off case.

According to Fig. 4.5, the in-plane SRP torque components in $\mathbf{x}$ and $\mathbf{y}$-direction at 1 AU solar distance can be written as

$$\mathbf{T}_{\mathrm{x}} = -p_0 \cos^2 \alpha \int_{-L/2}^{L/2} \int_{ax+b}^{L/2} y \,\mathrm{d}y\mathrm{d}x\, \mathbf{x} \tag{4.10a}$$

$$\mathbf{T}_{\mathrm{y}} = \quad p_0 \cos^2 \alpha \int_{-L/2}^{L/2} \int_{ax+b}^{L/2} x \,\mathrm{d}y\mathrm{d}x\, \mathbf{y} \tag{4.10b}$$

when assuming the ‘upper case’, thus only the electro-chromic coatings above the boundary line are active. When the coating elements are switched into the ‘lower case’, the limits of both inner integrals need to be inverted to $[-L/2, ax+b]$, which is equivalent to changing the signs of the torques.

When integrating Eqs. (4.10a) and (4.10b), seven torque cases have to be considered, depending on the intersection of the boundary line with the limits of the surface domain in $\mathbf{x}$-direction, $-L/2$ and $L/2$, as shown in Fig. 4.7 for illustration. Note that the coloured areas in the figure do not represent the activation state of the two reflectivity regions above and below the boundary line. In order to assist the computation of each

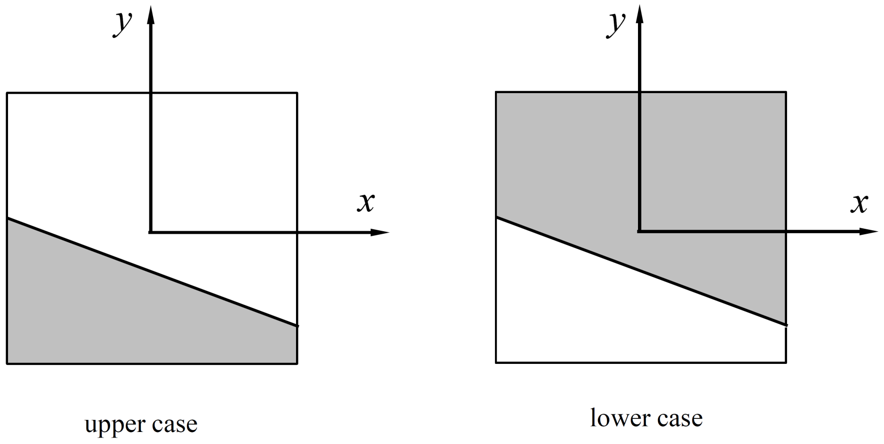

Figure 4.6: Possible on/off cases for the two reflectivity regions on the membrane surface, separated by a movable boundary line.

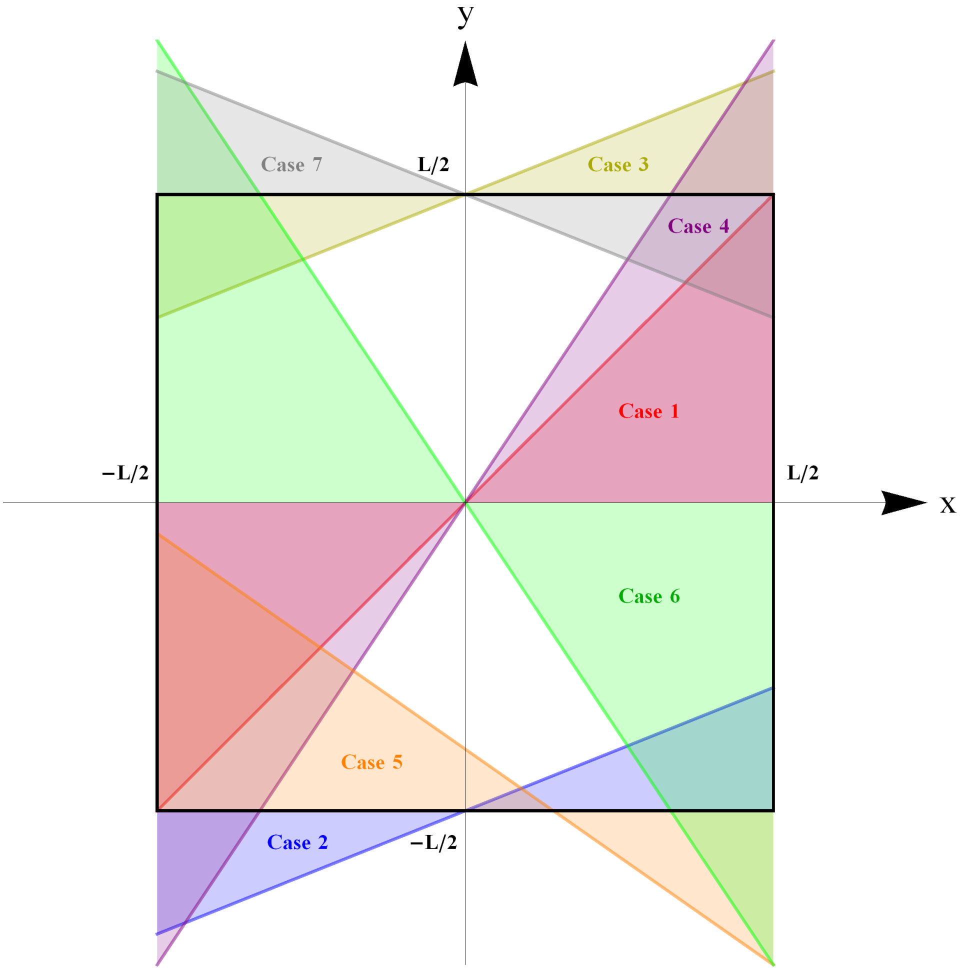

Figure 4.7: Schematic representation of torque cases, depending on the position of the boundary line across the membrane surface.

torque case, the following conditionals are introduced at the edges of the membrane

$$y_{\mathrm{BL,low}} = -a\left(\frac{L}{2}\right) + b \lesseqgtr \pm\frac{L}{2} \tag{4.11a}$$

$$y_{\mathrm{BL,up}} = \quad a\left(\frac{L}{2}\right) + b \lesseqgtr \pm\frac{L}{2} \tag{4.11b}$$

The above conditionals are simply the intersections of the boundary line with each membrane edge in y-direction, as shown in Fig. 4.5. For example, if the coefficients of the boundary line are chosen such that $-L/2 \leq y_{\mathrm{BL,low}} \leq L/2$ and $-L/2 \leq y_{\mathrm{BL,up}} \leq L/2$, the resulting torques are of type ‘Case 1’, as shown in Fig. 4.7.

After defining all seven cases accordingly, analytic expressions for the optical torques can be found. In particular, a set of boundary equations for a and b can be introduced to identify the torque case for a given boundary line. As a result, the torques are now fully determined by the following conditional scheme, given here for the ‘upper case’, when the surface region above the boundary line is activated (excerpt only)

Case 1 $a \geq 0 \ \wedge \quad L/2(a-1) \leq b \leq L/2(1-a)$ or
$a \leq 0 \ \wedge \ -L/2(a+1) \leq b \leq L/2(a+1)$

$$\mathbf{T}_{\text{x,upper}} = p_0 L^3 \cos^2\alpha \left[\frac{1}{2}\frac{b^2}{L^2} - \frac{1}{8} + \frac{1}{24}a^2\right] \mathbf{x} \tag{4.12a}$$

$$\mathbf{T}_{\text{y,upper}} = \frac{1}{12} p_0 a L^3 \cos^2\alpha \ \mathbf{y} \tag{4.12b}$$

Case 2 $a > 0 \ \wedge \ -L/2(a+1) < b < L/2(1-a) \ \wedge \ b < L/2(a-1)$

$$\mathbf{T}_{\text{x,upper}} = \quad p_0 L^3 \cos^2\alpha \tag{4.13a}$$

$$\left[\frac{1}{6}\frac{b^3}{aL^3} + \frac{1}{4}\frac{b^2}{L^2} - \frac{1}{8}\frac{b}{aL} + \frac{1}{8}\frac{ab}{L} - \frac{1}{16} - \frac{1}{24}\frac{1}{a} + \frac{1}{48}a^2\right] \mathbf{x}$$

$$\mathbf{T}_{\text{y,upper}} = \quad p_0 L^3 \cos^2\alpha \tag{4.13b}$$

$$\left[\frac{1}{6}\frac{b^3}{a^2L^3} + \frac{1}{4}\frac{b^2}{a^2L^2} - \frac{1}{8}\frac{b}{L} + \frac{1}{8}\frac{b}{a^2L} - \frac{1}{16} - \frac{1}{24}a + \frac{1}{48}\frac{1}{a^2}\right] \mathbf{y}$$

The remaining cases can be derived in the same way. Switching from the ‘upper case’ to the ‘lower case’ changes signs in the previous equations such that $\mathbf{T}_{\text{x,lower}} = -\mathbf{T}_{\text{x,upper}}$ and $\mathbf{T}_{\text{y,lower}} = -\mathbf{T}_{\text{y,upper}}$.

In order to demonstrate the concept, a sample reflector configuration with edge length $L = 100\,\text{m}$ is now considered. Including the membrane assembly mass and the payload mass, the total mass of the spacecraft is assumed to be $m = 200\,\text{kg}$. The spacecraft’s total mass moments of inertia are $I_{\text{xx}} = I_{\text{yy}} = 1.67 \times 10^5\ \text{kg}\,\text{m}^2$ and $I_{zz} = 3.34 \times 10^5\ \text{kg}\,\text{m}^2$. The achievable torques, as a function of the boundary line coefficients a, b and for increasing cone angle α, are shown in Fig. 4.8, with the electro-chromic elements activated in the ‘lower case’. As can be seen, this activation state creates a positive $\mathbf{T}_{\text{x}}$ over the entire (a, b)-domain, while the torque magnitude decreases for increasing α. The maximum torque is created for $(a, b) = (0, 0)$, hence for the slope and the vertical offset of $y_{\text{BL}}(x)$ being zero. Clearly, this matches the condition for which all electro-chromic coatings on the lower half of the surface are active. In the **y**-direction,

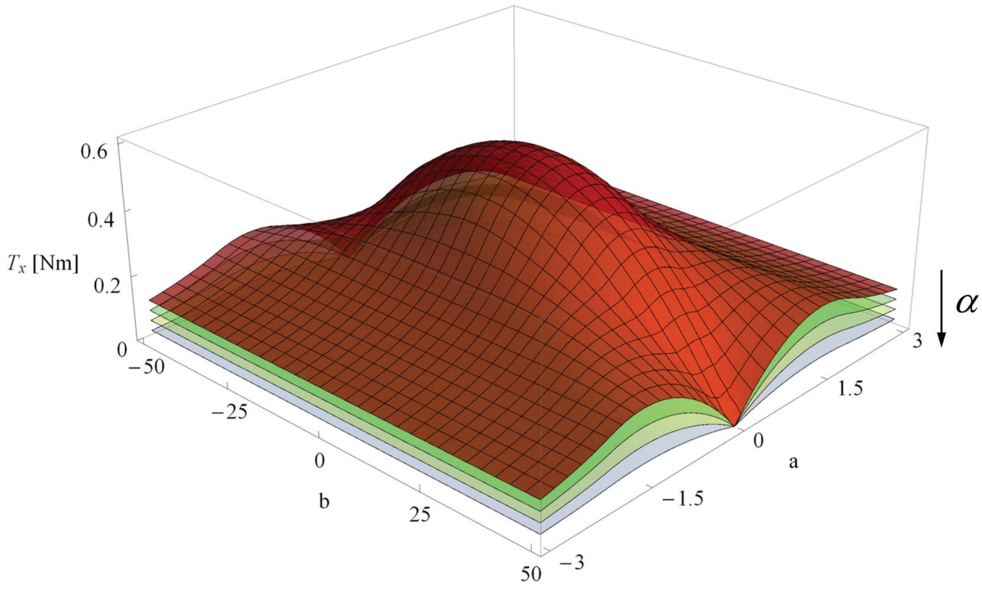

(a) Torque in membrane x-direction

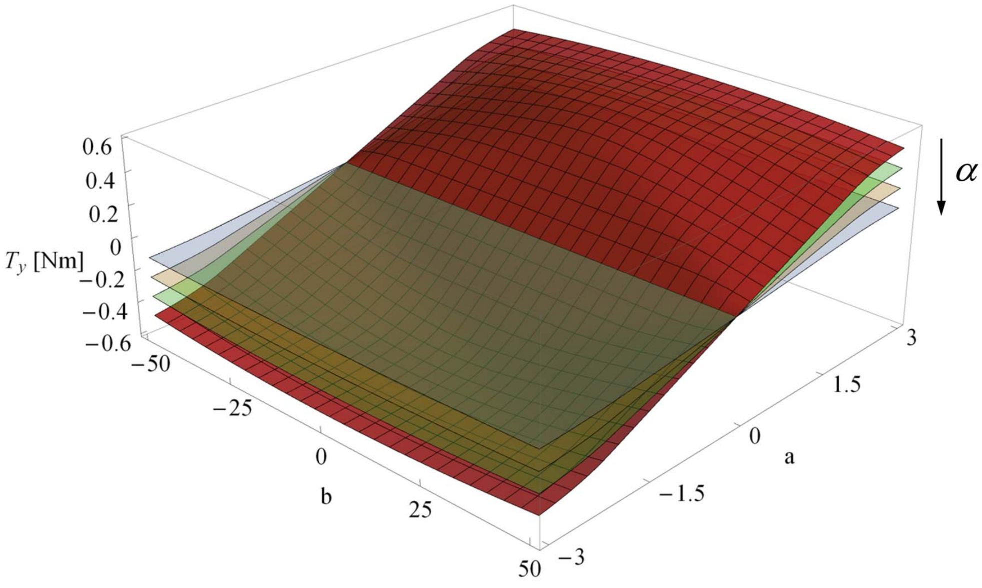

(b) Torque in membrane y-direction

Figure 4.8: In-plane reflector torques over boundary line coefficients a and b and for selected surface cone angles α (coloured). Reflectivity regions activated in 'lower case'.

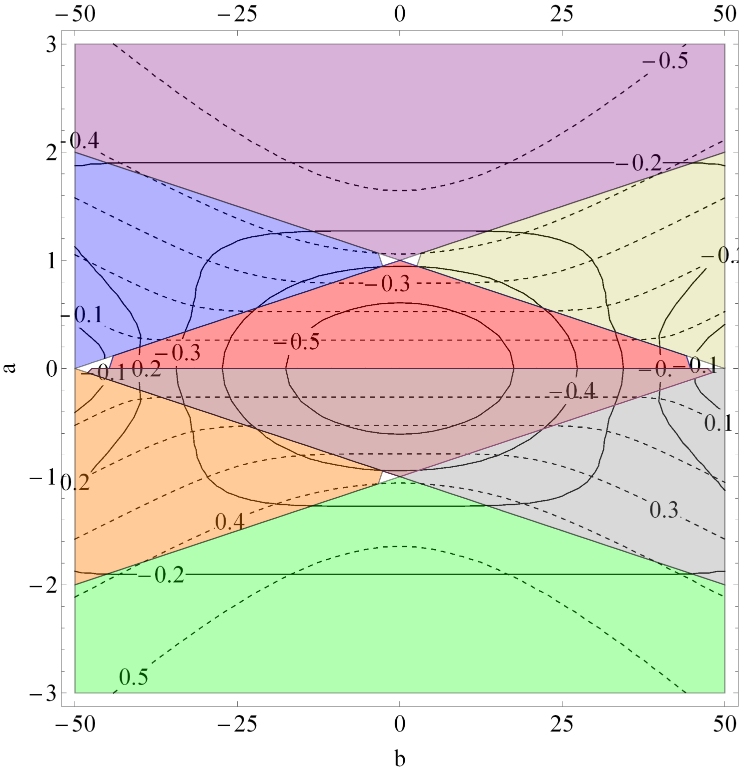

Figure 4.9: In-plane optical torques T_x (solid lines) and T_y (dashed lines) as function of boundary line coefficients a and b, with surface cone angle $\alpha = 0$ deg. Coloured regions indicate each torque case. Constrained reflectivity regions activated in 'upper case'.

the achievable torques mainly depend on the slope a of the boundary line and only to a very limited extent on the offset b. In addition, negative torques can also be created, which is not possible in the **x**-direction for the selected activation state. The maximum torques about both spacecraft axes are found to be $\mathbf{T}_{\mathrm{x,max}} = \mathbf{T}_{\mathrm{y,max}} = \pm 0.57$ Nm, which occurs when all coating elements on one half of the membrane surface are active. For example, applying this torque to the given sample reflector results in a full 360 deg rotation of the spacecraft in approximately 1900 s $\approx$ 32 min.

All seven torque cases over the selected (a, b)-domain are shown in Fig. 4.9 through the use of coloured regions, showing both torque components for a cone angle of $\alpha = 0$ deg and the 'upper case' activation state. Each colour represents the same torque case as in Fig. 4.7. The solid lines in Fig. 4.9 indicate $\mathbf{T}_{\mathrm{x}}$, while the dashed lines characterise $\mathbf{T}_{\mathrm{y}}$. From the figure, the feasible torques for each reflectivity-line in terms of the coefficients a and b can be obtained. It can be seen that no arbitrary torques about both spacecraft axis can be generated, even when staying below $\mathbf{T}_{\mathrm{max}}$ for a chosen reflector configuration.

In the following, the control concept is demonstrated through a sample spacecraft manoeuvre in three rotational degrees of freedom (3 DOF). Therefore, the equations of rotational motion of the reflector spacecraft are derived first.

4.2.1 Rigid-body attitude dynamics

The rigid-body attitude dynamics of the spacecraft are formulated using Euler's equation in quaternion notation [101, 102]. The attitude of the body-fixed frame $\mathcal{B}$ is described with respect to the so-called ecliptic reference frame $\mathcal{E} := (\mathbf{x}_\mathrm{E}, \mathbf{y}_\mathrm{E}, \mathbf{z}_\mathrm{E})$, centred in the spacecraft c.m. on a Sun-centred orbit, as can be seen in Fig. 4.5. The $\mathbf{z}_\mathrm{E}$-axis is oriented towards the Sun, the $\mathbf{y}_\mathrm{E}$ component is always in the ecliptic plane, and $\mathbf{x}_\mathrm{E}$ completes the right-handed coordinate system. It is assumed that attitude changes do not affect the spacecraft's Sun-centred orbit, thus the orbit and attitude motion are decoupled. Choosing quaternions for attitude representation is beneficial compared to other attitude descriptors such as Euler angles, since quaternions have one redundant parameter and thus, no singularities occur. Furthermore, quaternions offer a lower computational effort, since the quaternion algebra does not require trigonometric functions, which appear, for example, in the Euler rotation matrices [101].

The (four-dimensional) attitude quaternion $\bar{q} = (q_1, q_2, q_3, q_4)^\mathrm{T}$ is a hypercomplex number system in the Cartesian basis $(1, \mathbf{i}, \mathbf{j}, \mathbf{k})$ in $\mathbb{R}^4$ [103, 104]. It has the general form

$$\bar{q} = q_1 + q_2\mathbf{i} + q_3\mathbf{j} + q_4\mathbf{k} \tag{4.14}$$

with four real numbers q_i, termed the components of $\bar{q}$, and the upper $(\bar{\ })$ denoting a quaternion vector. Since the subspace $(\mathbf{i}, \mathbf{j}, \mathbf{k})$ represents a basis in $\mathbb{R}^3$, the components of the vector $\mathbf{q} = (q_2, q_3, q_4)^\mathrm{T}$ can be regarded as the vector component and q_1 as the scalar component of $\bar{q}$. Following the derivation given in the Appendix A, the quaternion can be rewritten as

$$\bar{q} = \cos\left(\frac{\theta}{2}\right) + \big(a_\mathrm{x}\mathbf{i} + a_\mathrm{y}\mathbf{j} + a_\mathrm{z}\mathbf{k}\big)\sin\left(\frac{\theta}{2}\right) \tag{4.15}$$

with the rotation angle θ between the body frame $\mathcal{B}$ and the reference frame $\mathcal{E}$ about the Euler axis of rotation $\mathbf{a} = (a_\mathrm{x}, a_\mathrm{y}, a_\mathrm{z})^\mathrm{T}$, which is defined relative to $\mathcal{B}$. In other words, $\mathbf{a}$ denotes the axis about which the body frame $\mathcal{B}$ has been displaced by the angle θ with respect to the reference frame $\mathcal{E}$, according to Fig. A.1 in the Appendix A. This notation simplifies the attitude description considerably. In contrast, the traditional Euler angle notation, for example, requires 3 angles (e.g. roll, pitch and yaw), which are defined w.r.t. different body axes.

Using the above definitions, the governing kinematic equation of the rotational motion of a rigid body can be written as

$$\dot{\bar{q}} = \frac{1}{2}\,\bar{q} \otimes \bar{\omega} \tag{4.16}$$

representing the rate of change of $\bar{q}$ due to the spacecraft's angular velocity $\bar{\omega} = [0, \omega_{\mathrm{x}}, \omega_{\mathrm{y}}, \omega_{\mathrm{z}}]^{\mathrm{T}}$, written in quaternion notation. In the previous equation, the operator $\otimes$ represents the quaternion product [103], which is described in the Appendix A.

Euler's equation, constituting the kinetic equation of the rotational motion [101], describes the rate of change of the angular velocity $\dot{\omega}$ due to an external torque $\mathbf{T} = (T_{\mathrm{x}}, T_{\mathrm{y}}, T_{\mathrm{z}})^{\mathrm{T}}$ about the body axes as

$$\dot{\boldsymbol{\omega}} = [I]^{-1}(\mathbf{T} - \boldsymbol{\omega} \times [I]\boldsymbol{\omega}) \tag{4.17}$$

with $[I]$ the mass moment of inertia tensor.

Alternatively, the kinetic equation can also be formulated with respect to the second derivative of the attitude quaternion [102], which results in

$$\ddot{\bar{q}} = \dot{\bar{q}} \otimes \bar{q}^{-1} \otimes \dot{\bar{q}} + \frac{1}{2}\,\bar{q} \otimes \dot{\bar{\omega}} \quad \text{with } \dot{\bar{\omega}} = \begin{pmatrix} 0 \\ [I]^{-1}(\mathbf{T} - \boldsymbol{\omega} \times [I]\boldsymbol{\omega}) \end{pmatrix} \tag{4.18}$$

Equation (4.18) represents a second order DES and can be formulated as an initial value problem (IVP)

$$\ddot{\bar{q}} = \mathrm{f}\big(\dot{\bar{q}}, \bar{q}, \dot{\bar{\omega}}, t\big), \quad \bar{q}(t = t_0) = \bar{q}_0, \quad \dot{\bar{q}}(t = t_0) = \dot{\bar{q}}_0, \quad \dot{\bar{\omega}}(t = t_0) = \dot{\bar{\omega}}_0 \tag{4.19}$$

with arbitrary initial attitude $\bar{q}_0$, attitude rate of change $\dot{\bar{q}}_0$ and angular rate $\dot{\bar{\omega}}_0$ at time t_0. In the following, the system is solved using a Runge-Kutta Nyström (RKN) integration scheme [105].

In order to demonstrate the optical control concept proposed, a basic rest-to-rest manoeuvre is considered. In principle, a constant optical torque is applied to steer the reflector spacecraft from its initial to final attitude. Halfway during the manoeuvre, when the spacecraft attitude has changed over an angle $\theta/2$, the sign of the torque is inverted to decelerate the motion until the final attitude is reached (bang-bang control). Since the SRP torque magnitude depends on the current attitude of the membrane with respect to the Sun (cone angle α), the position and shape of the boundary line has to be controlled during the manoeuvre. Therefore, after selecting the required torque components $(T_\mathrm{x}, T_\mathrm{y})_\mathrm{req}$ to perform the manoeuvre, the corresponding boundary line coefficients as a function of the current reflector attitude must be found. This can be achieved through the formulation of an inverse problem, as will be shown below.

4.2.2 Inverse problem approach for boundary line control

When re-writing the torque equations, Eqs. (4.12) and (4.13) for the coefficients a and b, the boundary line can be expressed as a function of the (required) torques and the current cone angle α. Given here for torque Case 1 (and the 'upper case' activation state) only, the inverse problem results in

Case 1 $a \geq 0 \ \wedge \ L/2(a-1) \leq b \leq L/2(1-a)$

$$a = -12 \frac{T_\mathrm{y,upper}}{p_0 L^3 \cos^2\alpha} \tag{4.20a}$$

$$b = \pm\frac{L}{2}\sqrt{1 + \frac{8T_\mathrm{x,upper}}{p_0 L^3 \cos^2\alpha} - \frac{48 T^2_\mathrm{y,upper}}{(p_0 L^3)^2 \cos^4\alpha}} \tag{4.20b}$$

where the following conditions apply for the two torque components

$$-\frac{1}{12} p_0 L^3 \cos^2\alpha \leq T_\mathrm{y,upper} \leq 0 \tag{4.21a}$$

$$-\frac{1}{8}\left(L^3\cos^2\alpha - \frac{48\, T^2_\mathrm{y,upper}}{p_0 L^3 \cos^2\alpha}\right) \leq T_\mathrm{x,upper} \leq 3T_\mathrm{y,upper} + \frac{24\, T^2_\mathrm{y,upper}}{p_0 L^3 \cos^2\alpha} \tag{4.21b}$$

The above scheme can be applied as follows. First, the required torques for a particular manoeuvre are selected, which have to satisfy the maximum achievable limits for a given reflector configuration, as well as the conditions of Eqs. (4.21). Second, the shape and position of the boundary line, in terms of the coefficients a and b, in order to create these torques can be computed according to Eqs. (4.20).

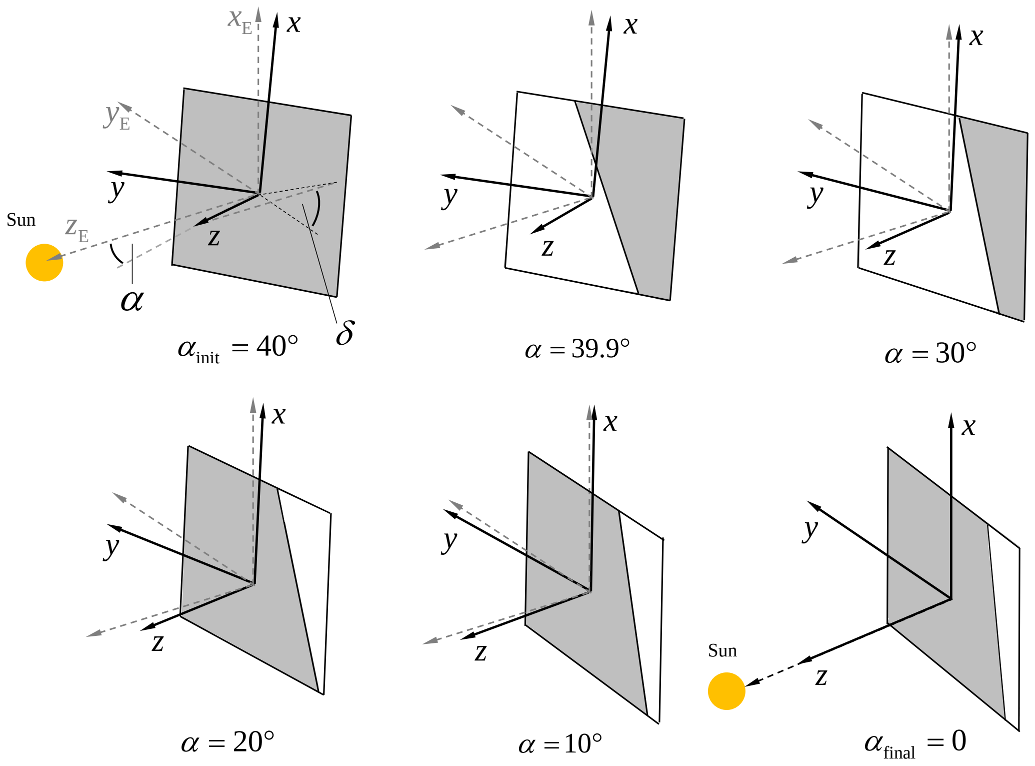

Figure 4.10: Manoeuvre sequence for selected initial reflector attitude $\alpha_0 = 40$ deg and clock angle $\delta_0 = 52$ deg towards final Sun-pointing attitude, and active surface reflectivity region.

4.2.3 Sample Attitude Manoeuvre

The previously described attitude control concept of employing constrained reflectivity regions across the membrane is now applied to perform a basic spacecraft manoeuvre. Considering the sample reflector configuration (edge length $L = 100\,\mathrm{m}$, total mass $m = 200\,\mathrm{kg}$) in a Sun-centred orbit. As introduced before, the spacecraft shall be steered from an arbitrary initial attitude towards Sun-pointing, using combined torques T_x and T_y in the reflector plane.

Initially, the reflector is chosen to be tilted over a cone angle $\alpha_0 = 40$ deg and clock angle $\delta_0 = 52$ deg, as shown in Fig. 4.10 (upper left). This translates into a rotation angle $\theta_x = 38$ deg and $\theta_y = 12$ deg about the in-plane spacecraft axes. After the manoeuvre, the reflector shall be Sun-pointing, thus $\alpha_\mathrm{final} = 0$. From the quaternion approach, the Euler axis follows as $\mathbf{a} = (-0.3, -0.1, 0)$. This axis can be obtained from the initial attitude quaternion $\bar{q}_0$ that is calculated from the initial displacement angles θ_x and θ_y. Accordingly, a constant torque couple of $T_\mathrm{x} = -0.3$ Nm and $T_\mathrm{y} = -0.1$ Nm

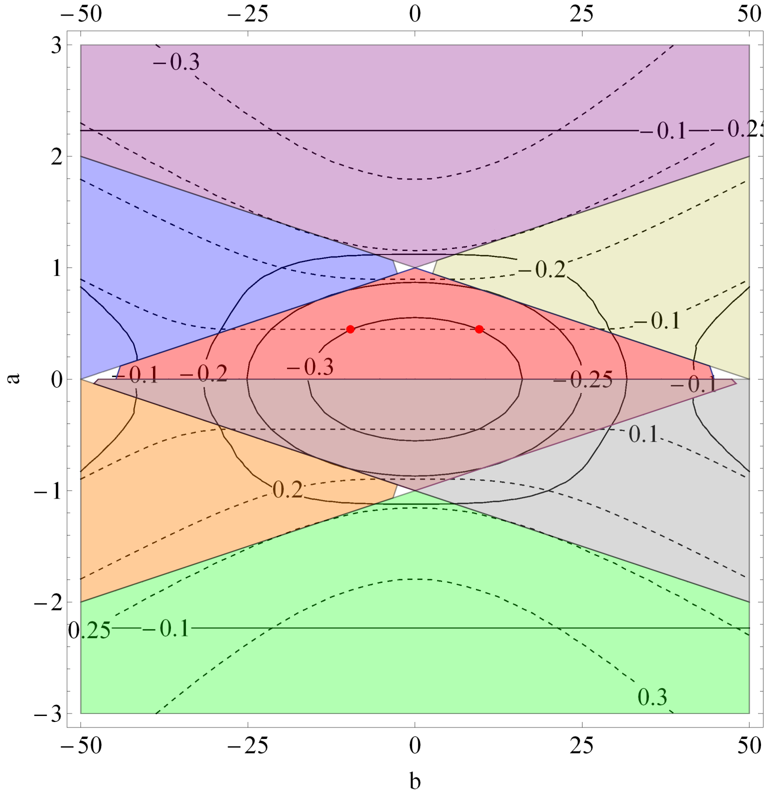

Figure 4.11: In-plane torques $\mathbf{T_x}$ (solid lines) and $\mathbf{T_y}$ (dashed lines) as function of boundary line coefficients a and b and surface cone angle $\boldsymbol{\alpha = 40}$ deg. Red dots indicate feasible sets $\mathbf{(a_0, b_0) = (0.45, \pm 9.59)}$ for the required manoeuvre torques.

is selected such that the total torque vector matches the initial displacement of the reflector with respect to frame $\mathcal{E}$. Since the torque T_x is negative, the 'upper case' distribution needs to be used, as was shown in Fig. 4.9.

For the selected initial cone angle, the achievable torques over the (a, b)-domain of the boundary line are shown in Fig. 4.11, for an active 'upper case' reflectivity distribution. The solid lines again indicate T_x, while the dashed lines represent T_y. Red points identify the two feasible sets $(a_0, b_0) = (0.45, \pm 9.59)$ for the selected torques, as calculated from the inverse problem in Section 4.2.2. They both require the same slope of the boundary line, however, a positive or negative offset in the y-direction can be chosen. Furthermore, from Eq. (4.20) of the inverse problem, the boundary line coefficients are fully determined as a function of the local cone angle during the manoeuvre, as shown in Fig. 4.12. When adapting the reflective region across the surface during the manoeuvre, according to the derived control scheme for the boundary line, the in-plane torques can be kept constant, although the light incidence angle α, and thus the SRP forces across the membrane, change over time. The reflector attitude is computed

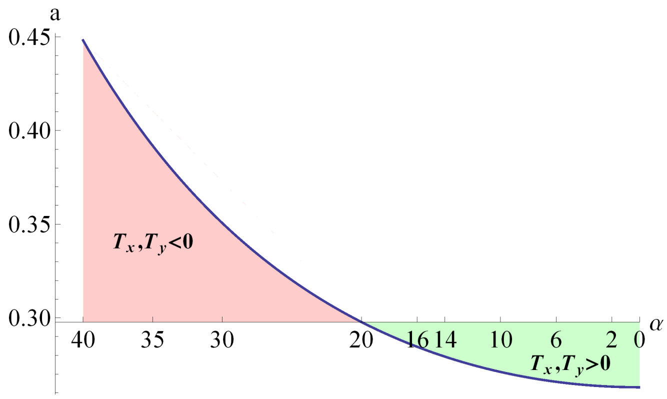

(a) slope coefficient

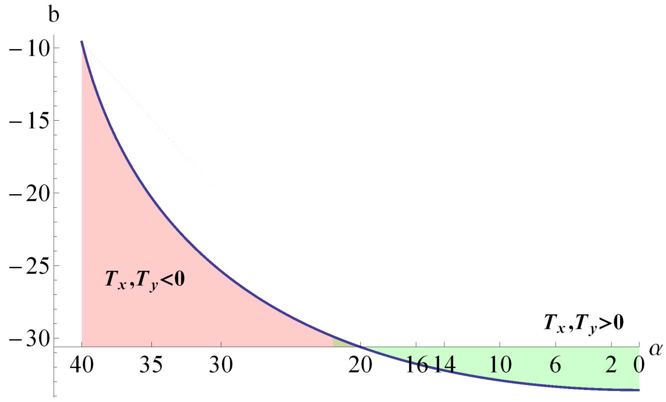

(b) offset coefficient

Figure 4.12: Controlled boundary line coefficients a and b as function of surface cone angle α for selected manoeuvre towards Sun-pointing attitude.

through the DES of rotational motion, Eq. (4.18), by solving the IVP, as described in Subsection 4.2.1. The resulting time history of the cone angle and angular rates ω_{x} and ω_{y} of the spacecraft about the in-plane axes are shown in Fig. 4.13, together with the applied bang-bang torque profile. The total manoeuvre time to rotate the surface into a Sun-pointing attitude is $1216\,\mathrm{s} \approx 20$ min.

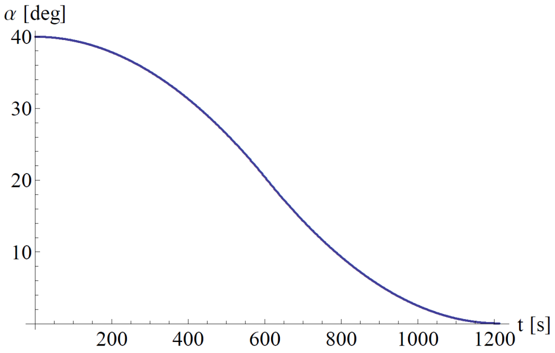

(a) cone angle α

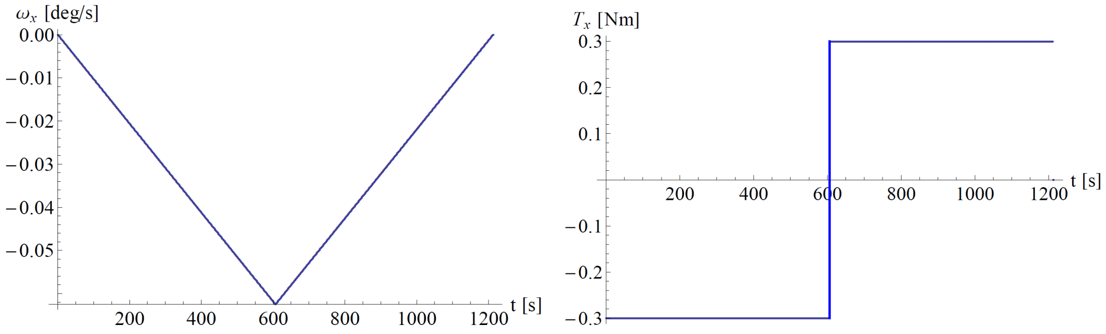

(b) angular rate in x-direction

(c) torque in x-direction

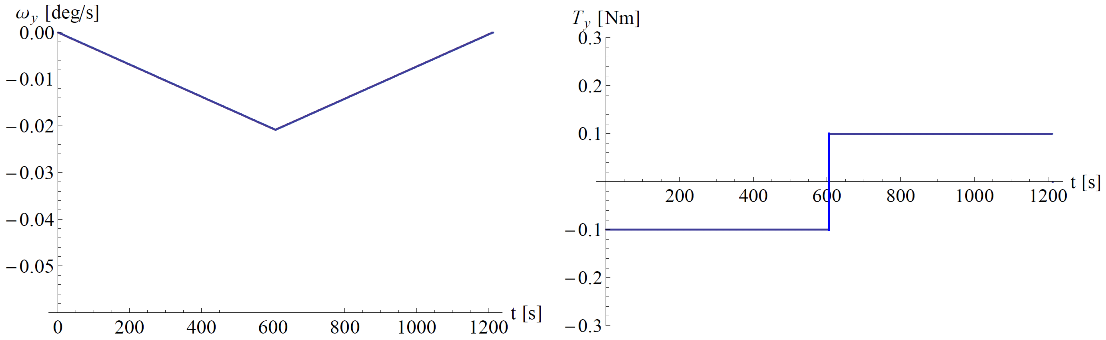

(d) angular rate in y-direction

(e) torque in y-direction

Figure 4.13: Spacecraft manoeuvre time-history towards final Sun-pointing attitude.

4.3 Discrete reflectivity array

In this section, the constrained reflectivity regions are replaced by a number of discrete electro-chromic coating elements, or ‘RCDs’, as introduced in Section 2.4. The square RCDs are assumed to be uniformly distributed across the entire membrane surface, as in a dot matrix. Each cell can maintain two states, either ’on’ (high reflectivity) or ’off’ (low reflectivity). Consequently, the achievable control torques are expected to be discrete as well, while being a function of number, position and activation state of the

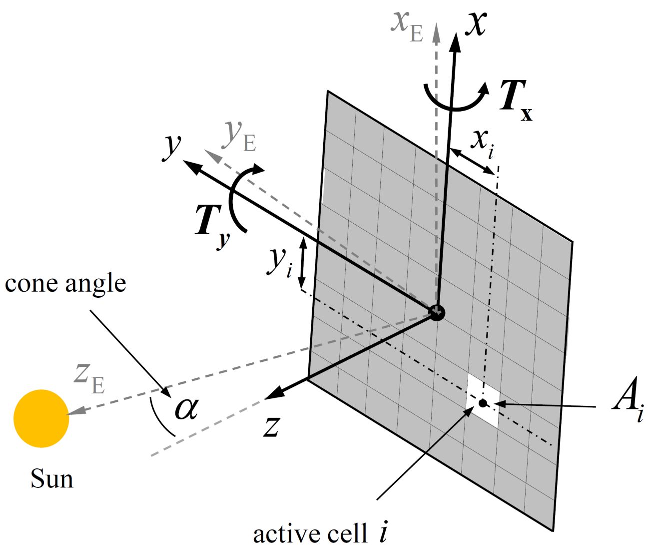

Figure 4.14: Square membrane reflector spacecraft with discrete number of RCD cells across the surface to modulate SRP torques acting on the structure for attitude control.

coating elements. With this concept a wide range of torque vector directions in the reflector plane can be generated, while torques normal to the surface are again zero.

In order to steer the spacecraft using this discrete RCD matrix (or RCD array, respectively), an attitude control framework can be formulated using, for example, a quaternion feedback controller. This framework shall compute the required reference torques (e.g. for a particular manoeuvre) that have to be matched by the actuating RCD matrix. The aim is towards finding the optimal reflectivity pattern in terms of the number and combination of active cells to create the required control torque. This 'optical attitude controller' has to take into account that control torques can be delivered with two (in-plane) components only for controlling three rotational degrees of freedom. Furthermore, the two in-plane torque components both depend on the distribution and activation state of the RCD elements simultaneously; thus, they cannot be controlled independently. In addition, the torque magnitudes vary with changing spacecraft attitude (surface cone angle α), as seen previously in Section 4.2, which constitutes a challenging attitude control problem.

4.3.1 Membrane Surface Model using RCD matrix

As shown in Fig. 4.14, the membrane surface A is assumed to be covered with a square matrix $[M]:=(n,n)$ of electro-chromic coating cells, with n the number of cells per side, that are restricted to operate at two discrete reflectivity states, either 'on' ($\rho_{\text{on}} = 1$)

or 'off' ($\rho_{\text{off}} = 0$). The additional mass and thickness of the elements is neglected, while the membrane is assumed ideally flat and rigid. Each cell i of area $A_i = \Delta x\, \Delta y$ and distance x_i and y_i from the in-plane x and y-axes, respectively, creates a discrete torque $\mathbf{T}_i = (T_{\text{x},i}, T_{\text{y},i})$. Written in x and y-components, the SRP torques created by each individual element i at 1 AU solar distance are

$$T_{\text{x},i} = -p_0\,[1+\rho]\cos^2\alpha\, y_i\, A_i \tag{4.22a}$$

$$T_{\text{y},i} = \quad p_0\,[1+\rho]\cos^2\alpha\, x_i A_i \tag{4.22b}$$

with $\rho \in (\rho_{\text{on}}, \rho_{\text{off}})$. The total torque $\mathbf{T} = (T_{\text{x}}, T_{\text{y}})$ is simply the sum of all RCD cells across the surface

$$T_{\text{x}} = \sum_{i=1}^{N} T_{\text{x},i} \quad \text{and} \quad T_{\text{y}} = \sum_{i=1}^{N} T_{\text{y},i} \tag{4.23}$$

with N the total number of cells. The number of possible reflectivity combinations C_{n} using two-state elements (on/off) follows the relation

$$C_{\text{n}} = 2^{n^2} \tag{4.24}$$

and thus, increases rapidly with increasing size of the square RCD matrix $[M]$, as shown in Table 4.1. For example, using a (6×6)-matrix, and thus a total number of $N = 36$ elements across the surface, the number of possible combinations is already $C_6 = 68.7$ billion. In order to compute the large number of reflectivity combinations expected, the properties of the discrete torque sets, created by C_{n}, need to be examined. If, for example, potential recurring patterns within the torque sets can be identified, this would allow for a truncation of the number of total combinations to the number of combinations that create unique torques. Furthermore, as shown for a (3×3)-array in Fig. 4.15, every (axially) symmetric combination does not create a torque, since SRP

Table 4.1: Number of possible discrete reflectivity combinations C_{n} as a function of the square matrix size $[M] = (n, n)$ and total element number $N = n^2$

n	N	C_{n}
2	4	16
3	9	512
4	16	65,536
5	25	33.554×10^6
6	36	68.719×10^9

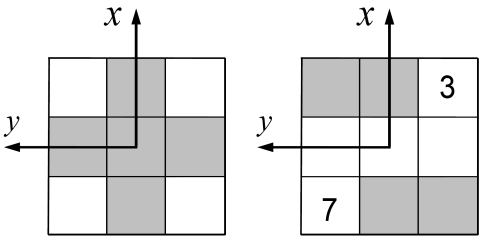

Figure 4.15: (3 × 3)-size RCD matrix with two axis-symmetric reflectivity combinations, creating zero torque about both in-plane axes.

torques created by opposite RCD elements cancel out. For example, the two active cells labelled '3' and '7' create the same torques about both in-plane axes, but with opposite signs. As a result, if only these two cells are active (or inactive), the total torque is zero. Furthermore, each inverted combination of the binary-state matrix $[M]$ generates the exact counter torque about both in-plane axes, as can be seen in Fig. 4.16. According to the figure, the four upper-left cells are active on the left-hand side, while the remaining five cells are inactive. In the right-hand figure, the inverted combination is shown. The total torque vector, highlighted in red, has the same magnitude, but opposite sign. This property is again shown in Fig. 4.17. The figure shows one subset of the total of $C_3 = 512$ combinations, in which each combination creates the same torques about the x and y-axis. Only the sign of the two torques changes, as indicated by the (+) and (−) sign at the top of each column. For example, the two sets of frame axes (solid and dashed, respectively) mark two inverted combinations, one from the (++) column, one from the (−−) column. As can be seen, middle elements that contain one of the axes only produce a torque about the other axis. The centre-element never produces a torque. Therefore, the total number of discrete torques that can be generated is much smaller than C_n.

In total, four truncation laws can be formulated to find the number of same-torque reflectivity combinations for a given set C_n

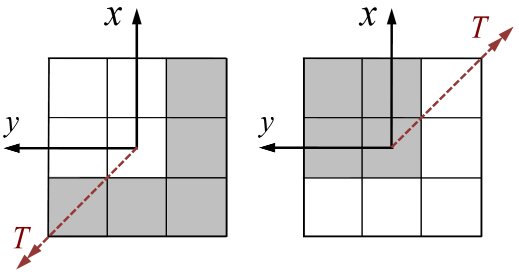

Figure 4.16: (3 × 3)-size RCD matrix with two inverse reflectivity combinations, creating opposite torque of same magnitude (red arrow).

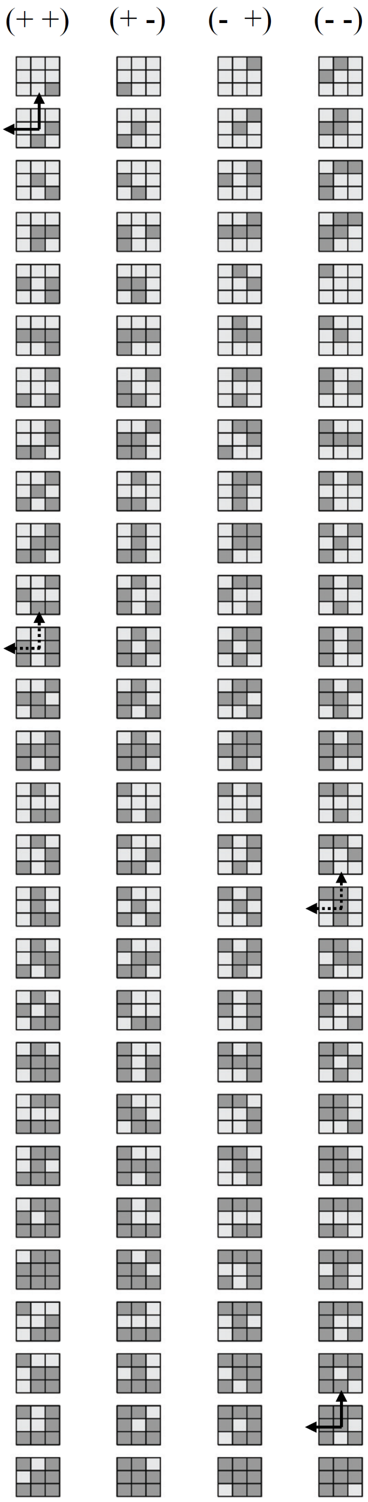

Figure 4.17: Largest subset (112 combinations) of possible reflectivity combinations ($C_3 = 512$) using a (3×3)-array. Each combination generates the same torque about the x and y-axes. Signs of T_x and T_y are different in each column, as indicated with + (positive) and - (negative)

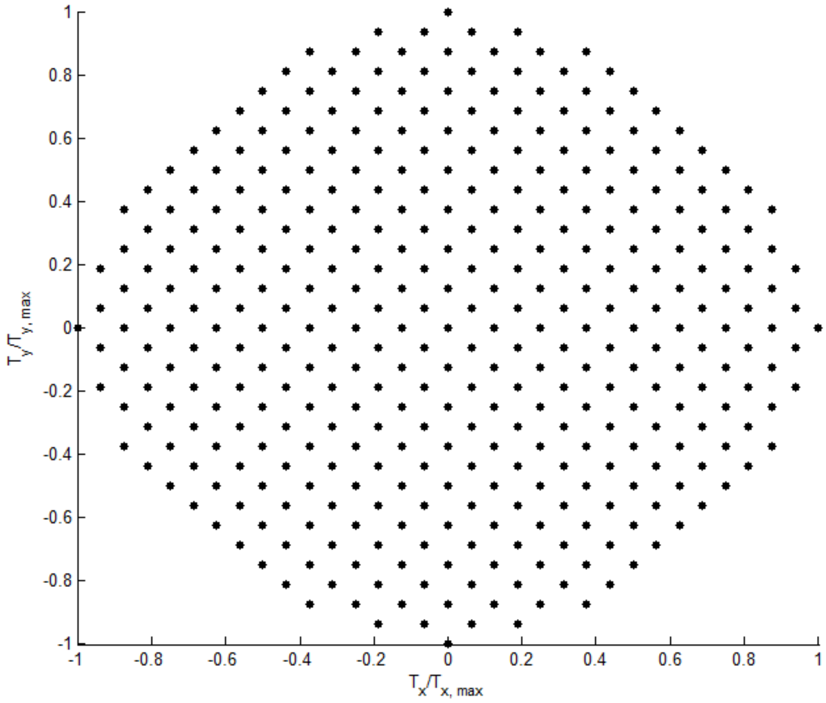

Figure 4.18: Non-dimensional discrete torques in x and y-direction, generated by a (4×4)-array. Each entry may contain several reflectivity combinations that result in the same torque.

1. axis-symmetric combinations do not create a torque (opposite elements cancel out)
2. middle elements along one of the axes only produce a torque about the other axis
3. the centre element never produces a torque
4. each inverted combination generates a counter torque of same magnitude (sign inversion)

Finally, a large number of reflectivity combinations create the same torques about the x and y-axis. For example, the total number of combinations for a (4×4)-array is $C_4 = 65,536$. Removing the same-torque combinations reduces this number to $376+1$ unique torque combinations (including zero-torque combinations). This is a reduction of 99.4 %.

The remaining discrete torque pairs for the (4×4)-array are shown in Fig. 4.18, normalised by the maximum possible torque about each in-plane axis, $T_{\mathrm{x,max}}$ and $T_{\mathrm{y,max}}$. The distance between two torque pairs in the x and y-directions represents the minimum discrete torque increment that can be generated using a (4×4)-array. This is also demonstrated by Fig. 4.19, which provides the total torque magnitude $T = (T_{\mathrm{x}}^2 + T_{\mathrm{y}}^2)^{1/2}$

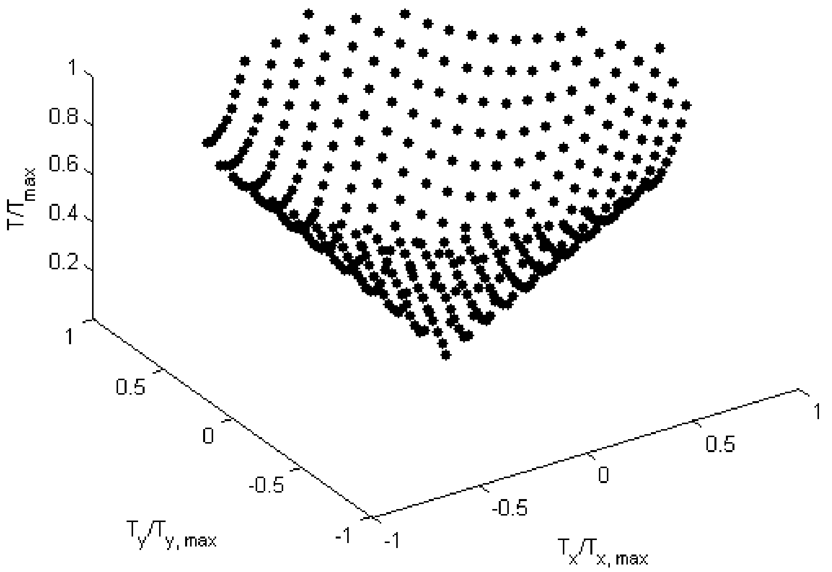

Figure 4.19: Non-dimensional discrete torques in x and y-direction, generated by a (4×4)-array, and total magnitude of the torque.

that can be generated by each reflectivity combination. This already indicates potential challenges for membrane attitude control, in case a limited number of RCD elements across the surface are used.

4.3.2 Optical Attitude Control using RCD matrix

In the following, a feedback control scheme for two-axis attitude control of the membrane reflector using a discrete $(n \times n)$ actuation matrix is introduced. The rigid-body attitude dynamics of the spacecraft are described using Euler's Equation in quaternion notation, as introduced in Subsection 4.2.1. The two equations of rotational motion, Eqs. (4.16) and (4.17), can be solved numerically by formulating the IVP

$$\bar{q}(0) = \bar{q}_0, \quad \boldsymbol{\omega}(0) = \boldsymbol{\omega}_0 \tag{4.25}$$

and using, for example, the MATLAB$^{\text{TM}}$ *ode45* routine that employs an explicit Runge-Kutta $(4, 5)$ scheme [106].

The spacecraft attitude is controlled using a quaternion feedback scheme in Simulink$^{\text{TM}}$, as shown schematically in Fig. 4.20. First, the scheme calculates the error quaternion $\bar{q}_{\text{err}}$, between the desired final attitude $\bar{q}_{\text{final}}$ and the current attitude $\bar{q}$, which is known from the DES of rotational motion. The DES is represented by the function block termed 'attitude dynamics' in Fig. 4.20. The error quaternion $\bar{q}_{\text{err}}$ is calculated through

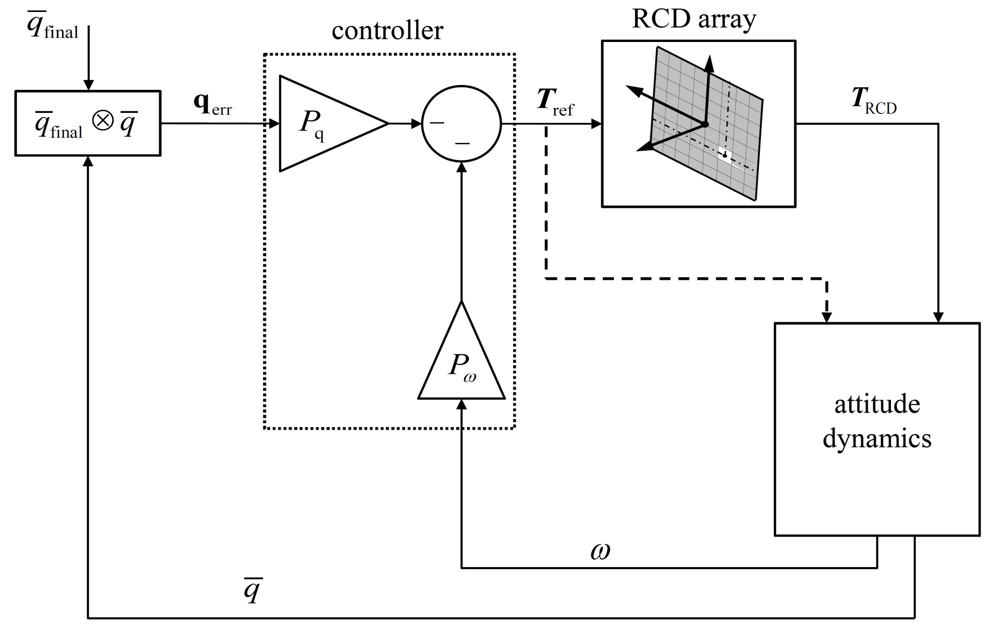

Figure 4.20: Quaternion feedback control scheme. Dashed line indicating reference torque $\mathbf{T}_{\text{ref}}$ loop without RCD actuation $\mathbf{T}_{\text{act}}$.

the quaternion product

$$\bar{q}_{\text{err}} = \bar{q}_{\text{final}} \otimes \bar{q} \tag{4.26}$$

according to Eq. A.13 in the Appendix A. Second, $\bar{q}_{\text{err}}$ is fed into the 'controller', which will be described below, together with the current angular velocity vector $\boldsymbol{\omega}$. Third, the controller calculates the reference torque $\mathbf{T}_{\text{ref}} = (T_{\text{x}}, T_{\text{y}})_{\text{ref}}$ that is required to minimise the error quaternion, and thus, the angular displacement of the spacecraft from its final attitude $\bar{q}_{\text{final}}$. Finally, $\mathbf{T}_{\text{ref}}$ can either be used directly to control the spacecraft attitude, as indicated by the dashed line in Fig. 4.20, connecting the 'controller' with the 'attitude dynamics' block. Alternatively, $\mathbf{T}_{\text{ref}}$ can be fed into the optical RCD array that can be configured in terms of the number of elements $(n \times n)$. The RCD array returns a discrete optical torque $\mathbf{T}_{\text{RCD}}$ from $\mathbf{T}_{\text{ref}}$ in order to steer the spacecraft, as will be described below.

According to Fig. 4.20, a PD-controller is employed, consisting of two loops: first, an inner loop using a proportional controller P_{ω} for the angular velocity. Second, an outer loop employing a proportional controller P_{q} for the tracking of the current attitude error. The combined controller can be formulated as [107]

$$\mathbf{T}_{\text{ref}} = -P_{\text{q}} \cdot \mathbf{q}_{\text{err}} - P_{\omega} \cdot \boldsymbol{\omega} = \begin{pmatrix} T_{\text{x,ref}} \\ T_{\text{y,ref}} \\ 0 \end{pmatrix} \tag{4.27}$$

with $\mathbf{q}_{\mathrm{err}}$ the vector component of the current error quaternion, according to Eq. (4.15). The $T_{\mathrm{z,ref}}$ component is to be neglected, since no torque normal to the membrane plane can be provided by the employed RCD array. The values of the gains P_ω and P_{q} are defined empirically such that the maximum output torque $\mathbf{T}_{\mathrm{ref}}$ matches the maximum discrete torque $\mathbf{T}_{\mathrm{RCD}}$ that can be achieved by the employed RCD array and for a given reflector spacecraft configuration. The maximum torque is generated when one half of the employed RCD cells is active ($\rho = 1$), while $\rho = 0$ for the other half.

Before the control loop is executed, the chosen $(n \times n)$ RCD array is initialised by calculating all possible discrete torques $(T_{\mathrm{x}}, T_{\mathrm{y}})_{\mathrm{RCD}}$ for all reflectivity combinations, truncated using the previous laws in Subsection 4.3.1. The remaining torques are stored in a lookup table, together with the respective combination number of the active element(s). For example, the set of possible torques using a (4×4) element array has been shown in Fig. 4.18.

When the control loop is active, the controller returns the reference torque $\mathbf{T}_{\mathrm{ref}}$, according to Eq. (4.27), which is then provided to the optical RCD array. In here, the achievable torque from the employed $(n{\times}n)$ RCD-array is computed by browsing the lookup table of discrete RCD torques. In particular, the optimal torque $\mathbf{T}^*_{\mathrm{RCD}} = (T_{\mathrm{x}}, T_{\mathrm{y}})^*_{\mathrm{RCD}}$ is found by scanning the lookup table for the closest match torque about the $\mathbf{x}$ and $\mathbf{y}$-axes. As noted before, the array can only generate a finite number of torques, with the torque magnitude further depending on the current surface cone angle α towards the Sun, according to Eq. (4.2). Finally, the found $\mathbf{T}^*_{\mathrm{RCD}}$ is used within the 'attitude dynamics' block to compute the new attitude, according to Eqs. 4.16 and 4.17.

4.3.3 Attitude Manoeuvre using discrete RCD array

The optical RCD array is now applied to control the attitude of a membrane reflector spacecraft on a Sun-centered orbit. Starting from an arbitrary initial attitude and angular rate, the final spacecraft attitude shall be Sun-pointing. The final attitude about the $\mathbf{z}$-axis is not controllable and will be neglected throughout the present analysis. This can be justified by the fact that the reflector attitude about the $\mathbf{z}$-axis has no impact on the SRP torque magnitudes.

The same square reflector configuration with edge length $L = 100$ m and total mass $m = 200\,\mathrm{kg}$, see Section 4.2, is used for demonstration. The optical controller shall perform a basic manoeuvre to obtain a Sun-pointing attitude, thus with cone angle $\alpha_{\mathrm{final}} = 0$. Initially, the membrane surface is chosen to be tilted by the Euler angles $\theta_{\mathrm{x},0} = \theta_{\mathrm{y},0} = -40\,\mathrm{deg}$ about the in-plane x and y-axis. This attitude translates into an

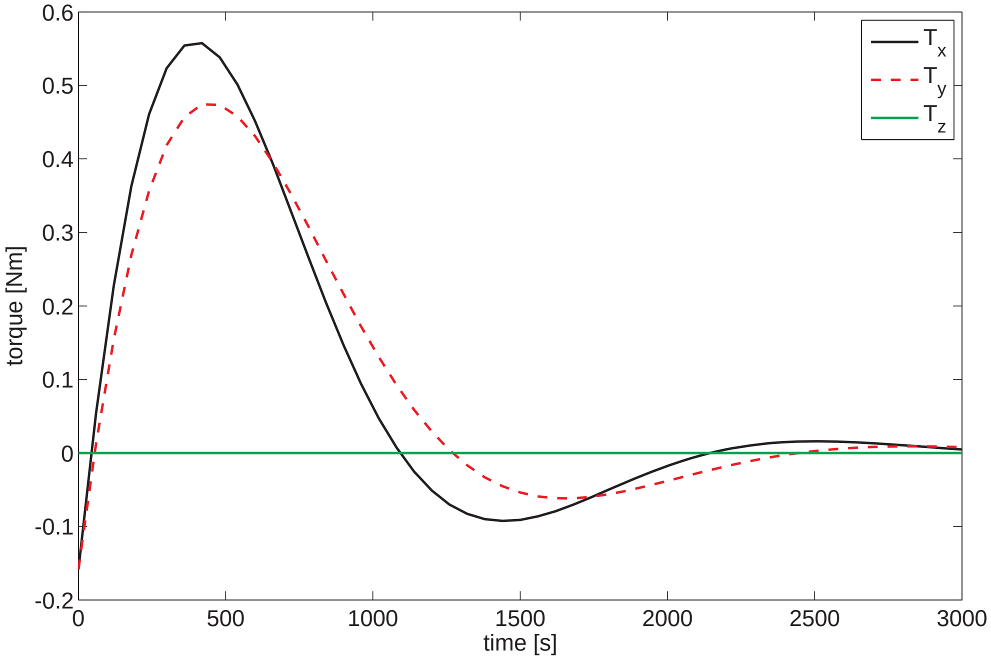

Figure 4.21: Reference torque $\mathbf{T}_{\mathrm{ref}}$ from quaternion feedback controller.

initial cone angle of $\alpha_0 = 54$ deg. Additionally, the spacecraft is rotating with an initial angular rate of $\omega_{\mathrm{x},0} = \omega_{\mathrm{y},0} = 0.1\,\mathrm{deg/s}$. First, the manoeuvre is controlled using the reference torques $\mathbf{T}_{\mathrm{ref}}$ from the ideal feedback controller, without RCD actuation, as shown by the dashed path in Fig. 4.20. Second, a (4×4) RCD-array is used to translate the reference torques into the closest-match optical SRP torques $\mathbf{T}^{*}_{\mathrm{RCD}}$.

The second control setup, using the discrete RCD torques to steer the spacecraft, is further repeated to include the effect of the current surface cone angle α on the SRP torques during the manoeuvre. The SRP variation with changing α can be switched off in the feedback scheme and results are given for comparison.

The resulting reference torque components $(T_{\mathrm{x}}, T_{\mathrm{y}})_{\mathrm{ref}}$ for the chosen attitude manoeuvre, as computed by the controller, are shown in Fig. 4.21. The simulation is finished at the time t_{final} for which $\alpha(t)$ stays below a certain threshold $\alpha_{\mathrm{lim}} \leq 0.1\,\mathrm{deg}$. This is achieved at time $t_{\mathrm{final}} = 3000\,\mathrm{s} = 50\,\mathrm{min}$. The simulation is repeated after activation of the (4×4) RCD array. The achievable discrete torques from the RCD array are given in Fig. 4.22, which shows that the RCD array can follow the controller's demands by returning the closest matching torques available. Please note that in the figure, a constant cone angle $\alpha = 0$ is assumed to highlight the discrete character of the torques. When including the cone angle influence on the SRP during the manoeuvre, as shown in Fig. 4.23, the actuated torques $(T_{\mathrm{x}}, T_{\mathrm{y}})_{\mathrm{RCD}}$ are modulated towards lower values, in particular for high $\alpha(t)$. According to Fig. 4.24, the cone angle is highest

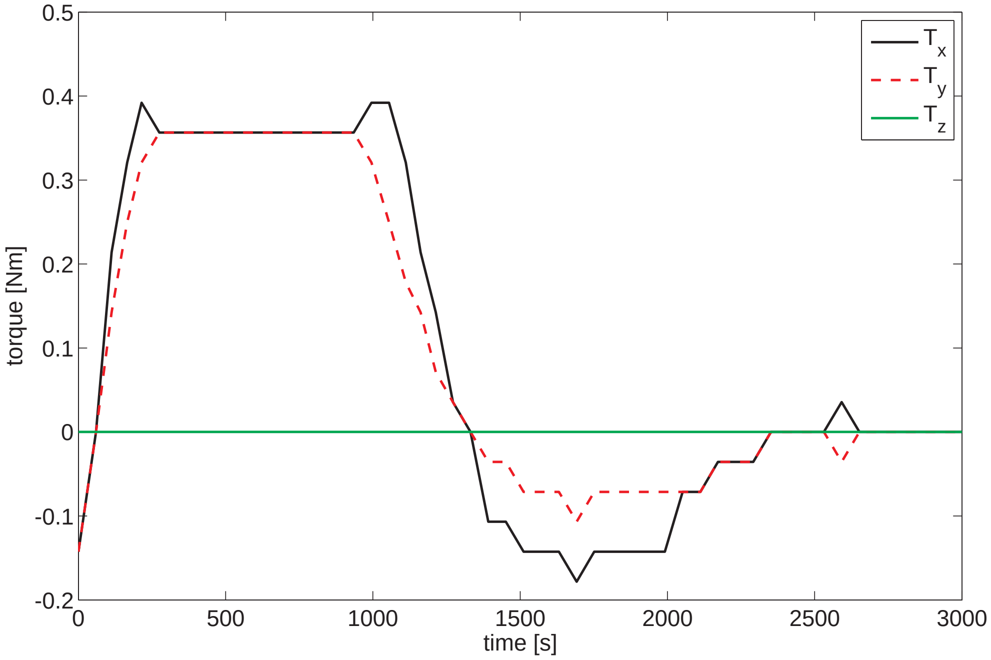

Figure 4.22: Achievable torque $\mathbf{T_{RCD}}$ from RCD array, assuming constant cone angle $\alpha = 0$ during the manoeuvre.

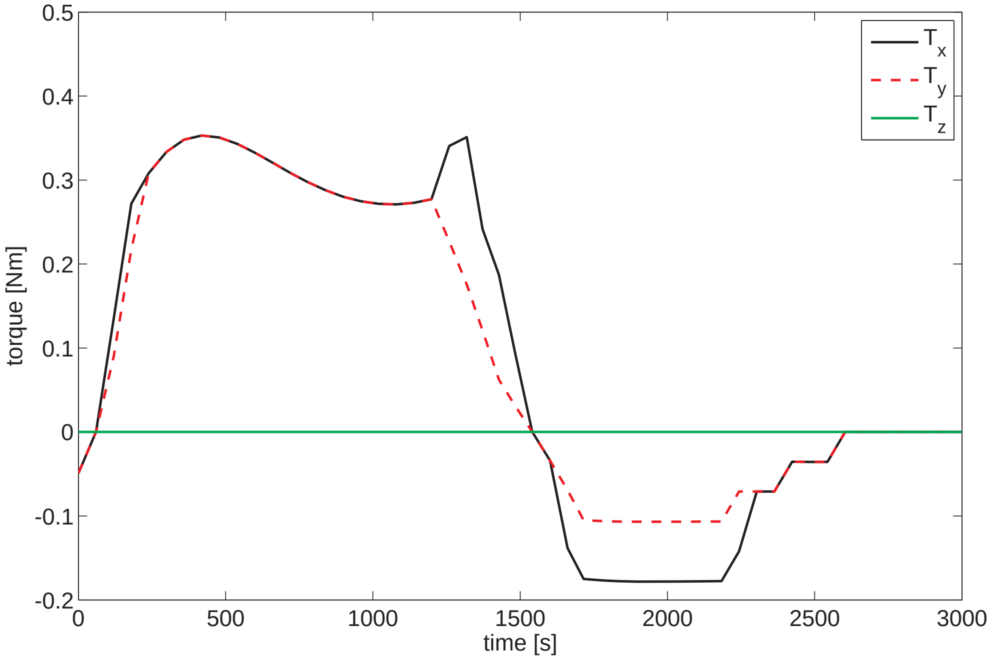

Figure 4.23: Achievable torque $\mathbf{T_{RCD}}$ from RCD array and considering variation of SRP with changing surface cone angle α over time.

at the start of the simulation and during the time interval $[700, 1500]$ sec, when the membrane overshoots the targeted Sun-pointing attitude. The overshooting is higher

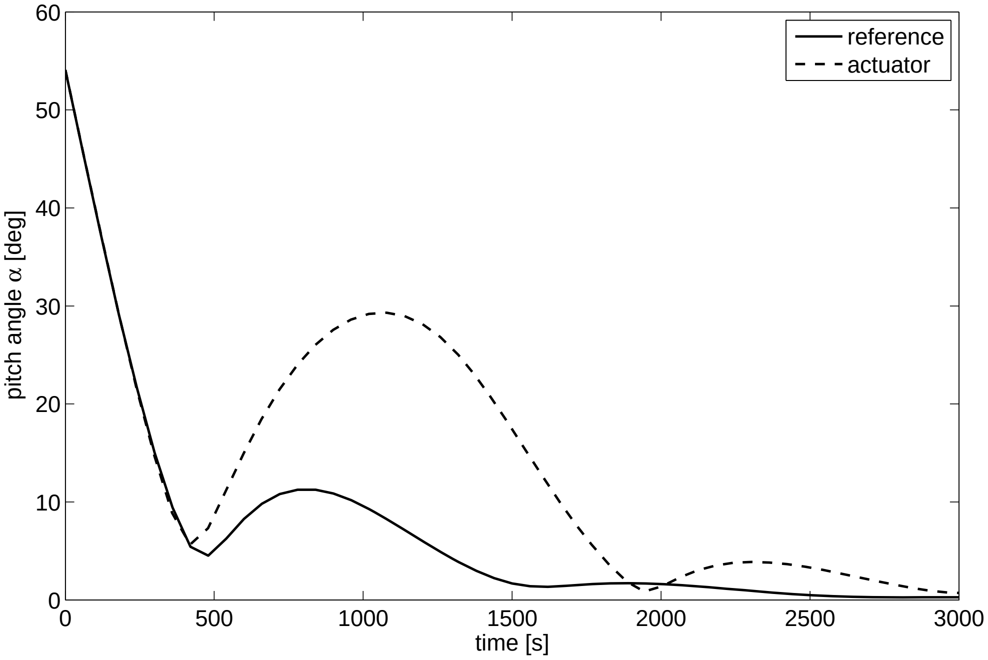

Figure 4.24: Membrane surface pitch angle α time-history using reference torque control (solid line) and using RCD array control, considering SRP variation with α (dashed line)

in case of the RCD actuation (dashed line in Fig. 4.24), due to the limited capacity of the RCD-array to provide the required control torques. The cone angle reaches the required α_{lim} condition in approximately twice the simulation time (not shown in Fig. 4.24), which is likely to be due to the minimum threshold of discrete torque that can be generated by the employed RCD-array.

4.4 Chapter summary

A variable reflectivity distribution across the surface of a square membrane reflector has been considered in this chapter, in order to investigate ultra-lightweight optical steering of large gossamer spacecraft. The nominal SRP forces across the membrane have been modulated using different surface reflectivity models, which generate optical torques about the in-plane spacecraft axes.

First, a continuous reflectivity model across the surface of the membrane has been employed to control the attitude of the spacecraft in LEO and under the influence of gravity-gradient torques. While the spacecraft has been restricted to planar motion in a fixed orbital plane, it has been shown that a constant Sun-pointing attitude can be maintained, when modulating the coefficients of a linear reflectivity function across the membrane.

Second, a more complex model using constrained regions of high reflectivity across the surface has been employed to enable two-axis attitude control of the membrane spacecraft. When controlling the boundary line between two regions of high and low reflectivity, a wide range of torques in the membrane plane can be generated. Since the SRP force magnitude depends on the surface cone angle towards the Sun, an analytic control scheme has been derived that maintains a constant SRP torque even when the surface is rotating during manoeuvre phases. The control scheme moves the boundary line across the surface, depending on the current spacecraft attitude with respect to the Sun. It has been shown that by controlling the SRP torques in the membrane plane, the reflector can be brought to a Sun-pointing attitude from an arbitrary initial displacement.

Finally, a discrete array of RCDs across the membrane surface has been considered. Each cell can maintain two states, either 'on' (high reflectivity) or 'off' (low reflectivity). The resulting discrete torques have been calculated for a given reflector size, and as a function of number, position and activation state of the coating elements. The concept has been demonstrated by a basic Sun-pointing manoeuvre, after the discrete actuation model has been implemented into a quaternion feedback control scheme. Starting from an arbitrary initial attitude and angular rate, a (4,4)-array of reflectivity cells has been employed, which can obtain $65,536$ reflectivity combinations and 376 discrete torques in the membrane plane. The array was able to steer the spacecraft into final resting attitude, despite the limitation on the discrete torques that can be generated by such low number of reflectivity cells. Compared to the reference control torques, the optical-array torques have been in good agreement, although the total manoeuvre time has been twice as long, compared to the reference manoeuvre time. This has been attributed to the minimum threshold of discrete torques that can be generated by the employed array.

Exploiting variable SRP forces across the surface to steer space membrane reflectors introduces a more flexible and potentially lightweight attitude control method to large gossamer spacecraft. Therefore, the concept of optical attitude control may contribute to reduce the overall system mass.

Chapter 5

Shape control of elastic membrane reflectors

The previous two chapters considered optical attitude control of large rigid gossamer structures by exploiting SRP in space. This chapter will now investigate the concept of optical shape control of large elastic gossamer structures to enable ultra-lightweight surface actuation and high shape accuracy for this type of spacecraft. In Section 5.1, the governing equations of a thin circular membrane subject to SRP loads, perpendicular to the undeflected surface plane, will be introduced. The nominal deflection profiles due to uniform SRP across the surface will be assessed first in Section 5.2, for different membrane sizes and distances from the Sun. Subsequently, in Section 5.3, suitable reflectivity functions across the surface will be used to modulate light pressure for controlled surface deflection. To this aim, the required reflectivity distribution to obtain a particular deflection, e.g. a parabolic profile, will be calculated by formulating an inverse problem (Section 5.3.1). The resulting deflection shapes and magnitudes will be evaluated in Section 5.4 in terms of the achievable focal lengths as a function of aperture size and solar distance. Section 5.5 will summarise the chapter.

5.1 Elastic membrane deflection through SRP

As discussed in Chapter 1, deploying a large highly-reflective membrane in space enables a variety of future space-based applications. However, it is essential to keep the system mass as low as possible to reduce launch costs, while at the same time providing controllability, reliability and shape accuracy of the surface in the space environment.

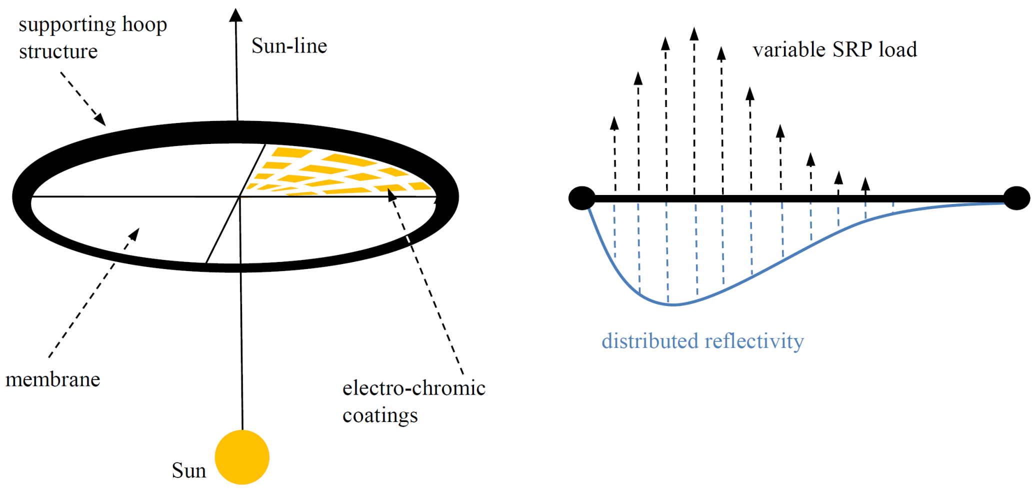

Figure 5.1: Circular membrane reflector with thin-film electro-chromic coatings (left) and modulated surface reflectivity enabling variable SRP loads (right).

To this end, controlling the membrane shape by modulating the SRP forces acting on the structure in space is considered throughout this chapter.

The circular membrane reflector is modelled as a thin circular polymer film, according to Section 1.1.2. The membrane is supported by a circumferential hoop structure, as shown in Fig. 5.1, forming hinged-support type boundary conditions (BC) at the edges. The mass of the hoop is assumed to be much larger than the membrane mass. Thin-film electro-chromic coatings are further assumed to be uniformly distributed across the surface, while neglecting the additional mass and thickness that would be introduced to the membrane. As shown schematically in Fig. 5.1, these coatings are capable of modulating the surface reflectivity in the interval $\rho = [0, 1]$. The SRP loads are calculated using the simplified SRP model, according to Eq. (2.7). The membrane (including electro-chromic coatings) is assumed to be of uniform thickness with uniform mechanical properties in all directions (isotropic). Prior to deflection, the membrane surface is assumed to be flat and perpendicular to the Sun-reflector line, thus the cone angle $\alpha = 0$.

In the present analysis, only the static structural bending of the membrane is accounted for, ignoring any dynamical response (e.g. vibrational modes) of the real structure due to time-dependent loads, movement of the structure or flexibilities in the supporting hoop. A thin circular isotropic membrane of radius R and thickness t under uniform vertical SRP load p_{SRP}, perpendicular to the undeflected membrane plane, is shown in Fig. 5.2. In here, w_0 denotes the out-of-plane deflection at the centre of the membrane. Due to the very small thickness and relatively large deflections w to be expected (i.e. a high $W = w/t$ ratio), the use of non-linear bending theory [108] is required, ac-

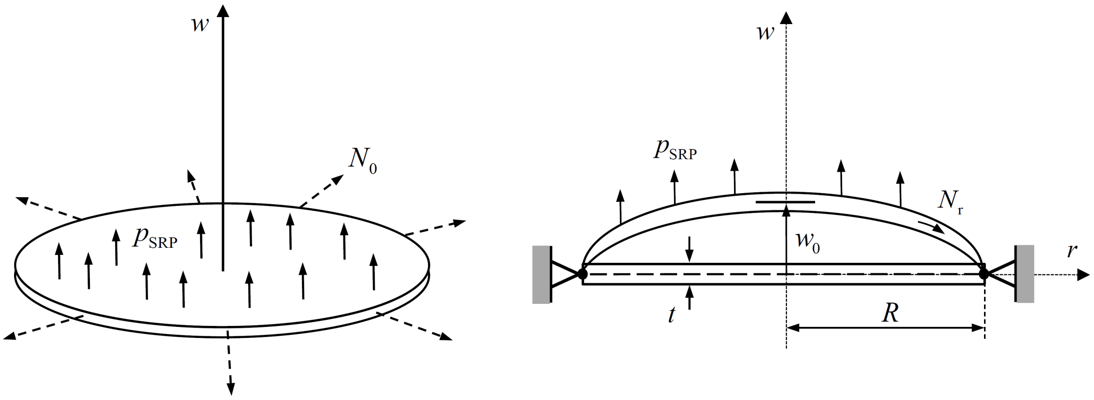

Figure 5.2: Circular membrane under uniform vertical SRP load, perpendicular to the undeflected membrane plane, and initial in-plane tension (left), and membrane cross-section with hinged-edge support and deflected shape (right).

counting for the non-negligible in-plane tension within the material. In general, thin membrane-like structures offer a very small flexural rigidity and therefore cannot resist bending loads [109]. Furthermore, radial and circumferential in-plane tensions are non-negligible, while for low W ratios, they are usually ignored within the well-known linear beam and plate theory [110].

According to [111, 112], the symmetrical out-of-plane deflection can be described by a third-order non-linear coupled system as

$$\frac{\mathrm{d}^3 w}{\mathrm{d}r^3} + \frac{1}{r}\frac{\mathrm{d}^2 w}{\mathrm{d}r^2} - \frac{1}{r^2}\frac{\mathrm{d}w}{\mathrm{d}r} - \frac{N_0}{D}\frac{\mathrm{d}w}{\mathrm{d}r} - \frac{\tilde{N}_{\mathrm{r}}}{D}\frac{\mathrm{d}w}{\mathrm{d}r} = \frac{p_{\mathrm{SRP}}\, r}{2D} \tag{5.1}$$

$$\frac{\mathrm{d}\tilde{N}_{\mathrm{r}}}{\mathrm{d}r} + \frac{\tilde{N}_{\mathrm{r}} - \tilde{N}_\theta}{r} = 0 \tag{5.2}$$

$$\frac{\mathrm{d}\tilde{N}_\theta}{\mathrm{d}r} - \frac{\tilde{N}_{\mathrm{r}} - \tilde{N}_\theta}{r} + \frac{Et}{2r}\left(\frac{\mathrm{d}w}{\mathrm{d}r}\right)^2 = 0 \tag{5.3}$$

with the radial and circumferential in-plane tensions N_r and N_θ and the initial in-plane tension N_0 at the edges, according to Fig. 5.2. By further definition, E is the Young's modulus, ν the Poisson ratio, and D the flexural rigidity (bending stiffness) of the membrane material, which is defined as

$$D = \frac{Et^3}{12(1-\nu^2)} \tag{5.4}$$

Please note that Eqs. 5.1-5.3 originate form the equilibrium equations for the *symmetrical* bending of thin membranes only. The system has been chosen for the present analysis, because it accounts for non-linear load distributions and large deflections.

Since the membrane is initially stretched by the load N_0, the in-plane tensions are decomposed as follows

$$N_\mathrm{r} = N_0 + \tilde{N}_\mathrm{r} \qquad \text{and} \qquad N_\theta = N_0 + \tilde{N}_\theta \tag{5.5}$$

where $\tilde{N}_\mathrm{r}$ and $\tilde{N}_\theta$ are incremental changes from N_0 due to the SRP load.

The system in Eqs. (5.1) to (5.3) can further be written in non-dimensional form as

$$\chi'' + \frac{\chi'}{\xi} - \left(k^2 + \frac{1}{\xi^2}\right)\chi - 12(1-\nu^2)S_\mathrm{r}\chi = 6(1-\nu^2)P_\mathrm{SRP}\xi \tag{5.6}$$

$$S_\mathrm{r}' + \frac{S_\mathrm{r} - S_\theta}{\xi} = 0 \tag{5.7}$$

$$S_\theta' - \frac{S_\mathrm{r} - S_\theta}{\xi} = -\frac{1}{2\xi}\chi^2 \tag{5.8}$$

where the following non-dimensional variables are used

$$\xi = \frac{r}{R}, \quad \square' = \frac{\mathrm{d}}{\mathrm{d}\xi}, \quad W = \frac{w}{t} \tag{5.9}$$

$$\chi = \frac{\mathrm{d}W}{\mathrm{d}\xi} = \frac{R}{t}\frac{\mathrm{d}w}{\mathrm{d}r}, \quad S_\mathrm{r} = \frac{\tilde{N}_\mathrm{r}R^2}{Et^3}, \quad S_\theta = \frac{\tilde{N}_\theta R^2}{Et^3} \tag{5.10}$$

and after introducing the initial tension parameter k and the loading parameter P_SRP

$$k = \sqrt{\frac{N_0 R^2}{D}} \quad \text{and} \quad P_\mathrm{SRP} = \frac{p_\mathrm{SRP}R^4}{Et^4} \tag{5.11}$$

Combining Eqs. (5.7) and (5.8), the system can be recast as two second-order coupled equations in the variables χ and S_r

$$\xi^2\chi'' + \xi\chi' - [1 + \xi^2(k^2 + 12(1-\nu^2)S_\mathrm{r})]\chi = 6(1-\nu^2)P_\mathrm{SRP}\xi^3 \tag{5.12}$$

$$\xi^2 S_\mathrm{r}'' + 3\xi S_\mathrm{r}' = -\frac{\chi^2}{2} \tag{5.13}$$

Within the scope of this thesis, no initial in-plane tension is accounted for to maximise the deflection, so the parameter k is zero. The corresponding BCs to solve the boundary value problem (BVP) for a hinged edge support are then

$$\left.\begin{aligned}\chi &= 0\\ S_\mathrm{r} &= 0\end{aligned}\right\} \text{for } \xi = 0 \quad \text{and} \quad \left.\begin{aligned}\chi'' &= 0\\ S_\mathrm{r}' + (1-\nu)S_\mathrm{r} &= 0\end{aligned}\right\} \text{for } \xi = 1 \tag{5.14}$$

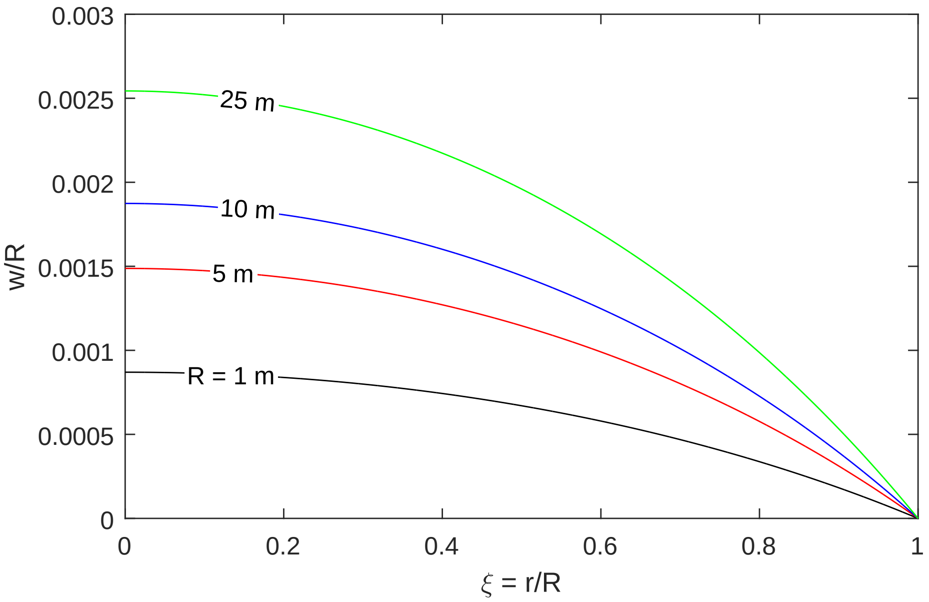

Figure 5.3: Reproduction of relative out-of-plane deflection for Mylar films ($t = 1\,\mu$m) at 1 AU for different membrane radii, as considered in [113].

This type of support was chosen to represent the real conditions in the best way, since the (assumed rigid) hoop structure inhibits membrane deflections in radial direction, but allows for a non-zero slope $\mathrm{d}W/\mathrm{d}\xi$ at the edges.

In principle, the above BVP can be solved for any radial-symmetric load distribution $P_{\mathrm{SRP}}(\xi)$ [109]. After finding a solution for $\chi(\xi)$, the relative membrane deflection is obtained through

$$W = \frac{w}{d} = \int \chi \, \mathrm{d}\xi \tag{5.15}$$

The BVP is solved numerically using the MATLAB$^{\mathrm{TM}}$ *bvp4c* routine that employs a three-stage Lobatto IIIa collocation method [106]. The implementation was validated using results observed in Ref. [112] for Silicon Nitride membranes with clamped-edge support under uniform vertical load, showing that the deflections found and non-dimensional in-plane tensions $S_{\mathrm{r}}(\xi)$ could be reproduced (results not included here). Furthermore, the chosen approach was validated with a numerical FEM analysis conducted in Ref. [113], using circular polyester Mylar films (density $\tau = 1{,}350\,\mathrm{kg/m^3}$, $E = 3.5 \times 10^9\,\mathrm{N/m^2}$, $\nu = 0.38$ and $t_{\mathrm{Mylar}} = 1.0 \times 10^{-6}$ m) of varying radius, subjected to uniform vertical light pressure at the Earth's distance from the Sun (1 AU). Figure 5.3 shows the relative out-of-plane deflections obtained when solving the coupled ODE system for the same conditions. The (relative) central deflections w_0/R are in the order of 0.2% and in good agreement with the results found in Ref. [113]. Note that Ref. [113] takes the variation of SRP magnitude due to the local deflection angle of the surface into account: the film deflection changes the local light incidence angle, cf. cone angle α in Eq. (2.7), reducing the nominal SRP load. However, comparing the results in Fig. 5.3 with Ref. [113] indicates that this effect is negligible, due to very small slope angles of the deflected surface.

5.2 Nominal membrane deflection for constant reflectivity

As noted in Section 1.1.2, the material likely to be employed for future space reflectors is Kapton, due to its higher resistance to heat and radiation compared to Mylar. Accordingly, the deflection properties of a Kapton membrane ($t_{\mathrm{Kapton}} = 2.5 \times 10^{-6}\,\mathrm{m}$, $E = 2.48 \times 10^9\,\mathrm{N/m}^2$ and $\nu = 0.34$ [114]) are investigated in the following. Figures 5.4 and 5.5 show the relative membrane deflections obtained for different hoop radii $R = 1, 5, 10, 25, 50$ and $100\,\mathrm{m}$, and for solar distances $R_{\mathrm{S}} = 0.5, 0.75, 1.0, 1.5, 2.5$ and $3.0\,\mathrm{AU}$, using a 100 m radius membrane for the second figure. The dashed lines indicate ideal parabolic reference curves that satisfy the same boundary conditions and the same central deflection. As can be seen, the deflected profiles obtained are clearly not ideal paraboloids, as will be discussed below. The figures also show the increase in central deflection for larger membrane sizes and smaller solar distances, as expected. In general, all absolute deflections remain below 0.6 m, even for relatively large mem-

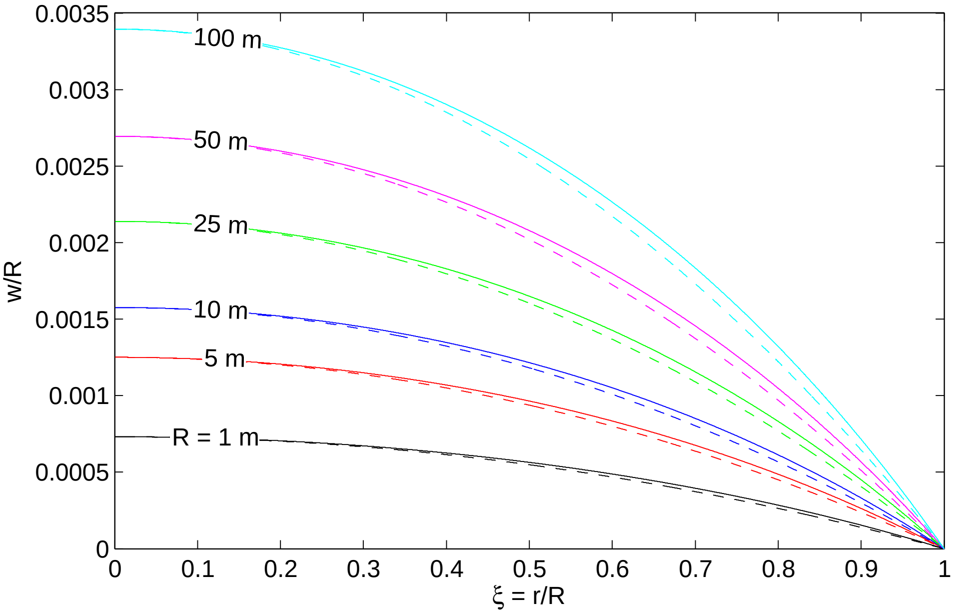

Figure 5.4: Relative out-of-plane deflection for Kapton membrane ($t = 2.5\ \mu$m) at 1 AU for different membrane radii (solid lines) and ideal parabolic reference curves (dashed lines).

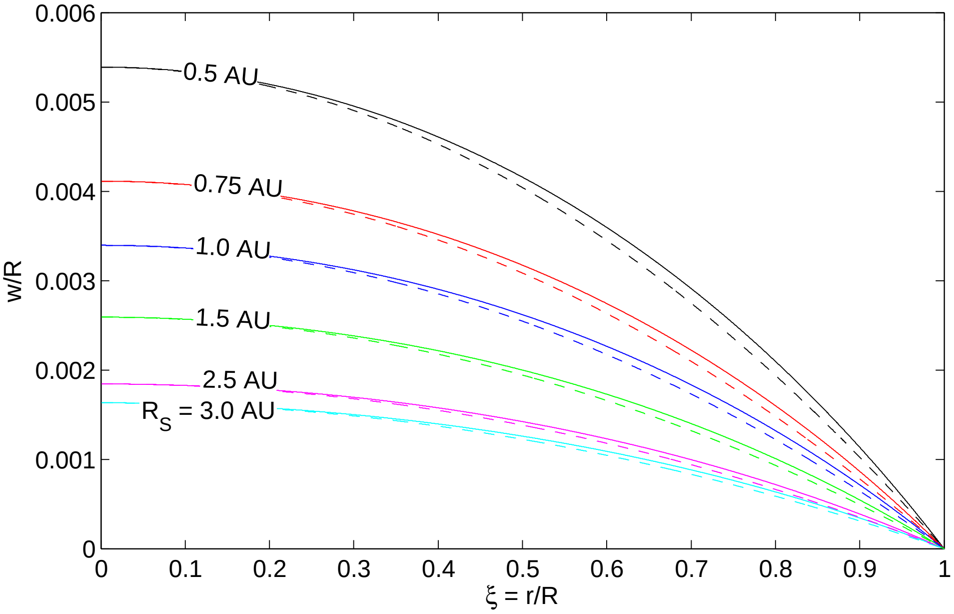

Figure 5.5: Relative out-of-plane deflection for Kapton membrane ($R = 100\,\mathrm{m}$, t = 2.5 μm) at different solar distances (solid lines) and ideal parabolic reference curves (dashed lines).

branes (100 m radius) and close to the Sun (0.5 AU). This already indicates large focal distances when using the membrane as a solar power collector or antenna. The achievable focal distances will be discussed in Section 5.4. The maximum radial tensile stress is found to be $\sigma_{\max} = N_{r,c}/t = 7.595 \times 10^4\,\mathrm{N/m^2}$ at the centre for a membrane radius of $R = 100\,\mathrm{m}$ at 0.5 AU. Compared to the ultimate tensile strength of Kapton, which is $\sigma_{\mathrm{lim}} = 2.31 \times 10^8\,\mathrm{N/m^2}$ (at 23° Celsius) and $1.39 \times 10^8\,\mathrm{N/m^2}$ (at 200° Celsius) [114], the maximum stresses never exceed 0.05 % of the limit load case. This indicates that even much thinner membranes could be employed for future space membrane reflectors.

Polynomial fits of different order are applied to the deflection curves to characterise their shape, which is found to be in good agreement with a third order (cubic) approximation. This trend is shown in Fig. 5.6 for a 100 m radius membrane at 1 AU, together with a parabolic fit using a second-order (parabolic) polynomial. Both polynomial fits are constrained to the central deflection value w_0/R. The cubic fit (dotted blue line) is almost identical with the deflection curve (solid black line). Although the parabolic fit (dashed red line) does not match the BC at the outer edge exactly, it represents a better second-order fit than the parabolic reference curves used in Figs. 5.4 and 5.5. The deviation of the membrane deflection curve from the ideal parabolic shape is most visible in the mid-region of the membrane. Here, the local gradient $\mathrm{d}w/\mathrm{d}\xi$ is

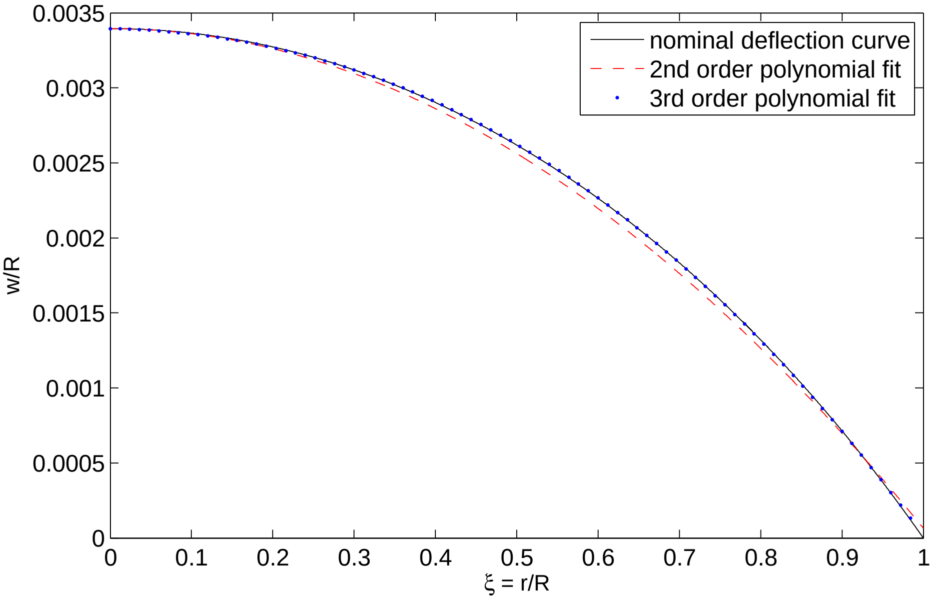

Figure 5.6: Nominal deflection curve for uniform load using Kapton membrane ($R = 100\,\mathrm{m}$, $t = 2.5\,\mu\mathrm{m}$) at 1 AU (black line), and second and third-order polynomial fits, constrained to central deflection value w_0/R.

smaller than the gradient of the parabola and vice-versa close to the outer edge. This indicates that the Kapton surface will not concentrate incoming light (or other forms of electro-magnetic radiation) into a single focal point due to distortion. In particular, the cubic surface reflects incoming light at the mid-part towards larger focal lengths and vice-versa for light impinging on the outer region. In the following, it will be shown that the cubic deflection can be corrected to a true parabolic one using non-uniformly distributed reflectivity across the membrane surface.

5.3 Shape control using variable surface reflectivity

In order to change the nominal deflection shapes that were found for a uniform light pressure load, the surface reflectivity distribution across the membrane needs to be controlled. As seen in Eq. (2.7), a modulated SRP load can be employed by incorporating the reflectivity $\rho(\xi)$ as a function of the position ξ across the surface. Thus, when uniformly distributing electro-chromic coatings across the surface, the reflectivity function directly represents the SRP load distribution. Solving Eq. (2.7) for $\rho(\xi)$ results in

$$\rho(\xi) = \frac{p_{\mathrm{SRP}}(\xi)}{p_0}\left(\frac{R_{S,0}}{R_S}\right)^{-2} - 1 \tag{5.16}$$

where an arbitrary symmetric load function $p_{\mathrm{SRP}}(\xi)$ can be used, as long as the physical constraint for $\rho(\xi) \in [0, 1]$ is satisfied. This property is now used to control the membrane shape, neglecting again the additional mass and thickness that would be introduced to the membrane when distributing an electro-chromic coating layer on the surface.

Expressing $p_{\mathrm{SRP}}(\xi)$ in terms of the non-dimensional load parameter P_{SRP} in Eq. (5.11) yields

$$P_{\mathrm{SRP}}(\xi) = \frac{p_{\mathrm{SRP}}(\xi) R^4}{E t^4} \tag{5.17}$$

Substitution of Eq. (5.17) for the uniform load distribution P_{SRP} within the coupled ODE system, Eq. (5.12), introduces an arbitrary (radial symmetric) load function into the system that can be solved as a BVP, with corresponding boundary conditions at the centre and at the edges.

5.3.1 Inverse problem approach for given shape profile

An inverse problem can now also be formulated, which is defined as calculating the necessary reflectivity function $\rho(\xi)$ to obtain a given membrane deflection shape $W(\xi)$. This can be, for example, a parabolic shape in order to use the membrane as a large antenna, telescope or solar power satellite. A parabolic deflection curve, as used already in Figs. 5.4 and 5.5, has the generic form

$$W_{\mathrm{p}}(\xi) = -A\xi^2 + B\xi + C \tag{5.18}$$

The coefficient A is the curvature and C is the vertex of the parabola. The parameter B is zero, because $W_{\mathrm{p}}(\xi)$ has no horizontal offset from the symmetry axis, which could only be created through an asymmetric load. When inserting the ideal parabolic curve into the coupled ODE system, it can be solved for $P_{\mathrm{SRP}}(\xi)$ in order to obtain the load distribution necessary to create this curve. Rearranging Eq. (5.12) for $P_{\mathrm{SRP}}(\xi)$ and Eq. (5.13) for the non-dimensional in-plane tension $S_{\mathrm{r}}(\xi)$ gives

$$P_{\mathrm{SRP}}(\xi) = \frac{1}{\nu^*}\left[\frac{W''''}{\xi} + \frac{W'''}{\xi^2} - [1 + \xi^2(k^2 + 2\nu^* S_{\mathrm{r}})]\frac{W'}{\xi^3}\right] \tag{5.19}$$

$$S_{\mathrm{r}}'' = -\frac{3}{\xi} S_{\mathrm{r}}' - \frac{1}{2\xi^2}(W')^2 \tag{5.20}$$

using the Poisson parameter $\nu^* = 1 - \nu^2$. Inserting the parabolic curve $W_\mathrm{p}(\xi)$ for W, the above equations now become

$$P_\mathrm{SRP}(\xi) = 4AS_\mathrm{r} \tag{5.21}$$

$$S_\mathrm{r}'' = -\frac{3}{\xi}S_\mathrm{r}' - 2A^2 \tag{5.22}$$

Equation (5.22) can be solved in general for S_r, without specifying boundary conditions

$$S_\mathrm{r} = -\frac{1}{4}A^2\xi^2 - \frac{C_1}{2\xi^2} + C_2 \tag{5.23}$$

When again using the boundary conditions for a hinged edge support, Eq. (5.14), the above equation becomes

$$S_\mathrm{r} = -\frac{1}{4}A^2\xi^2 + \frac{1}{4}\frac{3-\nu}{1-\nu}A^2 \tag{5.24}$$

Inserting Eq. (5.24) into Eq. (5.21), the load distribution associated with a general parabolic deflection curve can now be written as

$$P_\mathrm{SRP}(\xi) = -A^3\xi^2 + \frac{3-\nu}{1-\nu}A^3 \tag{5.25}$$

which shows that $P_\mathrm{SRP}(\xi)$ is fully determined by the polynomial coefficient A and the Poisson ratio ν.

The inverse problem is now applied to create a parabolic deflection shape for a 100 m Kapton membrane of thickness $t = 2.5\ \mu$m at the Earth's distance from the Sun. Figure 5.7 shows the nominal cubic deflection for constant reflectivity, thus a uniform load distribution. A parabolic reference curve (dotted black line) is taken as input for the inverse problem. In order to match the central deflection of the nominal cubic deflection curve (Fig. 5.4) and the zero-deflection condition at the edge, the coefficients are chosen to be $A = C = W_\mathrm{0,nom}$, where $W_\mathrm{0,nom}$ represents the nominal central deflection obtained for constant reflectivity. Accordingly, the parabolic reference curve is now

$$W_\mathrm{p}(\xi) = \ - W_\mathrm{0,nom}\xi^2 + W_\mathrm{0,nom} \tag{5.26}$$

and by inserting into Eq. (5.25), the light pressure distribution becomes

$$P_\mathrm{SRP}(\xi) = W_\mathrm{0,nom}^3\left(\frac{3-\nu}{1-\nu} - \xi^2\right) \tag{5.27}$$

After introducing this function into the coupled ODE system, it can be solved as a regular BVP. As can be seen in Fig. 5.7, the resulting deflection curve (dashed red line)

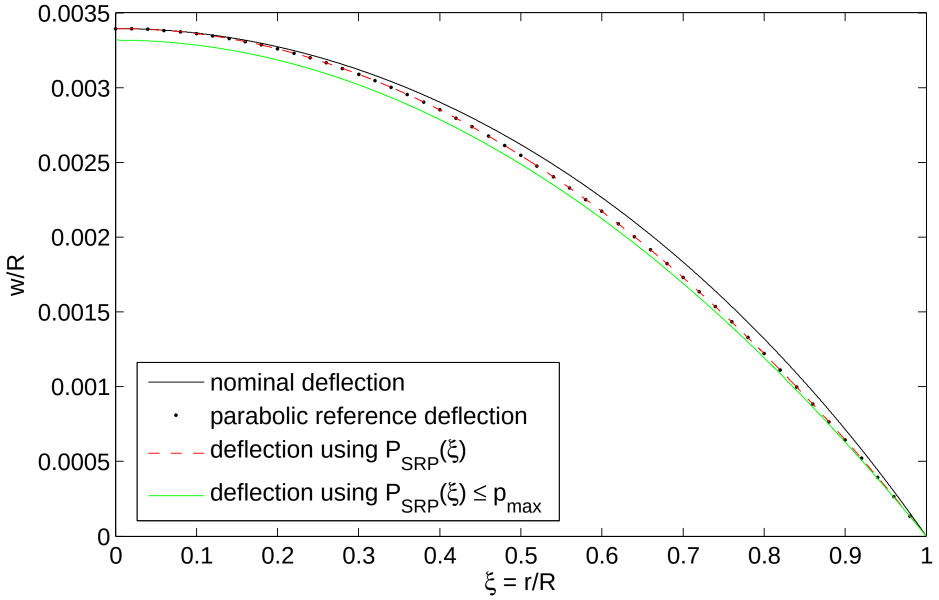

Figure 5.7: Nominal deflection curve for uniform load using Kapton membrane ($R = 100$ m, $t = 2.5$ μm) at 1 AU (black line), parabolic reference curve (dotted line), deflection using distributed load function (dashed red line) and constrained load function (green line).

exactly matches the input curve.

When reformulating Eq. (5.27), the absolute SRP load distribution can be written as

$$p_{\mathrm{SRP}}(\xi) = \frac{Et^4}{R^4} W_{0,\mathrm{nom}}^3 \left(\frac{3-\nu}{1-\nu} - \xi^2 \right) \tag{5.28}$$

However, this distribution does not necessarily match the condition not to exceed the maximum possible light pressure $p_{\max} = 2p_0(R_{S,0}/R_S)^2$ at a certain solar distance or, equivalently, not to exceed the maximum reflectivity $\rho_{\max}(\xi) = 1$. As can be seen in Fig. 5.8, the load distribution for the chosen parabolic deflection case exceeds $p_{\max}$ (dashed red line), showing that it is not possible to achieve the same nominal central deflection when simply constraining the membrane to a parabolic shape. After introducing the additional constraint $p_{\mathrm{SRP}}(\xi) \leq p_{\max}$ into Eq. (5.28), the coefficients $A_{\mathrm{c}} = C_{\mathrm{c}} = W_{0,\mathrm{c}}$ for the constrained parabola can be calculated as

$$W_{0,\mathrm{c}} = \left(\frac{2p_0 R^4}{Et^4} \frac{1-\nu}{3-\nu} \left(\frac{R_{S,0}}{R_S} \right)^2 \right)^{\frac{1}{3}} \tag{5.29}$$

In Eq. (5.29), the constrained central deflection $W_{0,\mathrm{c}}$ is now fully determined by the membrane size, material, thickness and solar distance. The resulting constrained load distribution is also shown in Fig. 5.8 (green solid curve). The respective central deflec-

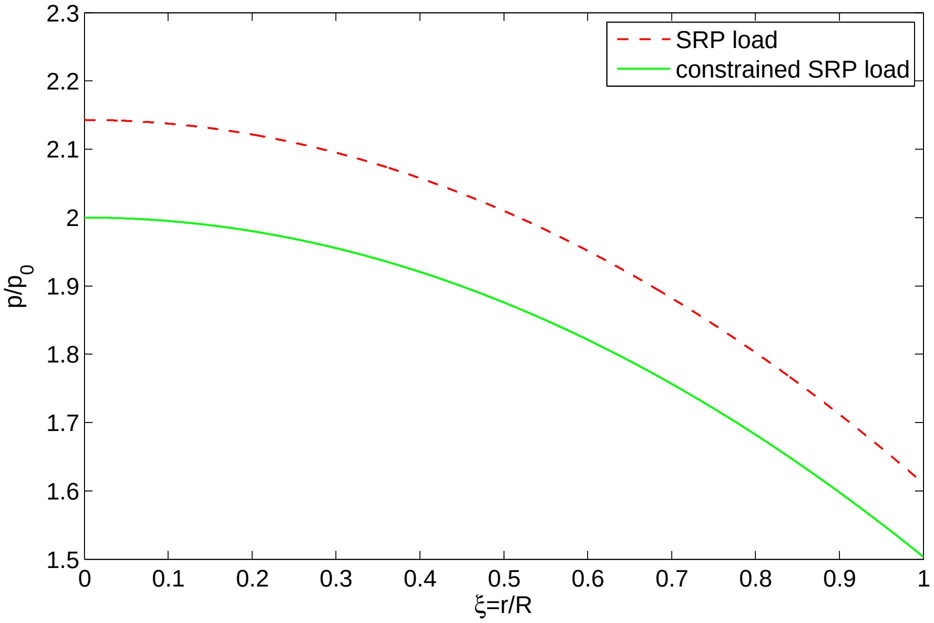

Figure 5.8: Non-dimensional load distribution for unconstrained parabolic deflection curve (dashed red line) and for constrained parabolic deflection (solid green line).

tion is about 3% smaller compared to the unconstrained parabolic deflection curve.

The corresponding reflectivity distribution $\rho(\xi)$ is finally found after inserting the SRP load distribution, Eq. (5.28), into Eq. (5.16)

$$\rho(\xi) = \frac{Et^4}{p_0 R^4}\left(\frac{R_S}{R_{S,0}}\right)^2 W_{0,\mathrm{c}}^3\left(\frac{3-\nu}{1-\nu} - \xi^2\right) - 1 \tag{5.30}$$

After inserting the constraint for the central deflection $W_{0,\mathrm{c}}$ into Eq. (5.30), the reflectivity distribution becomes

$$\rho(\xi) = 1 - \frac{2\,(1-\nu)}{3-\nu}\xi^2 \tag{5.31}$$

It can be seen that the reflectivity distribution for a parabolic deflection shape is independent of the membrane parameters (except the Poisson ratio ν) and solar distance. The latter indicates the possibility of maintaining a parabolic profile at any solar distance, which allows a pre-fabricated, fixed reflectivity distribution on the membrane surface, instead of using electro-chromic coatings. The reflectivity distribution is shown in Fig. 5.9, along with the constrained distribution that satisfies $\rho \leq 1$.

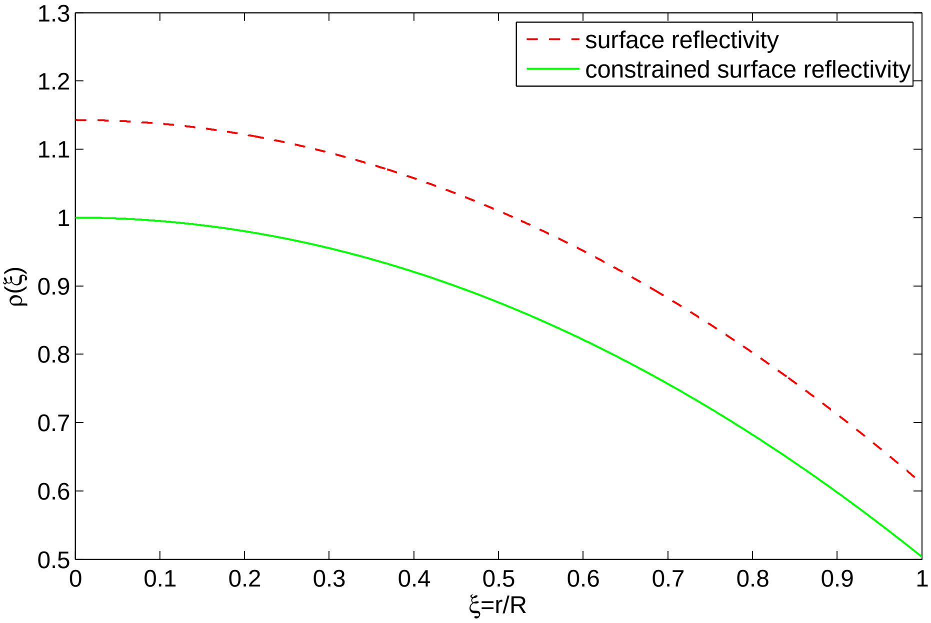

Figure 5.9: Reflectivity distribution for unconstrained parabolic deflection curve (dashed red line) and distribution for constrained parabolic deflection (solid green line).

5.4 Optical performance of elastic membrane reflector

A large reflective parabolic surface deployed in space has many potential applications, such as communication, sensing and power collection. In order to evaluate the performance of the deflected shapes that can be generated, some properties of parabolic membrane reflectors will be assessed in the following. A paraboloid concentrates incoming electro-magnetic radiation into a single focal point, depending on its geometrical precision and surface quality. The corresponding focal length, thus the focal distance from the vertex of the parabola, can be calculated after converting the expression obtained for the central deflection, Eq. (5.29), into dimensional form as

$$w_{0,\mathrm{c}} = \left(\frac{2p_0 R^4}{Et} \frac{1-\nu}{3-\nu} \left(\frac{R_{S,0}}{R_S} \right)^2 \right)^{\frac{1}{3}} \tag{5.32}$$

When also transforming the parabolic reference curve $W_\mathrm{p}(\xi)$, Eq. (5.26), into dimensional form

$$w_\mathrm{p} = W_{0,\mathrm{c}}\, t \left(\frac{r}{R} \right)^2 + W_{0,\mathrm{c}}\, t = \frac{W_{0,\mathrm{c}}\, t}{R^2} r^2 + W_{0,\mathrm{c}}\, t = ar^2 + c \tag{5.33}$$

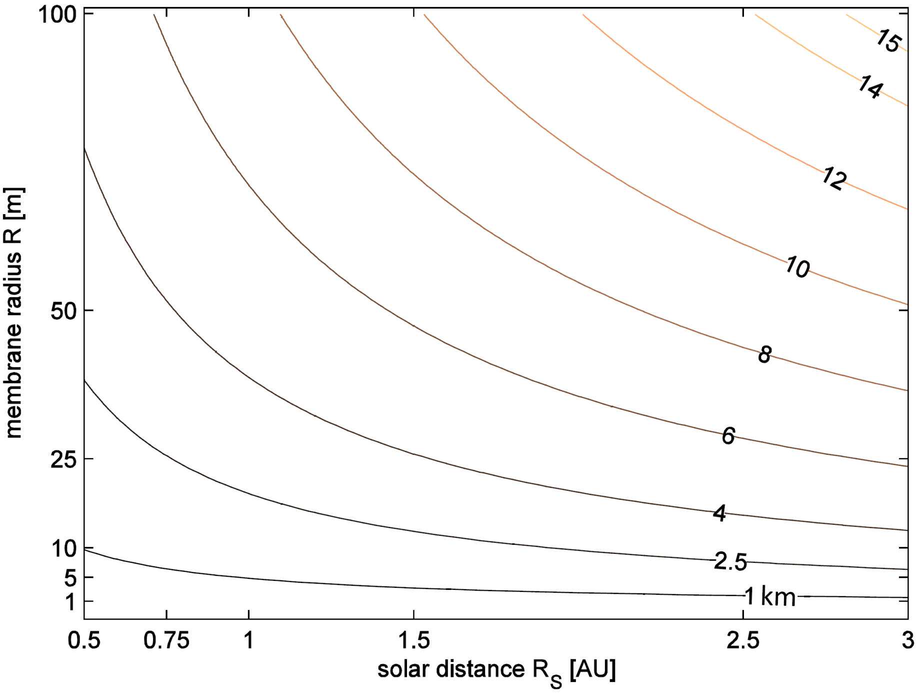

Figure 5.10: Achievable focal length of parabolic space reflector as function of Kapton membrane radius and solar distance.

where $a = w_{0,\text{c}}/R^2$ and $c = w_{0,\text{c}}$, the focal length can now be expressed as

$$f = \frac{1}{4a} = \frac{R^2}{4w_{0,\text{c}}} \tag{5.34}$$

The achievable focal lengths for the deflected Kapton membrane are shown in Fig. 5.10, as a function of radius and solar distance. For example, a deflected membrane of 100 m radius at the Earth's distance from the Sun has a focal length of $f_{\text{Kapton}} = 7.54$ km. However, when employing Mylar films with a currently achievable thickness of only 0.9 μm [115], the focal length could be further reduced to $f_{\text{Mylar}} = 6.11$ km, since the focal length scales with $t^{1/3}$ for the membrane thickness, according to Eqs. (5.32) and (5.34).

For some applications of a space-based optical device, it is desirable to achieve shorter focal lengths in order to operate a receiver/transmitter unit in the focus. This could be achieved either by physically connecting the unit with the space reflector, or more likely through positioning a detached platform at the focus, which is flying in formation with the reflector. Such formation flying is a well understood technology [116].

As can be seen in Figs. 5.11 and 5.12, the trend of the central deflection $w_{0,\text{c}}$ scales with $R^{1/3}$ for the membrane radius and with $1/R_{\text{S}}^{2/3}$ for the solar distance. The former figure

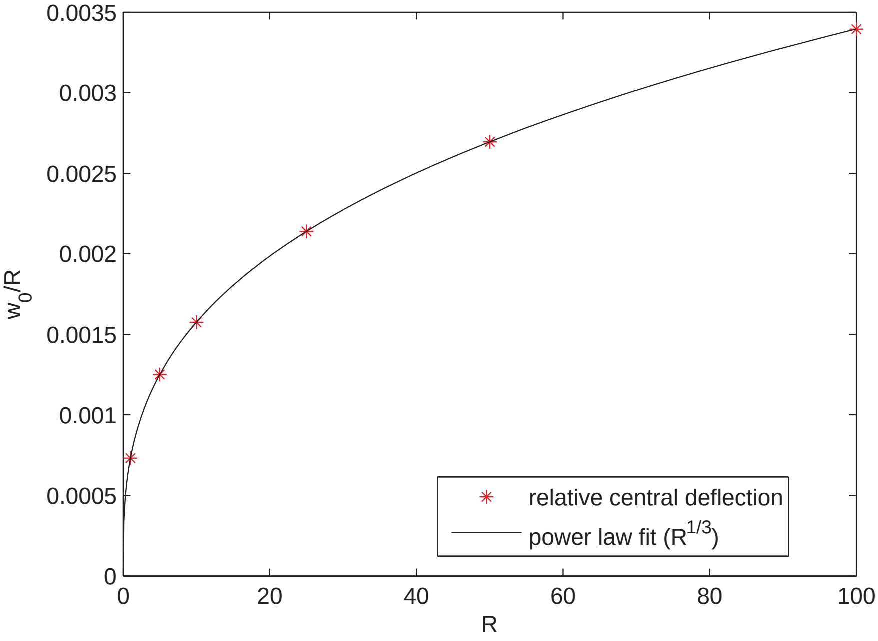

Figure 5.11: Relative central membrane deflection as a function of membrane radius *R* and power-law fit to the data.

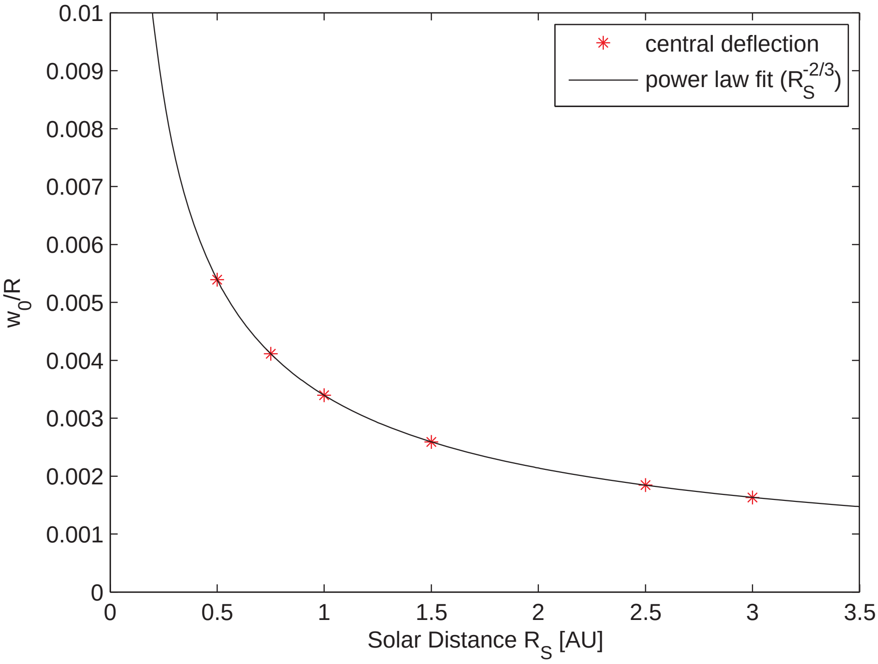

Figure 5.12: Relative central membrane deflection as a function of solar distance R_S and power-law fit to the data.

shows that increasing the membrane radius in order to achieve higher deflections (and thus smaller focal lengths) is not necessarily beneficial, since the resulting deflections do not increase linearly with the membrane size. Accordingly, a very large membrane diameter in the kilometre-range may not outweigh the increase in launch mass and hence launch cost. The latter figure shows that the deflection decreases slower than $1/R_\mathrm{S}^2$ with solar distance (i.e. the rate at which the flux density of solar photons and thus usable electric power scale), indicating that moderate focal lengths are still available at far distances from the Sun.

5.4.1 Solar concentrator performance

So far, the analysis of a paraboloid membrane reflector has been simplified by assuming, for example, ideal geometric conditions and surface properties. This section will determine the effect of these assumptions on the optical performance of the surface by considering the membrane for the use of space solar power collection.

Within the focal length equation, Eq. 5.34, it has been assumed that the incoming Sun rays are parallel to each other, creating a single focal point. Therefore, the concentration ratio

$$C_\mathrm{r} = \frac{A}{A_\mathrm{f}} \tag{5.35}$$

with A the collecting surface area (normal to the Sun) and A_f the area of the reflected spot in the focal plane, is infinitely large. However, the finite angular size of the solar disk results in non-parallel rays incident at each point of the reflective surface, as shown in Fig. 5.13. Accordingly, the reflected rays do not all pass through the focal point, but form an ‘image’ of finite size centred about the focus. The angular size of the Sun (or

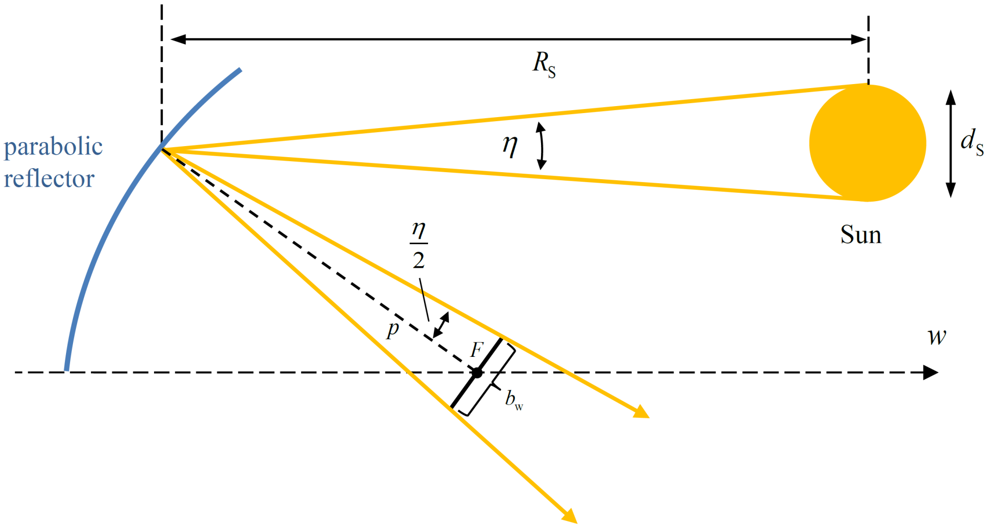

Figure 5.13: Finite angular size η of the Sun’s disk and beam width b_w of the reflected ‘image’ at the focus of a parabolic reflector

any other object) can be calculated as

$$\eta = 2\tan^{-1}\Big(\frac{d_\mathrm{S}}{2R_\mathrm{s}}\Big) \tag{5.36}$$

with $d_\mathrm{S} = 1,391,684\,\mathrm{km}$ the Sun's diameter and R_S the solar distance. Accordingly, the angular size of the Sun disk at Earth distance ($R_\mathrm{S} = 1\,\mathrm{AU}$) is $\eta = 9.3028$ mrad (0.533 deg). As a result, the 'image' size at the focus, the so-called beam width b_w (or beam spread), can be obtained through

$$b_\mathrm{w} = 2f\tan\Big(\frac{\eta}{2}\Big) \tag{5.37}$$

according to Fig. 5.13 and assuming that the line p through the focus and the focal length f are of the same length, thus $p \approx f$. Therefore, the beam width depends on the overall focal length of the paraboloid surface, according to Eq. 5.34. This is the minimum beam spread that will occur. Any errors in, for example, the precision of the mirror slope will cause additional spreading of the image size. For the elastic membrane, using the focal length $f_\mathrm{Kapton} = 7.54$ km, calculated earlier for an $R = 100\,\mathrm{m}$ radius reflector at Earth distance from the Sun, the beam width would be $b_{\mathrm{w},100} = 70.14\,\mathrm{m}$. According to Eq. 5.35, the concentration ratio would be

$$C_{\mathrm{r},100} = \frac{A}{A_\mathrm{f}} = \frac{\pi R^2}{\pi(b_\mathrm{w}/2)^2} = 4\frac{R^2}{b_\mathrm{w}^2} \approx 8 \tag{5.38}$$

This result suggests a quite low efficiency of the collector, while the receiver surface in the focal plane needs to be impractically large. However, as seen from Eq. 5.37, the beam width largely depends on the focal length, which is in the kilometre range for elastic membranes deflected by SRP. In Chapter 6, a method to reduce the focal length by increasing the surface deflection will be introduced. Consequently, the resulting beam width in the focal plane is expected to be smaller.

The collection efficiency of the reflector also strongly depends on the membrane surface quality. Clearly, an ideal mirror ($\rho = 1$) provides the highest performance due to specular reflection of the sunlight. However, when changing the reflectivity distribution in order to introduce optical control of the membrane deflection, the specular reflection requirement can no longer be met. This will cause power collection losses due to non-ideal reflection. The total collected solar power of the reflector, including a variable reflectivity distribution across the membrane, is

$$W_\mathrm{tot} = W_{\mathrm{S},0}A\,\rho(r) \tag{5.39}$$

with $W_{\mathrm{S},0} = 1368\ \mathrm{W/m^2}$ the solar constant, according to Section 2.1, and $\rho(r)$ the (symmetric) reflectivity function in radial direction. According to the simplified SRP model introduced in Section 2.2.2, a surface reflectivity $\rho < 1$ causes the fraction of photons not undergoing specular reflection to be absorbed by the surface. Consequently, such photons do not contribute to the total collected power in the aperture focus. Equation 5.39 can be solved when introducing the reflectivity function found from the inverse problem that creates a parabolic surface. After inserting Eq. 5.31, Eq. 5.39 can be rewritten as

$$W_{\mathrm{tot}} = W_{\mathrm{S},0} \int_0^{2\pi} \int_0^R r \left(1 - \frac{2\,(1-\nu)}{3-\nu} \left(\frac{r}{R}\right)^2\right) \mathrm{d}r\, \mathrm{d}\theta \tag{5.40}$$

with θ the surface angle in circumferential direction. Integrating Eq. 5.40 results as

$$W_{\mathrm{tot}} = W_{\mathrm{S},0} \pi R^2 \left(1 - \frac{2\,(1-\nu)}{3-\nu}\right) \tag{5.41}$$

As can be seen from the previous equation, the term $W_{\mathrm{S},0}\pi R^2$ represents the total collected power in case of specular reflection across the entire surface. However, after introducing the Poisson ratio of Kapton ($\nu = 0.34$) into Eq. 5.41, the effective collected solar power is obtained as

$$W_{\mathrm{tot}} = W_{\mathrm{S},0} \pi R^2\, 0.7519 \tag{5.42}$$

The result suggests that approximately 75% of the total power collected by the surface can effectively be reflected into the focus.

5.5 Chapter summary

It has been shown in this chapter that the deflection shape of a circular membrane reflector exposed to vertical SRP loads can be controlled by changing the reflectivity distribution across the surface. At first, using non-linear thin membrane theory, the nominal deflection due to a uniform light pressure distribution has been calculated for various membrane diameters and solar distances. The results showed a cubic polynomial deflection curve, which indicates that the deflected surface does not naturally concentrate incoming light (or other forms of electro-magnetic radiation) into a single focal point due to non-parabolic distortion. However, by formulating an inverse problem to obtain the required load distribution for a given (e.g. parabolic) profile, an analytical expression for the reflectivity function across the surface has been derived, enabling a true parabolic deflection shape. As for the vertical SRP load cases investigated, this reflectivity function is radially symmetric and does not depend on membrane size, thickness or solar distance. The latter will enable a parabolic profile at any solar distance and thus to potentially prefabricate a fixed reflectivity distribution on the membrane surface, instead of using electro-chromic coatings.

Although the absolute deflection and thus focal length changes with solar distance, this can be compensated for by a detached receiver/transmitter platform that is flying in formation at the current focus. All absolute membrane deflections for a 2.5 μm Kapton film have been found to be smaller than 0.6 m, even for relatively large membranes (100 m radius) and close to the Sun (half the Sun-Earth distance), while no initial in-plane tension has been accounted for to maximise the deflection. The focal lengths of the resulting parabolic reflectors have been calculated, resulting for example in a focal length of 7.54 km for a 100 m radius membrane at the Earth's distance from the Sun. Finally, when employing Mylar films with a currently achievable thickness of only 0.9 μm, the focal length could be further reduced to 6.11 km, since the deflection increases for smaller membrane thickness.

Chapter 6

Shape control of slack space reflectors

In the previous chapter, optical shape control was used to create paraboloid-type deflection profiles for tensioned elastic membranes. In order to reduce the achievable focal distance of the aperture, this chapter will consider the shape control of slack 'membrane-like' surfaces. This will enable very large membrane reflectors with the focal point close to the reflector itself. To this aim, Section 6.1 will introduce the concept of modelling the circular film using 'catenary-type' radial strings, suspended in between a rigid hoop. This approximation enables a semi-analytic investigation of ideally slack surfaces involving very large deflections. The governing equations of the string, subject to various distributed loads, will be presented in Section 6.2. In Section 6.3, the resulting deflection profiles for all load cases will be compared. The manipulation of the nominal deflection profiles to generate parabolic shapes through the use of suitable reflectivity functions will be discussed in Section 6.4. The resulting deflections will be assessed in Section 6.5 in terms of the achievable focal lengths. The chapter will end with conclusions.

6.1 Modelling slack gossamer surfaces

It has been demonstrated in Chapter 5 that the central deflection of a thin tensioned membrane due to SRP is below one percent of the aperture radius. The resulting focal lengths were found to be in the range of a few kilometres. This imposes ambitious requirements on the relative position of an emitter/receiver unit at the aperture focus. For this reason, an alternative concept to reduce the focal distance will be investigated in this chapter. According to Eq. (5.34), the larger the central deflection of a parabolic surface, the smaller its focal length. Therefore, considering a slack reflective surface

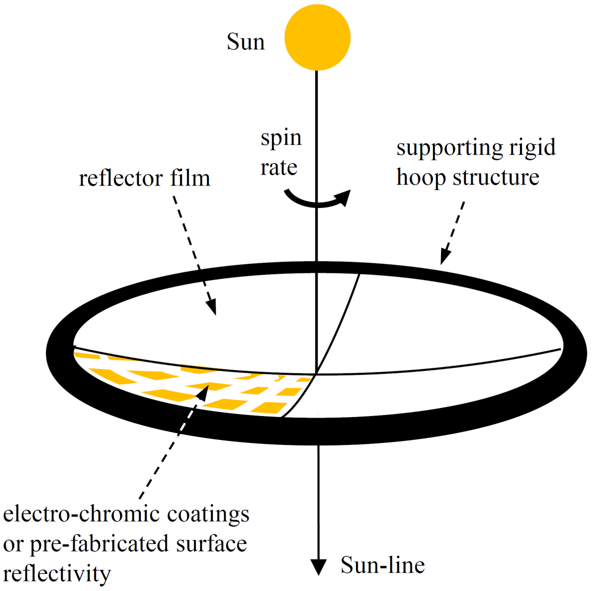

Figure 6.1: Spin-stabilised space reflector with slack suspended film attached to rigid hoop structure and surface covered with electro-chromic coatings

should result in larger deflections due to SRP. In order to investigate this effect, a slack suspended reflector film is now considered, attached to a spin-stabilised rigid hoop structure, as shown in Fig. 6.1. The mass of the hoop is assumed to be much larger than the film, while the surface (including electro-chromic coatings) is assumed to be of uniform thickness (isotropic). The additional mass introduced by the coating layer is included in the surface areal density.

The corresponding equations are derived from idealising the two-dimensional (2D) surface as a 'cobweb' of radially spanned 1D strings (or threads), as can be found, for example, in natural spider webs. As shown in Fig. 6.2, these grid-like structures consist of radial 'carrier threads' to carry the load of the web and slack circumferential 'capture threads' to hold the prey [118]. It has been shown that the static structural integrity of spider webs remains intact even when multiple capture threads are damaged, indicating that they are not contributing to carrying the web's own weight. Applying this analogy to the slack film, circumferential tension is ideally assumed to be zero and only radial forces are considered. When further ignoring the usually quite significant elasticity of spider webs, the reflector surface can be approximated as a set of inextensible, infinitely flexible strings. Throughout this analysis, inextensible means that the film material is rigid to applied tensile loads and flexible means that the thin film cannot absorb bending moments or shear stresses. The radial strings are suspended from the rigid hoop structure in a catenary-like manner and intersect at the centre of the circular surface, as shown in Fig. 6.3. By increasing the total slack length of the

Figure 6.2: Natural spider web consisting of radially spanned 'carrier threads' (in vertical direction) and circumferential 'capture threads' in horizontal direction (image source: [117])

strings, thus by suspending more material in between the fixed hoop, the sagging is expected to increase accordingly. As a result, the focal length of the deflected surface could be modified and, ultimately, minimised.

6.2 Catenary-type deflection

The deflection of a slack inextensible catenary-type string of uniform thickness, subject to different load distributions, are presented in this section. As shown in Fig. 6.4, the string is supported by a rigid outer hoop of radius R and diameter D, forming hinged-support type boundary conditions at the edges. The mathematical model idealises the string by assuming that it is thin enough to be regarded as a 1D curve. The ordinary differential equation (ODE) describing the static deflection (as a function of the radial position r along the curve) is derived from the equilibrium of forces over a curve segment of length Δs, thickness t and depth h, according to Fig. 6.4. The load case of a uniform vertical field of gravity is described first in order to demonstrate that the catenary profile differs from the required parabolic deflection. Following this, a generic pressure distribution, centrifugal forces and finally SRP (using a constant surface reflectivity) are introduced into the model.

6.2.1 Equations of the classical catenary

The classical equation of catenary deflection due to gravity (commonly termed as a 'hanging chain') can be found in the literature, as derived by Leibniz, Huygens and

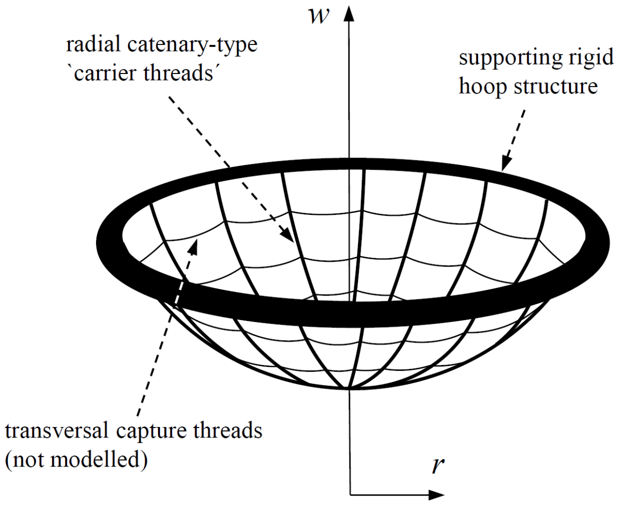

Figure 6.3: Circular reflector film modelled as a cobweb of slack radial 'carrier threads', suspended from a rigid supporting hoop structure. Circumferential 'capture threads' ideally carry no tension and are not considered in the model

Bernoulli in 1691 [119]. Ideally, the infinitesimal chain links are connected by friction-free hinges and thus cannot absorb bending moments. Considering a small chain (curve) segment Δs, the external force $\Delta\mathbf{G}$ due to vertical gravity is

$$\Delta\mathbf{G} = -\tau g A\,\Delta s\,\mathbf{w} \tag{6.1}$$

where $\mathbf{w}$ is the unit vector in the vertical direction, τ is the density of the material, g is the gravitational acceleration and A is the (constant) cross-sectional area of the segment, according to Fig. 6.4. Furthermore, the internal (restoring) forces are the tension forces $T(r)$ and $T(r+\Delta r)$, respectively, acting in the tangential direction at the radial position r and $(r+\Delta r)$ of the curve segment. The angle φ denotes the local pitch angle of the segment between the horizontal axis and the tangential direction. The equilibrium conditions over the segment in the r (radial) and w (vertical) direction can be written as

$$-T(r)\cos\varphi(r) + T(r{+}\Delta r)\cos\varphi(r{+}\Delta r) = 0 \tag{6.2a}$$

$$-T(r)\sin\varphi(r) + T(r{+}\Delta r)\sin\varphi(r{+}\Delta r) = -\Delta G \tag{6.2b}$$

It can be seen from Eq. (6.2a) that the horizontal tension force component is always constant along r

$$T\cos\varphi = T_0 = \text{const} \tag{6.3}$$

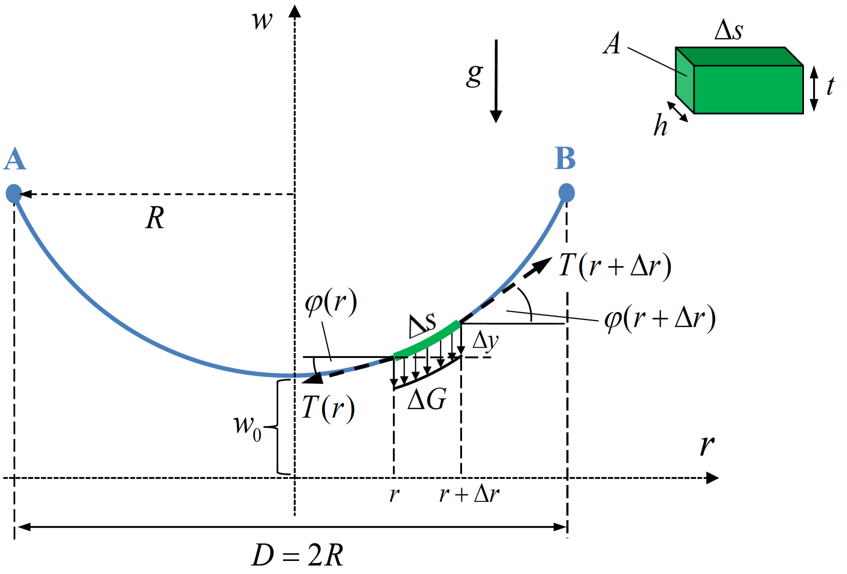

Figure 6.4: Deflection model of classical catenary, with force equilibrium over segment Δs in vertical gravitational field

with a constant tension force T_0. After taking the limit $\Delta s \to 0$, the vertical component, Eq. (6.2b), can be rewritten as

$$\mathrm{d}(T \sin\varphi) = -\mathrm{d}G \tag{6.4}$$

and after introducing Eq. (6.3)

$$T_0\, \mathrm{d}(\tan\varphi) = -\mathrm{d}G \tag{6.5}$$

Defining $\tan\varphi(r) = \mathrm{d}w/\mathrm{d}r = w'$, where $\square'$ denotes the derivative in the radial direction, according to Fig. 6.4, the equilibrium equation is written in differential form as

$$T_0\, \mathrm{d}w' = \tau g A\, \mathrm{d}s \tag{6.6}$$

Considering now the arc length equation

$$\Delta s = \left(\Delta r^2 + \Delta w^2\right)^{\frac{1}{2}} = \left(1 + \left(\frac{\Delta w}{\Delta r}\right)^2\right)^{\frac{1}{2}} \Delta r \tag{6.7}$$

and taking the limit $\Delta s \to 0$, such that

$$\mathrm{d}s = (1 + w'^2)^{\frac{1}{2}} \mathrm{d}r \tag{6.8}$$

this relation can be introduced into Eq. (6.6). The resulting ODE describes the deflected catenary in a gravitational field

$$w'' = \frac{\tau g A}{T_0}(1 + w'^2)^{\frac{1}{2}} \tag{6.9}$$

with tension at the centre T_0. Introducing the gravity force coefficient $a_{\mathrm{G}} = T_0/(\tau g A)$, this coefficient determines the geometrical shape of the catenary curve, as will be described below.

The resulting deflection curve due to gravity (subscript G) can be obtained analytically through integration of Eq. (6.9) as

$$w'_{\mathrm{G}} = \sinh\left(\frac{r}{a_{\mathrm{G}}}\right) + c_1 \tag{6.10}$$

with $c_1 = 0$, after introducing the BC $w'_{\mathrm{G}}(0) = 0$. Further, integration gives

$$w_{\mathrm{G}} = a_{\mathrm{G}} \cosh\left(\frac{r}{a_{\mathrm{G}}}\right) + c_2 \tag{6.11}$$

with $c_2 = -a_{\mathrm{G}} \cosh\big(R/a_{\mathrm{G}}\big) = c_{\mathrm{G}}$, after introducing the BC $w_{\mathrm{G}}(R) = 0$. The deflection curve for the classical gravity catenary can thus be written as

$$w_{\mathrm{G}} = a_{\mathrm{G}} \cosh\left(\frac{r}{a_{\mathrm{G}}}\right) + c_{\mathrm{G}} \tag{6.12}$$

with a_{G} and c_{G} in units of length. The two coefficients together define the deflection $w_{0,\mathrm{G}}$ at the centre, where $\cosh(0) = 1$. Accordingly, the central deflection is

$$w_{0,\mathrm{G}} = a_{\mathrm{G}} \cosh(0) + c_{\mathrm{G}} = a_{\mathrm{G}}\left(1 - \cosh\left(\frac{R}{a_{\mathrm{G}}}\right)\right) \tag{6.13}$$

The resulting catenary curve when setting $a_{\mathrm{G}} = 1$ and $R = 1$ is shown in Fig. 6.5, together with the corresponding parabolic reference curve $w_{\mathrm{p}} = a_{\mathrm{p}} r^2 + c_{\mathrm{p}}$ of the same central deflection $w_{0,\mathrm{p}} = w_{0,\mathrm{G}}$ and BC $w_{\mathrm{p}}(R) = 0$. As can be seen, the two curves are not identical, with the catenary curve being more deflected than the parabola. As a note, it was only in 1669 when Jungius disproved Galileo's claim that the curve of a chain hanging under gravity would be a parabola [119].

According to Eq. (6.12), the coefficient a_{G} completely defines the shape of the catenary curve. Although the value of the central tension force T_0 is unknown, the coefficient a_{G} can be calculated when introducing an additional constraint for the total curve length. Without derivation, the total arc length S_{G} of the catenary curve can be calculated as

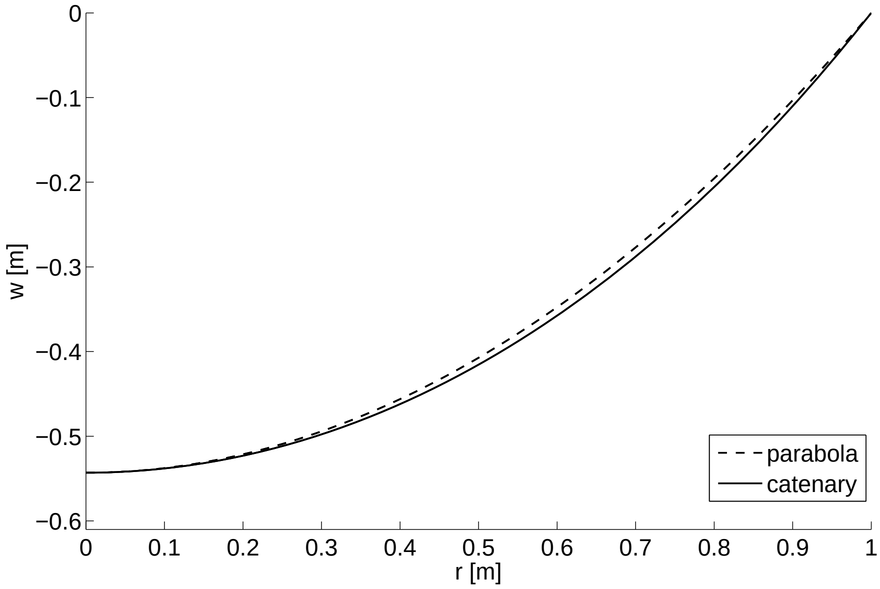

Figure 6.5: Comparison of catenary curve w_{G} and parabolic curve w_{p} of same central deflection w_0 and radius $R = 1$

[119]

$$S_{\mathrm{G}}(R) = a_{\mathrm{G}} \sinh\left(\frac{R}{a_{\mathrm{G}}}\right) \tag{6.14}$$

This transcendental equation in a_{G} can only be solved numerically. However, inserting a_{G} obtained for a specified total catenary length S_{G} and radius R into Eq. (6.12) results in the corresponding deflection curve. Thus, knowing the value of T_0 is not necessary to find a_{G}, as it can be computed as a function of R and S_{G}.

6.2.2 Deflection due to generic pressure and centrifugal forces

The previously introduced deflection model for a hanging chain is now extended by considering a generic pressure distribution $p(r)$, as shown in Fig. 6.6(a). Furthermore, centrifugal forces, acting on a spin-stabilised reflector disk, are introduced into the model. Centrifugal forces are exploited, since such a large spacecraft structure can be stabilised by rotation very efficiently, without introducing additional mass through mechanical attitude-control systems.

Considering again a small curve segment of length Δs, the forces acting on the segment are now given by the pressure force vector $\Delta \mathbf{F}_{\mathrm{P}}$, which is always normal to the segment,

$$\Delta \mathbf{F}_{\mathrm{P}}(r) = -p(r) h \Delta s\, \mathbf{n} \tag{6.15}$$

with the segment's surface area $h\Delta s$, according to Fig. 6.4, and the centrifugal force

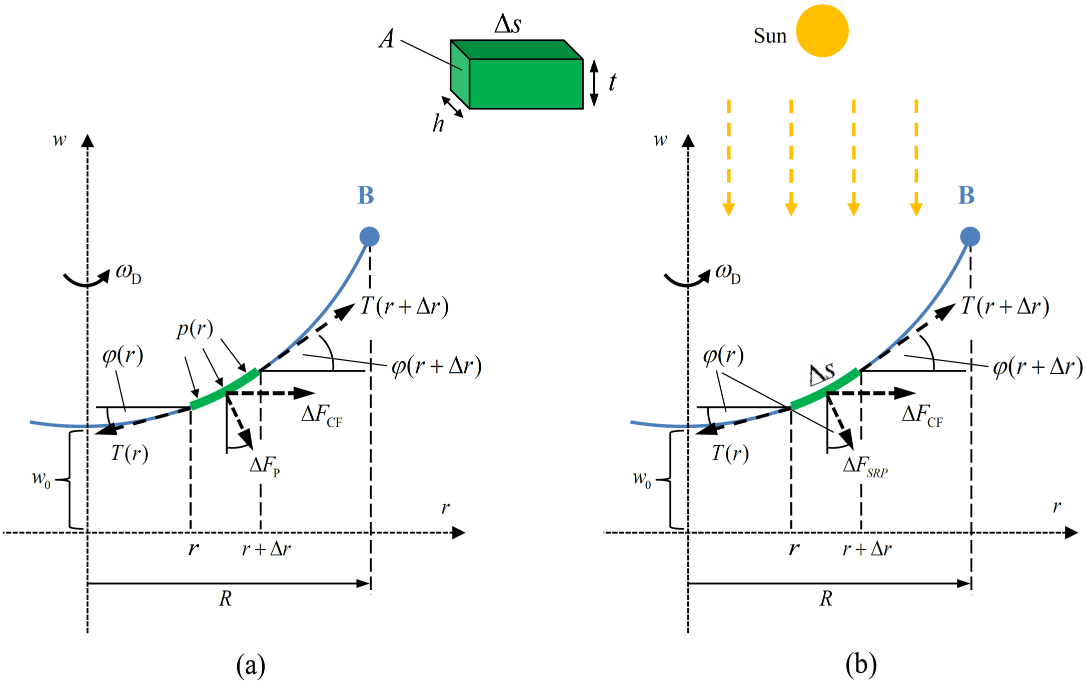

(a) (b)

Figure 6.6: Deflection models of slack catenary-type string, with force equilibrium over segment Δs under (a) generic pressure, and (b) uniform SRP load, with centrifugal force $\boldsymbol{F}_{\mathrm{CF}}$, due to spin-stabilised reflector disk with constant angular rate ω_{D} about w-axis

vector

$$\Delta\mathbf{F}_{\mathrm{CF}}(r) = \Delta m\,\omega_{\mathrm{D}}^2\,r\,\mathbf{r} \tag{6.16}$$

with ω_{D} the constant angular velocity of the disk and Δm the mass of the segment, such that

$$\Delta m = \tau A \Delta s \tag{6.17}$$

The two equilibrium conditions over a curve segment in the r and w directions are now

$$-T(r)\cos\varphi(r) + T(r+\Delta r)\cos\varphi(r+\Delta r) = -p(r)\sin\varphi(r)h\Delta s - \tau A\,\omega_{\mathrm{D}}^2 r\Delta s \tag{6.18a}$$

$$-T(r)\sin\varphi(r) + T(r+\Delta r)\sin\varphi(r+\Delta r) = \quad p(r)\cos\varphi(r)h\Delta s \tag{6.18b}$$

It can be seen that, in contrast to the deflection of a hanging chain in a gravitational field, a generic pressure causes a force component in the radial direction. This force component is a function of the local pitch angle φ with the segment normal. Furthermore, the additional centrifugal forces are proportional to the radial distance r from the rotation axis and only appear in the radial force equation. Dividing both equations by Δr and taking the limit $\Delta s \to 0$, while using again the arc length equation, Eq.

(6.8), gives

$$\frac{\mathrm{d}}{\mathrm{d}r}\big(T\cos\varphi\big) = -(p(r)\,h\sin\varphi + \tau A\,\omega_{\mathrm{D}}^2 r)\big(1+w'^2\big)^{\frac{1}{2}} \tag{6.19a}$$

$$\frac{\mathrm{d}}{\mathrm{d}r}\big(T\sin\varphi\big) = \quad p(r)\,h\cos\varphi\big(1+w'^2\big)^{\frac{1}{2}} \tag{6.19b}$$

Using elementary trigonometric relations, the $\sin\varphi$ and $\cos\varphi$ expressions can be written as

$$\cos\varphi = \quad \left(1+\left(\frac{\mathrm{d}w}{\mathrm{d}r}\right)^2\right)^{-\frac{1}{2}} = \big(1+w'^2\big)^{-\frac{1}{2}} \tag{6.20a}$$

$$\sin\varphi = \frac{\mathrm{d}w}{\mathrm{d}r}\left(1+\left(\frac{\mathrm{d}w}{\mathrm{d}r}\right)^2\right)^{-\frac{1}{2}} = w'\big(1+w'^2\big)^{-\frac{1}{2}} \tag{6.20b}$$

Introducing the previous relations into Eqs. (6.19) gives

$$\frac{\mathrm{d}}{\mathrm{d}r}\Big(T\big(1+w'^2\big)^{-\frac{1}{2}}\Big) = -\Big(p(r)\,hw'\big(1+w'^2\big)^{-\frac{1}{2}} + \tau A\,\omega_{\mathrm{D}}^2 r\Big)\big(1+w'^2\big)^{\frac{1}{2}} \tag{6.21a}$$

$$\frac{\mathrm{d}}{\mathrm{d}r}\Big(Tw'\big(1+w'^2\big)^{-\frac{1}{2}}\Big) = \quad p(r)\,h\big(1+w'^2\big)^{-\frac{1}{2}}\big(1+w'^2\big)^{\frac{1}{2}} \tag{6.21b}$$

Expanding the left-hand side, while introducing the centrifugal force coefficient $C_{\mathrm{CF}} = \tau A\,\omega_{\mathrm{D}}^2$ to simplify the equations, gives

$$T'\big(1+w'^2\big)^{-\frac{1}{2}} - Tw'w''\big(1+w'^2\big)^{-\frac{3}{2}} = -p(r)\,h\,w' - C_{\mathrm{CF}}\,r\,\big(1+w'^2\big)^{\frac{1}{2}} \tag{6.22a}$$

$$T'w'\big(1+w'^2\big)^{-\frac{1}{2}} + Tw''\big(1+w'^2\big)^{-\frac{1}{2}} - Tw'^2w''\big(1+w'^2\big)^{-\frac{3}{2}} = \quad p(r)\,h \tag{6.22b}$$

Solving Eq. (6.22a) for T' then yields

$$T' = -p(r)\,h\,w'\big(1+w'^2\big)^{\frac{1}{2}} - C_{\mathrm{CF}}\,r\,\big(1+w'^2\big) + Tw'w''\big(1+w'^2\big)^{-1} \tag{6.23}$$

So collecting second-order derivative terms in Eq. (6.22b) returns

$$w''\Big[\big(1+w'^2\big)^{-\frac{1}{2}} - w'^2\big(1+w'^2\big)^{-\frac{3}{2}}\Big] = \frac{p(r)\,h}{T} - \frac{T'}{T}w'\big(1+w'^2\big)^{-\frac{1}{2}} \tag{6.24}$$

and thus the ODE system can be written as

$$T' = -p(r)hw'\left(1+w'^2\right)^{\frac{1}{2}} - C_{\mathrm{CF}}\, r\left(1+w'^2\right) + Tw'w''\left(1+w'^2\right)^{-1} \tag{6.25a}$$

$$w'' = \frac{p(r)h}{T}\left(1+w'^2\right)^{\frac{3}{2}} - \frac{T'}{T}w'\left(1+w'^2\right) \tag{6.25b}$$

Furthermore, inserting Eq. (6.25b) in Eq. (6.25a) to eliminate w'' in the first equation, it can be shown that

$$T' = -C_{\mathrm{CF}}\, r \tag{6.26}$$

Finally, by inserting Eq. (6.26) into Eq. (6.25b), the ODE system for a generic pressure distribution $p(r)$ with centrifugal forces can be written as

$$w'' = \frac{p(r)h}{T}\left(1+w'^2\right)^{\frac{3}{2}} + \frac{C_{\mathrm{CF}}}{T}w'\, r\left(1+w'^2\right) \tag{6.27a}$$

$$T' = -C_{\mathrm{CF}}\, r \tag{6.27b}$$

In the case of a non-spinning reflector disk, thus $C_{\mathrm{CF}} = 0$, the tangential tension T is constant along r, according to Eq. (6.27b). Therefore, Eq. (6.27a) simplifies to

$$w'' = \frac{p(r)h}{T_0}\left(1+w'^2\right)^{\frac{3}{2}} \tag{6.28}$$

When comparing Eq. (6.28) with the classical gravity catenary, Eq. (6.9), it is clear that the two systems are not the same, and thus, a different shape of the deflection curve due to a generic pressure distribution is anticipated. In Section 6.3, this ODE system will be compared to the system obtained for a uniform SRP load, which is derived in the following section.

6.2.3 Deflection due to solar pressure and centrifugal forces

The deflection model is now modified by replacing the generic pressure load $p(r)$, as shown in Fig. 6.6(b), with a uniform vertical SRP load (normal to the undeflected reflector plane). The SRP force acting on the reflector film is calculated using the simplified SRP model, as described in Section 2.2.2. In the following, the incoming photons are assumed parallel to the spacecraft's spin axis vector $\hat{\mathbf{w}}$, while the spacecraft is orbiting at a constant solar distance. Furthermore, a constant reflectivity $\rho(r) = 1$ is chosen across the reflector film, which simplifies Eq. (2.7) to

$$p_{\mathrm{SRP}} = 2p_0^* \cos^2 \varphi \tag{6.29}$$

where $p_0^* = p_0\big(R_{\mathrm{S},0}/R_\mathrm{S}\big)^2$ is the SRP scaled by the inverse square-law of solar distance. Note that in Eq. (6.29) the cone angle α has been replaced by the local pitch angle φ of the deflected surface. Previously, α denoted the angle of the hoop plane normal towards the Sun, which is assumed to be always zero throughout this analysis.

Considering again a small curve segment Δs, the forces acting on the segment are now described by the SRP force vector

$$\Delta\mathbf{F}_\mathrm{SRP} = -2p_0^* \cos^2\!\varphi \, h\Delta s\,\mathbf{n} \tag{6.30}$$

with $\mathbf{n}$ the local normal to the segment. The centrifugal force vector $\Delta\mathbf{F}_\mathrm{CF}$ is still described by Eq. (6.16). When further introducing the trigonometric relation in Eq. (6.20a) for $\cos\varphi$ into Eq. (6.29) gives

$$p_\mathrm{SRP} = 2p_0^*\big(1+w'^2\big)^{-1} \tag{6.31}$$

The resulting ODE system can now be derived by replacing the generic pressure load $p(r)$ in Eq. (6.27) with the SRP load p_SRP in Eq. (6.31). Accordingly, the new ODE system can be written as follows

$$w'' = \frac{2p_0^* h}{T}\big(1+w'^2\big)^{\frac{1}{2}} + \frac{C_\mathrm{CF}}{T} w'\, r\big(1+w'^2\big) \tag{6.32a}$$

$$T' = -C_\mathrm{CF}\, r \tag{6.32b}$$

In the case of a non-spinning reflector disk, thus $C_\mathrm{CF} = 0$, the tangential tension T is constant along r, according to Eq. (6.32b). Therefore, Eq. (6.32a) simplifies to

$$w'' = \frac{2p_0^* h}{T_0}\big(1+w'^2\big)^{\frac{1}{2}} \tag{6.33}$$

Comparing Eq. (6.33) to the ODE of the classical catenary, Eq. (6.9), shows that, remarkably, both ODEs are the same, apart from the constant gravity force coefficient $a_\mathrm{G} = T_0/(\tau g A)$, which is replaced by the new SRP force coefficient $a_\mathrm{SRP} = T_0/(2p_0^* h)$ in Eq. (6.33). Note that, according to the ODE system found for a generic pressure distribution, Eq. (6.27), any other distribution $p(r)$ would not lead to the same result.

The ODE system of Eq. (6.32) can be solved as BVP on the interval $I = [a, b]$, with $a = 0$ at the centre of the circular reflector film and $b = R$ at the supported edge. Assuming a hinged support at the edge, the BCs are

$$w(R) = 0, \qquad w'(0) = 0, \qquad T(0) = T_0 \tag{6.34}$$

However, an analytical solution cannot be found and the BVP is therefore solved numerically, using the same MATLAB$^{\mathrm{TM}}$ *bvp4c* routine as previously in Chapter 5. For a non-spinning disk, T_0 can again be computed from Eq. (6.14) when replacing a_{G} by a_{SRP}. However, for the spinning case, T_0 cannot be obtained analytically. Therefore, a continuation approach on the spin rate ω_{D} is adopted. Starting from the solution for the non-spinning case, ω_{D} is gradually increased to its final value through $\omega_{\mathrm{D,j+1}} = \omega_{\mathrm{D,j}} + \Delta\omega_{\mathrm{D}}$ where the solution of step j is used as initial guess for step $j+1$. In order to create a converging solution of the BVP for each continuation step, the spin rate has to be increased using appropriate increments, e.g. $\Delta\omega_{\mathrm{D}} = 1\,\mathrm{deg/s}$.

6.2.4 Parabolic reference deflection

In order to compare the resulting deflection curves with an ideal parabolic profile, a reference parabola needs to be defined first. Its curve must be of equal total arc length, since it results from the same reflector film suspended from a rigid hoop of the same diameter. Assuming a generic parabolic deflection curve (subscript p) and its derivatives along the radial direction r

$$w_{\mathrm{p}} = a_{\mathrm{p}} r^2 + b_{\mathrm{p}} r + c_{\mathrm{p}} \tag{6.35a}$$

$$w'_{\mathrm{p}} = 2a_{\mathrm{p}} r + b_{\mathrm{p}} \tag{6.35b}$$

$$w''_{\mathrm{p}} = 2a_{\mathrm{p}} \tag{6.35c}$$

and considering a vertical symmetric load distribution, thus $w'_{\mathrm{p}}(0) = 0$, the coefficient b_{p} is zero. The constant coefficient c_{p} represents the deflection value at the centre, thus

$$c_{\mathrm{p}} = w_0 \tag{6.36}$$

Inserting Eq. (6.35b) into the arc length equation, Eq. (6.8), and integrating, yields

$$S_{\mathrm{p}} = \int_0^R \sqrt{1 + w'^2_{\mathrm{p}}}\,\mathrm{d}r = \frac{1}{2} r \sqrt{1 + 4a_{\mathrm{p}}^2 r^2} + \frac{1}{4a_{\mathrm{p}}} \sinh^{-1}(2a_{\mathrm{p}} r) + C_{\mathrm{p}} \tag{6.37}$$

which enables calculation of the coefficient a_{p}, once the slack arc length S_{p} of the film material is selected. From the condition $S_{\mathrm{p}}(0) = 0$ it follows that $C_{\mathrm{p}} = 0$. The resulting constraint equation

$$\frac{1}{2} R \sqrt{1 + 4a_{\mathrm{p}}^2 R^2} + \frac{1}{4a_{\mathrm{p}}} \sinh^{-1}(2a_{\mathrm{p}} R) \overset{!}{=} S_{\mathrm{p,tot}} \tag{6.38}$$

can be solved numerically for the coefficient a_p, after specifying the total parabolic curve length $S_\mathrm{p,tot}(R)$. The BC at the edge, $w(R) = 0$, finally returns the coefficient

$$c_\mathrm{p} = -a_\mathrm{p} R^2 \tag{6.39}$$

From this, the reference parabola is now completely defined as

$$w_\mathrm{p} = a_\mathrm{p}\big(r^2 - R^2\big) \tag{6.40}$$

According to Eq. 6.40, the parabolic shape equation depends on the hoop radius and the parabolic coefficient, which is a function of the string's arc length, as seen from Eq. 6.38.

6.3 Results

The resulting nominal deflection profiles are presented in this section. For all load cases, a rigid hoop of radius $R = 100\,\mathrm{m}$ and a slack length of $S = 105\,\mathrm{m}$ (from hoop to centre) is used. The string is modelled using polyimide Kapton (see Section 1.1.2) with thickness $t = 2.5\,\mu\mathrm{m}$, according to Fig. 6.4. The deflection profiles for vertical gravity and for a uniform pressure distribution $p(r) = 2p_0^*$ are shown in Fig. 6.7. The profiles are compared to a reference parabola with the same slack length S_p. As can be seen in the figure, the solution considering uniform pressure is more displaced towards the outer hoop and shows a smaller central deflection than the classical gravity catenary. This is due to the horizontal component of the pressure load along the curve. For the classic catenary, this horizontal component is zero. The shape of the ideal parabolic deflection curve is very similar to the classical catenary, as noted in Section 6.2.1. The parabolic deflection is smaller towards the outer regions, compared to the other load cases, while its central deflection is larger. The tension force distribution along the r-axis for all three load cases is shown in Fig. 6.8.

In the following, the effect of varying the slack length on the deflection is investigated. A reflector hoop radius of 100 m is used again for all cases. The deflection curves due to uniform SRP for slack lengths $S := [101, 102, 103, 104, 105, 106]\,\mathrm{m}$ are shown in Fig. 6.9. For comparison, the curves for each corresponding reference parabola are also shown. As expected, the deflection magnitude increases with increasing slack length and can be as large as 30 m at the centre for $S = 106\,\mathrm{m}$. As will be discussed in Section 6.5, a larger central deflection results in a smaller focal length of the reflector disk. According to Fig. 6.9, all deflections due to SRP are no ideal paraboloids, as indicated through

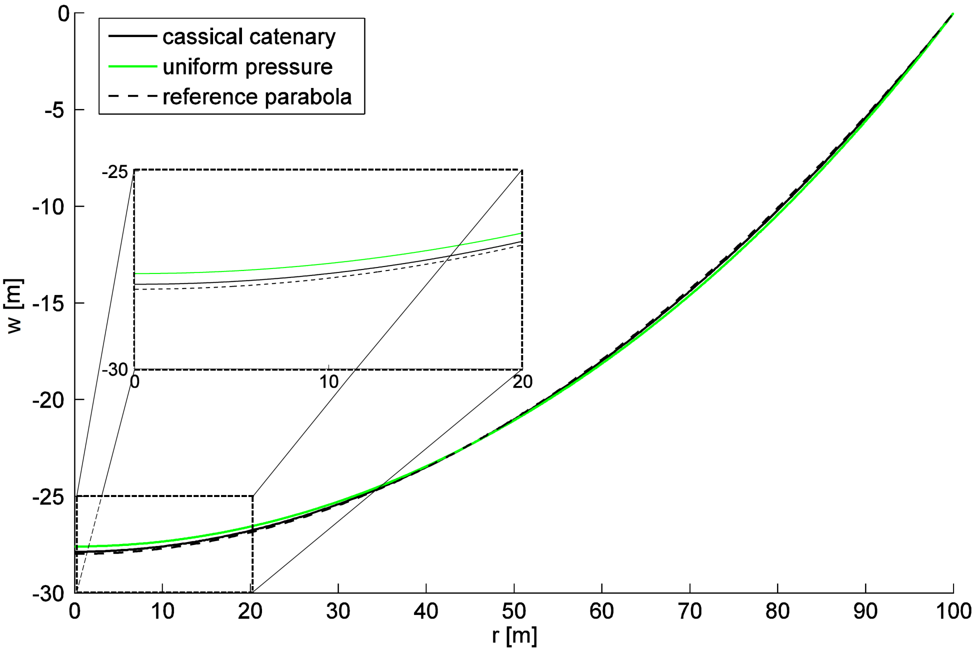

Figure 6.7: Comparison of deflection due to gravity (classical catenary) and uniform pressure and parabolic reference curve, for hoop radius $R = 100\,\mathrm{m}$ and slack length $S = 105\,\mathrm{m}$ (from hoop to centre)

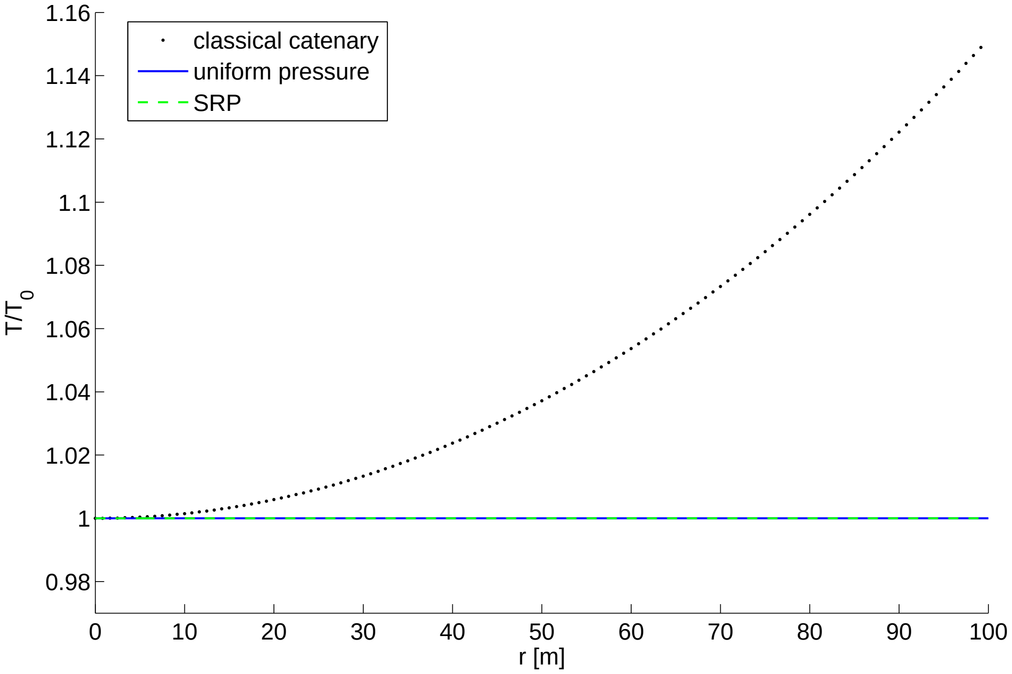

Figure 6.8: Resulting tension force for different load cases: gravity (classical catenary), uniform pressure and uniform SRP (non-spinning reflector disk), for hoop radius $R = 100\,\mathrm{m}$ and slack length $S = 105\,\mathrm{m}$

the dashed parabolic reference curves for each value of S. However, the difference is smaller for smaller slack length.

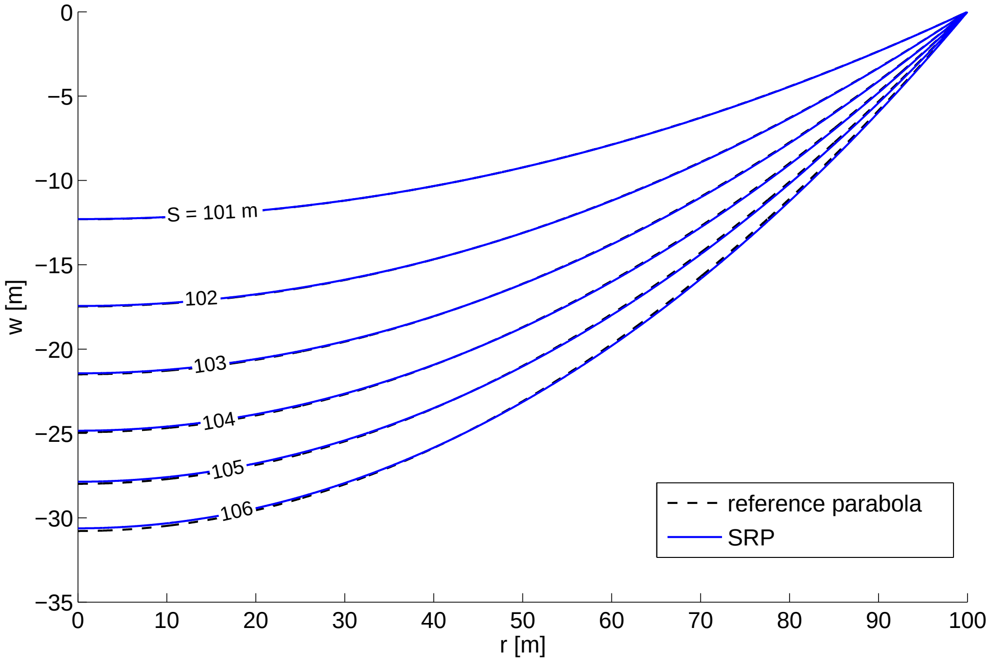

Figure 6.9: Comparison of deflection due to uniform SRP (non-spinning reflector disk) for different slack lengths S (hoop radius R = 100 m) and parabolic reference curves

Figure 6.10 shows the resulting deflection shapes for a spin-stabilised reflector disk with rates $\omega_\mathrm{D} = 0, 20, 30$ and $40\,\mathrm{deg/s}$. The slack length is again $S = 105\,\mathrm{m}$ with a hoop radius of $R = 100\,\mathrm{m}$. As can be seen, the centrifugal force pushes the reflector

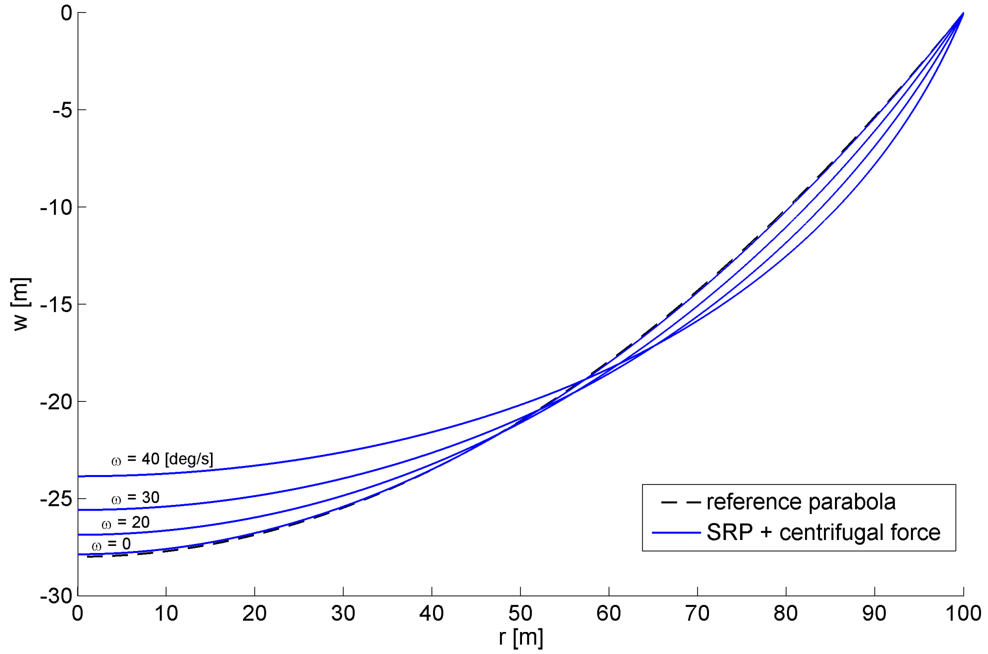

Figure 6.10: Comparison of deflection due to uniform SRP for different spin rates ω_D, using hoop radius $R = 100\,\mathrm{m}$ and slack length $S = 105\,\mathrm{m}$

film material away from the spin axis, causing an increased displacement towards the outer regions, while at the same time reducing the central deflection. Hence, the effect of a spinning reflector film is to shift the deflected profile further away from the ideal parabolic deflection, as indicated by the dashed curve in the figure, thus increasing the effect of SRP. This means that, in order to counteract non-parabolic shape errors, the cumulated effect of SRP and centrifugal forces has to be accounted for.

6.4 Shape control using variable reflectivity distribution

In this section, the deflection shape is controlled by varying the surface reflectivity, in order to create parabolic shapes useful for employing the spacecraft as a large antenna, telescope or power collector. Therefore, the previously defined parabolic reference curve, Eq. (6.40), shall now be generated by modulating the SRP load distribution across the string. For this purpose, an inverse problem, similar to the approach in Section 5.3.1 is formulated. It is defined as finding the necessary reflectivity function $\rho(r)$ that creates a given deflection curve. In doing so, the constant reflectivity ρ in the SRP equation, Eq. (2.7), is again replaced by a generic reflectivity function $\rho(r)$ that varies across the reflector surface as

$$p_{\mathrm{SRP}}(r) = p_0^*(1+\rho(r)) \tag{6.41}$$

The reflectivity is constrained to be within the interval $\rho = [0, 1]$, as introduced in Section 2.2.2. Using Eq. (6.41), the ODE system of Eq. (6.32) modifies into

$$w'' = \frac{p_0^* h(1+\rho(r))}{T}\big(1+w'^2\big)^{\frac{1}{2}} + \frac{C_{\mathrm{CF}}}{T} w'\, r\big(1+w'^2\big) \tag{6.42a}$$

$$T' = -C_{\mathrm{CF}}\, r \tag{6.42b}$$

with $C_{\mathrm{CF}} = \tau A\, \omega_{\mathrm{D}}^2$ denoting again the centrifugal force coefficient. Inserting the reference parabola, Eq. (6.35b) and 6.35c, into Eq. (6.42a) and solving for the unknown reflectivity function, results as

$$\rho(r) = \frac{2a_{\mathrm{p}}T_{\mathrm{p}}}{p_0^* h}\Big(1+(2a_{\mathrm{p}}r)^2\Big)^{-\frac{1}{2}} - \frac{2a_{\mathrm{p}}C_{\mathrm{CF}}\, r^2}{p_0^* h}\Big(1+(2a_{\mathrm{p}}r)^2\Big)^{\frac{1}{2}} - 1 \tag{6.43}$$

with $T_\mathrm{p}(r)$ now being the (unknown) tension force that corresponds to the parabolic displacement. In order to find an expression for T_p, Eq. (6.42b) is integrated as

$$T_\mathrm{p} = -\frac{1}{2} C_\mathrm{CF}\, r^2 + T_\mathrm{p,0} \tag{6.44}$$

Inserting into Eq. (6.43) yields

$$\rho(r) = \frac{a_\mathrm{p}}{p_0^* h}\left[2T_\mathrm{p,0} - C_\mathrm{CF}\, r^2\Big(3 + (2a_\mathrm{p} r)^2\Big)\right]\Big(1 + (2a_\mathrm{p} r)^2\Big)^{-\frac{1}{2}} - 1 \tag{6.45}$$

When further considering the reflectivity constraint at the edge of the disk, $\rho(R) = 0$, the unknown tension $T_\mathrm{p,0}$ can be computed from Eq. (6.45) as

$$T_\mathrm{p,0} = \frac{p_0^* h}{2a_\mathrm{p}}\Big(1 + (2a_\mathrm{p} r)^2\Big)^{\frac{1}{2}} + \frac{1}{2} C_\mathrm{CF}\, R^2\Big(3 + (2a_\mathrm{p} R)^2\Big) \tag{6.46}$$

Inserting this equation back into Eq. (6.45) yields the reflectivity distribution that creates a parabolic deflection curve as

$$\rho(r) = \left(\frac{1 + (2a_\mathrm{p} R)^2}{1 + (2a_\mathrm{p} r)^2}\right)^{\frac{1}{2}} + \frac{a_\mathrm{p} C_\mathrm{CF}}{p_0^* h}\Big(1 + (2a_\mathrm{p} r)^2\Big)^{-\frac{1}{2}}\Big[3(R^2 - r^2) + 8a_\mathrm{p}(R^4 - r^4)\Big] - 1 \tag{6.47}$$

Equation 6.47 is a function of the hoop radius R and the parabolic coefficient a_p and thus, the slack length S, according to Eq. (6.38). The distribution further depends on the centrifugal force coefficient C_CF, thus on the chosen material in terms of density τ and cross section A, and the spin rate ω_D of the disk. Note that Eq. (6.47) is also a function of the solar distance, as can be seen through the coefficient p_0^* in Eq. (6.29).

For a non-spinning reflector disk, $C_\mathrm{CF} = 0$, the required reflectivity distribution simplifies to

$$\rho(r) = \left(\frac{1 + (2a_\mathrm{p} R)^2}{1 + (2a_\mathrm{p} r)^2}\right)^{\frac{1}{2}} - 1 \tag{6.48}$$

which shows that in the special case of a non-spinning reflector disk, the necessary reflectivity distribution to create a parabolic deflection depends on the hoop radius R and a_p only, with the latter being a function of the chosen value of slack length S. In particular, Eq. (6.48) does not depend on the solar distance, as it was found previously for the spin-stabilised case. This indicates that the reflectivity distribution can be prefabricated into the film, as could be seen also in Eq. 5.31 for the elastic membrane case. The reflectivity distributions, according to Eq. (6.48), are shown in Fig. 6.11, for different slack lengths S. The resulting surface reflectivities are promising in terms of

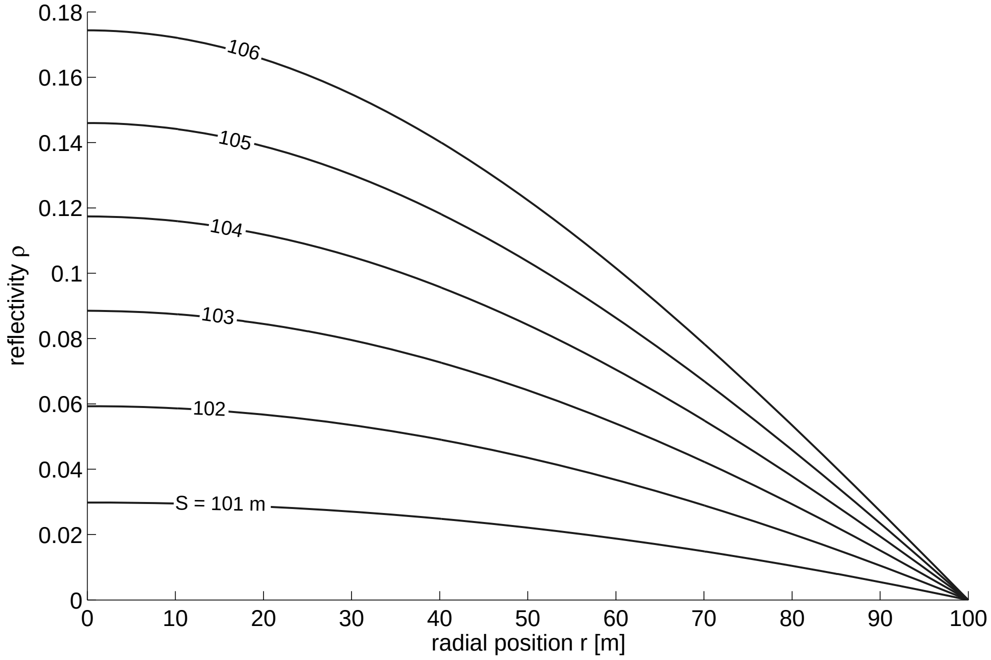

Figure 6.11: Required reflectivity distribution across reflector surface, creating parabolic film deflection (slack length $S = 105\,\mathrm{m}$)

their required magnitude, less than $\rho = 0.2$ even for high values of S, since achieving high surface reflectivities through electro-chromic coatings is generally more demanding (see Section 2.4). To validate the results in Fig. 6.11, the modified ODE system of Eq. (6.42) has been solved with the required reflectivity distribution for the non-spinning disk. The resulting deflection curve indeed matches the reference parabola, as can be seen in Fig. 6.12.

In the case of a spin-stabilised reflector disk, the possibility of creating a parabolic deflection profile strongly depends on the magnitude of the spin rate. The centrifugal forces always increase the deflection away from the ideal parabolic profile, as shown previously in Fig. 6.10. Since the reflectivity, and thus the achievable SRP force magnitudes to counteract this distortion from the parabolic shape, is limited to $\rho \in [0, 1]$, a maximum spin rate that can still be controlled into a parabolic profile is anticipated. In order to find the maximum spin rate $\omega_{\mathrm{D,lim}}$ for a given reflector, the reflectivity function, Eq. (6.47), is solved for ω_{D}. In addition, the maximum reflectivity is assumed to be at the centre of the disk, thus $\rho(0) = 1$. When further considering the minimum reflectivity constraint at the edge of the disk, $\rho(R) = 0$, the allowed maximum spin rate is found to be

$$\omega_{\mathrm{D,lim}} = \left(\frac{1}{\tau A} \left[1 - \frac{2}{\left(1 + (2a_{\mathrm{p}}R)^2\right)^2} \right] \frac{6 a_{\mathrm{p}} p_0^* \left(1 + (2a_{\mathrm{p}}R)^2\right)^2}{1 - \left(1 + (2a_{\mathrm{p}}R)^2\right)^{3/2} (1 + 12 a_{\mathrm{p}}^2 R^2)} \right)^{1/2} \tag{6.49}$$

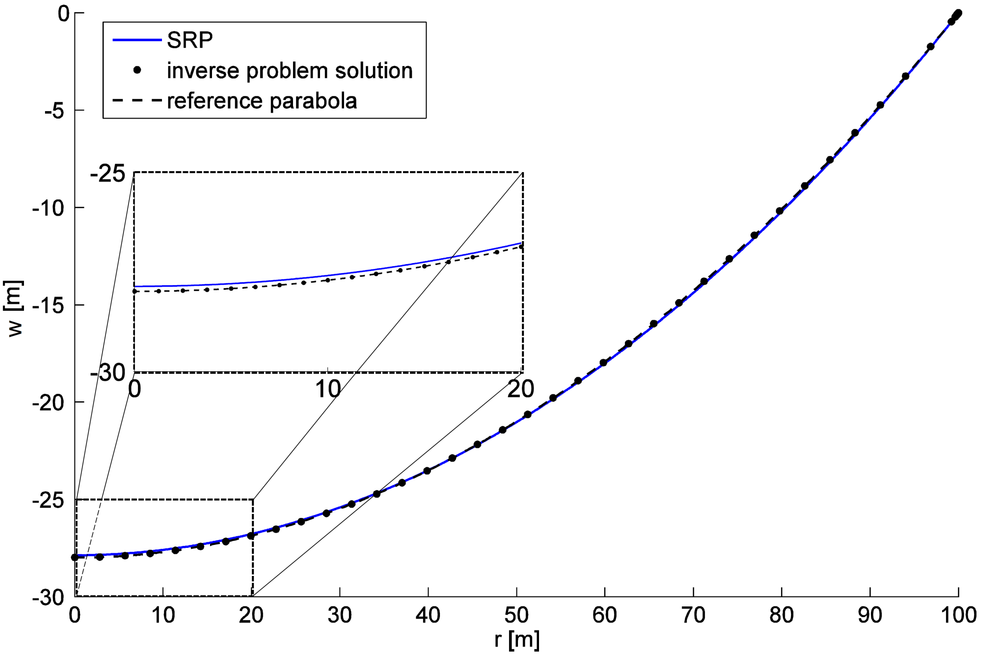

Figure 6.12: Deflection profiles due to uniform SRP (non-spinning reflector disk), inverse problem solution and parabolic reference curve for hoop radius $R = 100\,\mathrm{m}$ and slack length $S = 105\,\mathrm{m}$

The maximum spin rate is a function of the hoop radius R, the parabolic coefficient a_{p} and thus, the slack length S, and the chosen material in terms of density τ and cross section A. Therefore, the maximum allowed spin rate to achieve a parabolic deflection is fully defined for given reflector properties. Figure 6.13 shows the maximum spin rate as a function of the reflector disk radius and for different slack lengths. For example, the maximum spin rate for a reflector of radius $R = 100\,\mathrm{m}$ and $S = 105\,\mathrm{m}$ is found to be $\omega_{\mathrm{D,lim}} = 16.46\,\mathrm{deg/s}$. The corresponding reflectivity distributions for different spin rates, according to Eq. (6.47), are shown in Fig. 6.14. As can be seen, for spin rates above $\omega_{\mathrm{D,lim}} = 16.46\,\mathrm{deg/s}$, the required distribution exceeds $\rho = 1$ towards the centre of the disk, which is physically not possible.

In general, typical angular rates for spin-stabilised space structures such as solar sails are more likely to be smaller than the identified limit case. For example, a spin-stabilised 76×76 m square sail with a spin rate of $0.45\,\mathrm{deg/s}$ was selected for the NASA/JPL Geostorm mission concept study [60, 120]. This rate was found to be sufficient to always keep the sail surface perpendicular to the Sun within 1 deg to the Sun/sail line. In the case of a circular sail design, the selected sail area would correspond to a disk of radius $R \approx 43\,\mathrm{m}$. As can be seen in Fig. 6.13, the maximum spin rate in order to control the film into a parabolic deflection profile is between $40-70\,\mathrm{deg/s}$, depending on the diameter of the slack length. This limit is significantly larger than the

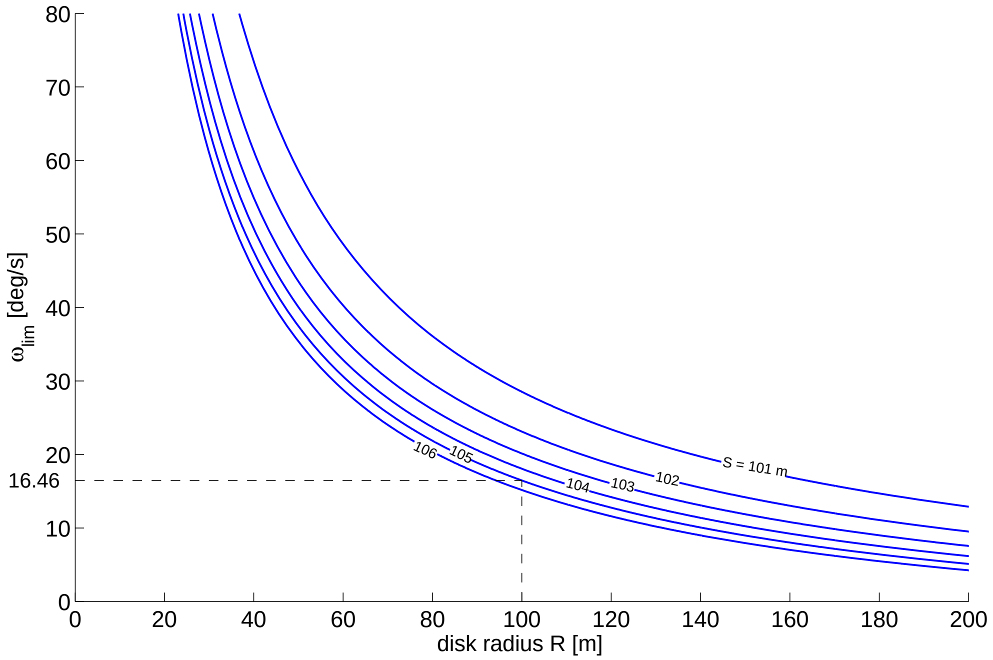

Figure 6.13: Maximum possible spin rate as a function of reflector hoop radius *R* and slack length *S*

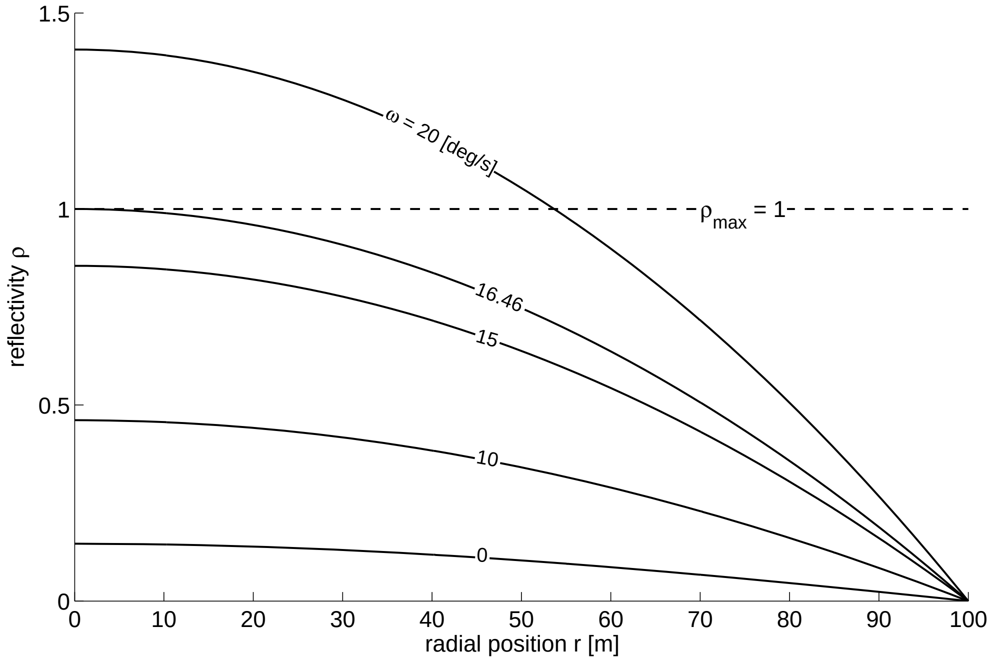

Figure 6.14: Reflectivity distributions for various spin rates, using hoop radius $R = 100\,\mathrm{m}$ and slack length $S = 105\,\mathrm{m}$. For the chosen reflector dimensions, the maximum spin rate such that a parabolic deflection can be created is $\omega_{\mathrm{D,lim}} = 16.46\,\mathrm{deg/s}$

selected spin rate for the proposed Geostorm sail. As a further example, the IKAROS sail with a 14×14 m square sail membrane was spin-stabilised at a nominal rate between $6-15\,\mathrm{deg/s}$ to maintain a flat sail surface [58]. Therefore, also the IKAROS spin rate is within the feasible spin rate interval to create a parabolic deflection.

6.5 Optical performance of slack parabolic reflector

In order to compare the parabolic shapes found in this chapter with the deflected membrane profiles in Chapter 5, the achievable focal lengths are now calculated, assuming an extension of the 1D model into 2D. According to Eq. (5.34), the focal length of the slack catenary surface can be calculated as

$$f = \frac{1}{4a_\mathrm{p}} = \frac{R^2}{4|w_0|} \tag{6.50}$$

when considering the quadratic coefficient $a_\mathrm{p} = -c_\mathrm{p}/R^2 = -w_0/R^2$, as discussed in Section 6.2.4. Thus, the focal length is a function of hoop radius R and central deflection w_0. The latter depends on the chosen slack film radius, as seen in Fig. 6.9. The focal lengths are calculated for a set of rigid hoop radii $R_i := [1, 5, 10, 25, 50, 100]$ m, each suspending a reflector film of varying slack radius $S_i := [101, 102, 103, 104, 105, 106]$ per cent of all R_i, where the spacecraft is assumed to be non-spinning and at a distance of 1 AU from the Sun. For each case, the nominal deflection profile due to uniform SRP is corrected through a non-uniform reflectivity distribution, according to Eq. (6.48), to generate an ideal paraboloid surface shape. The resulting focal lengths for all deflected profiles are shown in Fig. 6.15.

All focal lengths are below 200 m distance from the reflector surface. Previous results for tensioned elastic membranes subject to controlled SRP loads were in the kilometre range of focal length for the same surface diameters, according to Chapter 5, showing a significant improvement with the slack inextensible approach in this chapter. It can be seen in Fig. 6.15 that for all investigated slack film radii, a larger hoop radius increases the focal length. However, when suspending more material from the supporting hoop structure, the focal length decreases. Theoretically, by controlling the amount of film suspended in between the rigid outer hoop, for example through attaching the reflective film to cable rolls inside the hoop, the focal length can also be controlled during the mission.

As shown previously in Chapter 5.4.1, the finite size of the solar disk causes a beam spread in the focal plane, which reduces the efficiency of the surface in terms of, for

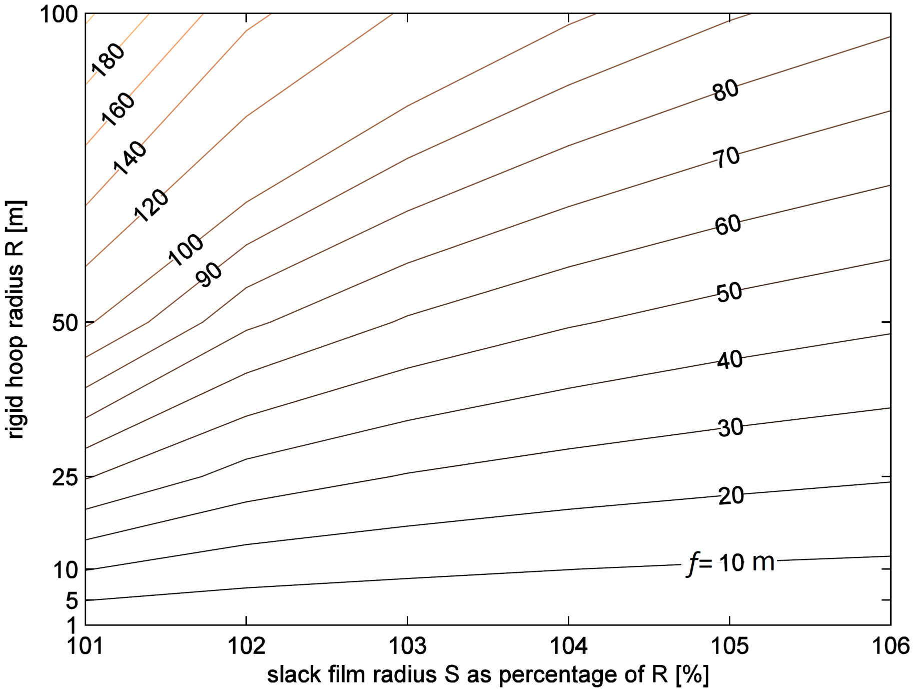

Figure 6.15: Focal lengths of deflected parabolic surface as a function of reflector hoop radius R (non-spinning) and slack film radius S at 1 AU

example, solar power collection. The beam width further depends on the focal length of the collector, according to Eq. 5.37. Therefore, employing a slack surface with much smaller focal lengths should improve the aperture efficiency. For example, considering again a focal length $f_{\text{Kapton}} = 7.54$ km, calculated in Section 5.4 for an elastic membrane reflector of $R = 100$ m radius at Earth distance from the Sun, the beam width was found to be $b_{\text{w},100} = 70.14$ m. Assuming the same hoop radius, the focal length of a slack suspended surface would only be about $f_{\text{slack}} = 100$ m. Accordingly, the beam width in the focal plane would only be $b_{\text{w,slack}} = 0.93$ m, with a concentration ratio $C_{\text{r,slack}} \approx 46,000$. Such a large increase in the optical performance clearly supports the concept of controlled surface billowing demonstrated in this chapter.

Since ultra-thin films are very susceptible to wrinkling, the feasibility of employing a slack suspended surface for the proposed applications still has to be investigated. Wrinkles cause multiple reflections of solar photons on the surface, which reduces the optical quality of the surface and potentially induces thermal peaks in the material. Although it has been demonstrated in this chapter that the available SRP loads are sufficient to allow for controlled (parabolic) billowing of the film, it is not clear whether the induced in-plane tensions will counteract wrinkles due to stowing/folding during launch or during the deployment of the surface.

6.6 Chapter Summary

In this chapter, a non-uniform reflectivity distribution across the surface of a thin slack circular film has been considered to investigate the shape control of slack suspended surfaces using modulated SRP. In this model, the film has been approximated as a 'cob-web' of one-dimensional slack radial strings, suspended from a rigid hoop. Initially, the nominal deflection profiles due to gravity, generic pressure and SRP have been calculated semi-analytically, by solving the coupled equations of inextensible catenary-type string deflection. It has been demonstrated that SRP is the only pressure distribution which yields the classical gravity catenary profile. Using different slack lengths of the string, it has been shown that the nominal deflection shapes due to light pressure are expected to be non-parabolic. When including centrifugal forces for a spin-stabilised reflector disk, the deflection profiles deviate even further from the ideal parabolic shape, thus controlling the spin rate cannot be exploited to generate parabolic surfaces.

Instead, an analytical expression for the reflectivity distribution across the modelled string, necessary to create a true parabolic deflection profile, has been derived. For a non-spinning disk, the expression obtained does not depend on the solar distance and is only a function of the hoop radius and slack length. Therefore, the required reflectivity function across the reflector could be pre-fabricated into the film surface, instead of using electro-chromic coatings. In the case of a spin-stabilised reflector spacecraft, the maximum spin rate that can still be controlled into a parabolic shape has been calculated as a function of reflector dimensions and material properties.

Assuming an extension of the 1D model to a real 2D surface, the focal lengths of the resulting paraboloids have been derived for different hoop radii and slack lengths and are typically below two hundred metres. Comparing the results with the elastic case of a tensioned membrane (Chapter 5), the achievable focal distances are one order of magnitude smaller.

Conclusions

In this final chapter, the research objectives of the thesis will be reviewed and the conclusions in response to the research objectives stated in Section 1.2 will be discussed. In addition, possible future research directions will be recommended.

Summary and conclusions

Optical attitude control of gossamer spacecraft

The first research objective of this thesis considered the investigation of the use of solar radiation pressure (SRP) to control the attitude of large gossamer spacecraft through the manipulation of their surface reflectivity. First, this concept has been demonstrated for a long-baseline tethered dumbbell formation in a combined gravity and SRP force field in a planar circular Sun-centred orbit. It has been shown that introducing SRP to the tip masses creates new unstable equilibria that are different from those of the pure gravity gradient dumbbell. In particular, by controlling the surface reflectivity of the two masses in the decoupled attitude problem, equilibria at an arbitrary angle, relative to the local vertical, have been presented. Furthermore, optical control of the unstable dumbbell attitude has been demonstrated through changing the surface reflectivity. Introducing SRP forces to the system perturbs the circular Keplerian motion of the spacecraft around the central body. Therefore, the coupling of the orbit and attitude dynamics has been reintroduced by deriving constraints for the surface reflectivity, showing that the dumbbell can be maintained on a circular non-Keplerian orbit for arbitrary attitudes using light pressure. The results obtained for the pure gravity gradient dumbbell suggest that for unequal masses and tether lengths up to the same order of magnitude as the orbit semi-major axis, unstable equilibria can be created also without SRP. Despite the theoretical nature of such configurations for planet- and Sun-centred orbits, however, for orbits centred around an asteroid, the tether length would only have to be in the range of a few kilometres.

The second research objective comprised an assessment of different reflectivity distributions across the surface of a large gossamer spacecraft. To this aim, three different distribution models, of increasing complexity, have been considered for a large (ideally rigid) membrane reflector. First, a linear reflectivity distribution along one of the in-plane axes has been employed, while keeping the reflectivity constant along the other in-plane axis. For the case where the resulting optical torques are used to compensate for the gravity-gradient torque acting on the membrane reflector in a circular LEO, the coefficients of the linear reflectivity distribution have been derived analytically. This scheme has been applied successfully to maintain the structure in a Sun-pointing attitude in LEO.

Second, a more complex model of two constrained regions of high and low reflectivity, separated by a controlled boundary line, has been employed. This reflectivity distribution has been shown to create a wide range of torques in the membrane plane, depending on the slope and position of the boundary line on the surface. Through this model, two degrees of freedom attitude control about the two in-plane spacecraft axes has been achieved. Since the SRP force magnitude depends on the membrane's attitude with respect to the Sun, an analytic control scheme has been derived that maintains a constant SRP torque during attitude manoeuvres by moving the boundary line across the surface. This scheme has been successfully applied to changing the membrane's attitude from an arbitrary initial attitude and angular rate to a Sun-pointing attitude.

In the third model, a discrete array of reflectivity control devices (RCDs) across the membrane surface has been considered. Each cell can maintain two states, either 'on' (high reflectivity) or 'off' (low reflectivity). The resulting discrete torques have been calculated for a given reflector size, and as a function of the number, position and activation state of the coating elements. For example, a (4×4)-array of reflectivity cells comprises $65,536$ reflectivity combinations, which reduce to 376 unique (discrete) torques in the membrane plane, after applying suitable truncation laws. In light of the third research objective, this optical control model has been applied to the same attitude manoeuvre as for the second model: from an arbitrary initial attitude and initial rate to a Sun-pointing attitude. To this end, a quaternion-based control scheme has been developed, which controls the reflectivity combinations across the membrane surface. Despite the limited number of discrete torques that can be generated with a small number of reflectivity cells (e.g. a (4×4)-array), the controller is able to execute the manoeuvre successfully, showing a good agreement between the available optical array torques and the reference torques computed by the feedback controller.

Conclusively, optical attitude control through variable SRP forces has been demonstrated to be a novel means for steering a large membrane reflector. By not relying on conventional attitude systems such as thrusters and reaction wheels, the concept of optical attitude control in principle introduces a lightweight attitude control method for large gossamer spacecraft, reducing the overall system mass, and thereby launch cost.

Optical shape control of gossamer spacecraft

The first research objective associated with optical shape control of large gossamer spacecraft required the investigation of the effect of SRP loads on the surface shape of large membrane structures. To this aim, the deflection of a thin circular membrane reflector, supported by a rigid hoop structure and exposed to vertical SRP loads (perpendicular to the membrane surface) have been derived. The equations of non-linear elastic membrane theory have been employed to calculate the nominal deflection profile due to a uniform light pressure distribution for various membrane diameters and solar distances in a Sun-centred orbit. The results indicated a cubic polynomial deflection curve, showing that the deflected surface does not naturally concentrate incoming light into a single focal point due to non-parabolic distortion.

Considering the second research objective, the manipulation of the nominal membrane deflection has been investigated by controlling the reflectivity across the surface. A closed-form solution for the reflectivity function across the membrane required to create a true parabolic deflection shape has been derived. As for the vertical SRP load cases investigated, this reflectivity function does not depend on membrane size, thickness or solar distance. Therefore, rather than using thin-film RCDs, the required reflectivity distribution can be prefabricated into the film surface, saving the additional mass of the coating elements. However, this would also be less flexible during the mission, considering the potential of RCDs for attitude control during manoeuvre phases, as demonstrated in this thesis. Although the required reflectivity distribution does not change with solar distance, the absolute deflection of the membrane does. An analytical expression has been derived for this absolute deflection at the centre of the membrane for a given diameter, film thickness, material properties and solar distance.

Regarding the final research objective, the potential of optical shape control has been investigated in terms of the absolute membrane deflection and focal length of the parabolic membrane. All absolute membrane deflections using a $2.5\,\mu$m Kapton film have been found to be smaller than 0.6 m, even for relatively large membranes (up to 200 m in diameter) and close to the Sun (half the Sun-Earth distance), while no initial in-plane tension has been accounted for to maximise the deflection. In general, the central deflection due to SRP and for all elastic membranes investigated is below one percent of the aperture radius. The focal length of the largest membrane is 7.54 km at the Earth's distance from the Sun. This focal length can be reduced to 6.11 km when employing Mylar films with a currently achievable thickness of only 0.9 μm.

Achieving focal lengths in the kilometre range imposes ambitious requirements on the relative position of an emitter/receiver unit in the aperture focus. Most likely, a detached platform will be required, which flies in formation with the main reflector spacecraft. For this reason, an alternative concept to reduce the focal length has been investigated. The resulting analyses have followed the same research objectives as before.

In particular, instead of using a tensioned elastic membrane, shape control of a slack suspended surface using modulated SRP has been investigated. For this, the film has been approximated as a 'cobweb' (or parachute) of one-dimensional slack radial strings, suspended from a rigid hoop. This analogy allowed a semi-analytic investigation of the surface deflection subject to various distributed loads, while centrifugal forces for a spin-stabilised reflector disk have also been considered.

By solving the coupled equations of inextensible string (or 'catenary') deflection, it has been demonstrated that SRP is the only pressure distribution that yields the classical gravity catenary deflection, and is therefore non-parabolic. The profiles for both load cases follow the same hyperbolic-cosine law.

When including centrifugal forces for a spin-stabilised reflector disk, the deflection profiles deviate even further from an ideal parabolic shape, thus controlling the spin rate cannot be exploited to generate parabolic surfaces.

Instead, an analytical expression for the reflectivity distribution across the modelled string, necessary to create a true parabolic deflection profile, has been derived. For a non-spinning disk, the expression found does not depend on the solar distance and is only a function of the hoop diameter and slack length. Again, this indicates that the required reflectivity function could be pre-fabricated into the film surface. In case of a spin-stabilised reflector spacecraft, it has been shown that a maximum spin rate exists at which the membrane can still be controlled into a parabolic shape.

Assuming an extension of the 1D string model to a real 2D surface, the focal lengths of the achievable parabolic surfaces have been obtained for a range of hoop diameters and slack lengths. For all investigated hoop sizes up to 200 m in diameter and slack lengths up to 212 m, the focal lengths are below two hundred meters. Comparing the results with the elastic case of a tensioned membrane, the achievable focal distances are one order of magnitude smaller. In terms of the emitter/receiver unit in the aperture focus, the results indicate that the platform can be physically connected with the main reflector, instead of operating a detached unit flying in formation with the spacecraft.

Lastly, optical shape control through variable SRP forces has been demonstrated to be a novel means to create parabolic surface deflections of large membrane reflectors. Potentially, this allows the membrane to be used as a multifunctional device for a range of communications, sensing and science applications.

Future research

The research presented in this thesis has demonstrated the potential of using modulated SRP for optical attitude and shape control of large gossamer spacecraft. Therefore, this thesis supports the ongoing engineering effort to realise ultra-lightweight low-cost technology concepts for a range of future space applications. In order to complement or improve the current results, additional analyses are considered below.

In general, the SRP model employed throughout this thesis is valid under the assumption of an ideal, specular reflecting, surface. In addition, when modulating the reflectivity, using the simplified SRP model, the remaining fraction of photons *not* undergoing specular reflection are assumed to be simply absorbed without re-emission. However, a real surface would scatter this fraction of light in the form of diffuse reflection, and thus, generating an additional SRP force fraction normal to the surface. Furthermore, due to the force contribution from the impinging photons, this results in an in-plane component of the total SRP force acting on the real surface. This could have an impact on the optical torques created and also on the deflection magnitudes of the membrane.

Optical attitude control

The analyses presented in this thesis for a tethered formation in the combined gravity and SRP force field have been constrained to planar Sun-centred orbits. This investigation could be continued by deriving the three-dimensional orbit/attitude dynamics problem and by considering the control of the configuration around small bodies such as asteroids. Applying optical attitude control to such a scenario could be promising as the ratio of SRP and the gravitational force is much greater and therefore a higher control authority can be achieved. In addition, orbit stabilisation of a tethered solar observatory about a sub-L_1 point for space weather monitoring could be investigated. Positioning the tether system closer to the Sun with respect to a spacecraft at the L_1-

point increases the warning time for a solar storm. Furthermore, a tethered formation could be used for solar observation using long baseline interferometry.

Surface reflectivity modulation has been investigated in this thesis for attitude control of large gossamer membrane spacecraft. In particular, an RCD reflectivity array across the surface of the membrane has been employed to demonstrate the control of the spacecraft attitude without using mechanical systems or thrusters. The discrete torques that can be generated using a square array have been derived from the total number of reflectivity combinations on the array. However, many reflectivity combinations generate the same discrete torque. As a way of reducing the number of combinations to be considered, truncation laws have been defined that select one reflectivity at random to represent that particular discrete torque. However, instead of selecting a viable reflectivity combination, it would be beneficial to select the combination that requires the least amount of active RCD cells to minimise the power required to operate the array. Furthermore, each time the control scheme switches between two combinations on the array, in order to generate the closest-match torque from the set of available torques, the control scheme could be further improved. It could be enabled to choose the combination that requires the least amount of cell switches. Again, such improvements potentially reduce the amount of power required for actuation, especially during times when extended attitude station-keeping is required. In addition, it might be sufficient to implement only larger groups of RCD cells across the surface, which are controlled at once to accomplish specific control tasks. Since this would reduce the level of fine control available, the feasibility strongly depends on the desired application, for example, solar power collection or space communication, and the requirements on station-keeping and pointing accuracy. However, this would reduce the system's complexity and minimise the additional mass introduced to the surface.

Optical shape control

In this thesis, the analyses of optical shape control of the membrane have focussed on vertical load distributions, normal to the undeflected surface. However, this condition is potentially undesirable during operation, especially for applications such as Earth communication and observation. For this reason, future analyses could include unsymmetric load cases and further derive the reflectivity required for a parabolic deflection as a function of light incidence angle. Potentially, such analyses would require finite element modelling (FEM) of the membrane for the general load case. In addition, the elastic membrane could be modelled as a composite membrane, thus considering the thickness of the electro-chromic coatings and different material properties for each individual layer. This would result in a more realistic modelling approach, which aims towards the best possible prediction of the behaviour of the membrane during the mission.

It has been shown in this thesis that the absolute deflection of the parabolic surface, and thus focal length, changes with solar distance. This variation could be compensated for, for example, by a detached receiver/transmitter platform that is flying in formation at the current focus. However, the reflectivity function obtained could potentially be modified to adapt to this condition, i.e. maintain the same parabolic deflection at different solar distances. This could be achieved, for example, by fixing the value of the central deflection of the film in the inverse problem.

Considering the investigation of slack suspended surfaces, the model developed could be extended by considering material in the circumferential direction between the radial strings, thereby considering a real 2D surface. This investigation could be supported by an FEM analysis, as has been conducted previously for a structural analysis of inflated parachutes [121].

With respect to both the attitude and shape control of gossamer spacecraft, the efficiency of optical control compared to other concepts that are currently developed could also be assessed, by considering an analysis on the system level. The analysis would compare mass budget, power consumption and control performance of competing methodologies and actuator systems. Clearly, this investigation has to consider the ongoing development of thin-film RCDs and possibly also ways to distribute thin foldable electric circuits across thin membranes [63]. Polymer-based electrochromic coatings of total thickness below a micrometre, using single-walled carbon nanotubes, have recently been assembled for ultra-thin touch-screen panels [14]. For solar sails in particular, the concept of optical control has the potential to support the technology roadmap for this promising type of low-thrust propulsion.

Further applications of optical control

One of the key objectives of this research was to develop a highly-integrated multi-functional control concept for gossamer membrane spacecraft. Beyond the scope of controlling the attitude and the shape of the reflector, optical control involves further advantages, which depend on the desired application. For example, in terms of solar power collection, controlling the surface reflectivity allows a modulation of the thermal load on the heat engine in the aperture focus. In this case, the RCD cells could be operated in low (diffuse) reflectivity mode instead of having to rotate the reflector away from the Sun, in event of thermal loads being exceeded.

Furthermore, instead of limiting the application of RCDs to the light collecting front of the membrane, the same devices could also be applied to the back of the reflector. This could improve the thermal state of the structure by controlling the emissivity of the far side, hence disposing of excess of thermal energy. In comparison to a black back surface, this could minimise thermal heating in case the back of the membrane is exposed to solar or planetary irradiation.

Finally, in the future, a functional RCD array fabricated on the surface of a membrane spacecraft may comprise 10,000 or even 100,000 individual cells. When operating the array in a communication mode, each cell could be addressed individually to produce one element of a large 'QR code' (a matrix barcode commonly used for product tracking, item identification or commercial marketing). When further pointing the reflector towards, for example, a ground-based optical receiver, digital coding of the RCD array would enable transfer of huge amounts of data through high-speed optical switching.

Appendix

A Quaternion Algebra

In this appendix, some mathematical properties of the quaternion and its usefulness to represent the spacecraft attitude will be explained.

The (four-dimensional) quaternion $\bar{q} = (q_1, q_2, q_3, q_4)^{\mathrm{T}}$ is a hypercomplex number system in the Cartesian basis $(1, \mathbf{i}, \mathbf{j}, \mathbf{k})$ in $\mathbb{R}^4$ [103, 104], with $\mathbf{i} = (1, 0, 0)^{\mathrm{T}}$, $\mathbf{j} = (0, 1, 0)^{\mathrm{T}}$ and $\mathbf{k} = (0, 0, 1)^{\mathrm{T}}$, representing three unit vectors in $\mathbb{R}^3$. The quaternion has the general form

$$\bar{q} = q_1 + q_2\mathbf{i} + q_3\mathbf{j} + q_4\mathbf{k} \tag{A.1}$$

with four real numbers q_i, termed the components of $\bar{q}$, and the upper $(\bar{\ })$ denoting a quaternion vector. Since the subspace $(\mathbf{i}, \mathbf{j}, \mathbf{k})$ represents an orthonormal basis in $\mathbb{R}^3$, the components of the vector $\mathbf{q} = (q_2, q_3, q_4)^{\mathrm{T}}$ can be regarded as the vector component and q_1 as the scalar component of $\bar{q}$. Therefore, $\bar{q}$ represents a mathematically strange object, which is not defined in ordinary linear algebra: the sum or a scalar and a vector [103]. The quaternion number system was first described by the Irish mathematician Sir W. R. Hamilton in 1843.

By convention, the quaternion must satisfy the Euclidean norm of $\bar{q}$ being unity (normalization condition)

$$|\bar{q}| = \sqrt{q_1^2 + q_2^2 + q_3^2 + q_4^2} = \sqrt{q_1^2 + \mathbf{q}^2} = 1 \tag{A.2}$$

The latter constraint implies that only unit quaternions are applicable for attitude descriptions and rotations. Therefore, $\bar{q}$ with $|\bar{q}| = 1$ is called the unit quaternion or normalised quaternion.

The conjugate complex of $\bar{q}$ is defined as

$$\bar{q}^* = q_1 - iq_2 - jq_3 - kq_4 = q_1 - \mathbf{q} \tag{A.3}$$

which is also the inverse quaternion, thus $\bar{q}^* = \bar{q}^{-1}$, for normalised $\bar{q}$ (without derivation). Furthermore, a quaternion with a scalar component $q_1 = 0$ is called a pure quaternion. For example, the vector $\mathbf{p} = (p_1, p_2, p_3)^\mathrm{T}$ is the vector part of the pure quaternion $\bar{p} = (0, p_1, p_2, p_3)^\mathrm{T}$.

The unit quaternion $\bar{q}$ represents an attitude description like the classical rotation matrix or Euler angles. A fundamental theorem explains the characteristics of an attitude quaternion:

Euler's Theorem

A coordinate frame can be brought from an arbitrary initial attitude to an arbitrary final attitude by a single rotation by an angle θ (with $-\pi \leq \theta \leq \pi$) about a single axis of rotation $\mathbf{a}$, which is called the Euler axis [101]. The theorem implies that the axis of rotation $\mathbf{a}$ remains unchanged in both the rotated frame $\mathcal{B}$ and the reference frame $\mathcal{E}$, thus a rotation has no effect on $\mathbf{a}$

$$\mathbf{a}_{\mathcal{B}} = \mathbf{a}_{\mathcal{E}}$$

Figure A.1 shows Euler's Theorem. Assuming that both frames initially have the same attitude (parallel axes), the axis of rotation $\mathbf{a}$ (red) has the same components in $\mathcal{B}$ and $\mathcal{E}$ such as

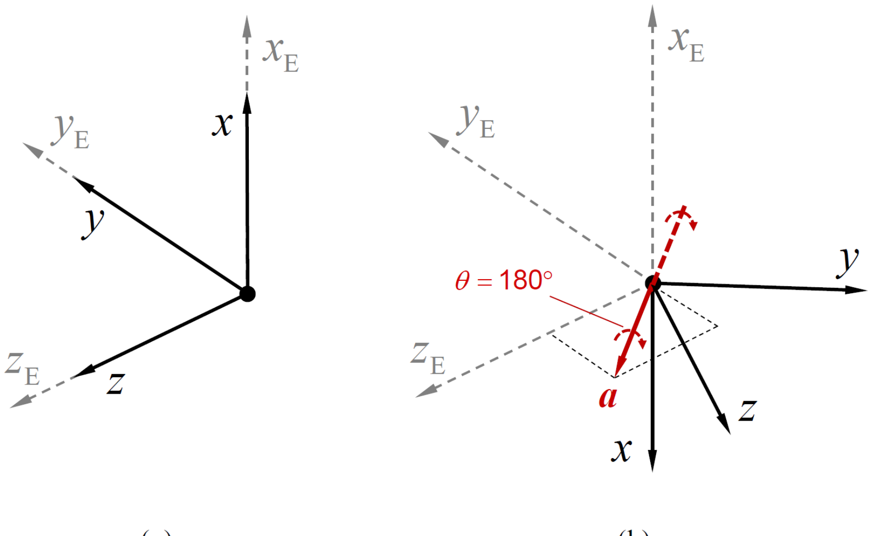

(a) (b)

Figure A.1: Attitude of body frame $\mathcal{B} := (\mathbf{x}, \mathbf{y}, \mathbf{z})$ relative to ecliptic reference frame $\mathcal{E} := (\mathbf{x_E}, \mathbf{y_E}, \mathbf{z_E})$, as described by Euler's Theorem: a) same attitude (left), and b) rotated by the angle $\theta = 180$ deg about Euler axis a (right).

$$(a_\mathrm{x}, a_\mathrm{y}, a_\mathrm{z})^\mathrm{T}_\mathcal{B} = (a_{\mathrm{x_E}}, a_{\mathrm{y_E}}, a_{\mathrm{z_E}})^\mathrm{T}_\mathcal{E}$$

However, from the previous definition of the quaternion $\bar{q}$, according to Eq. A.1, the rotation angle and thus, the quaternion's rotational character, is not directly visible. The following derivation gives a quaternion notation in terms of rotation axis $\mathbf{a}$ and rotation angle θ.

Applying Euler's theorem on $\bar{q} = \mathbf{q} + q_4$, while considering the Euclidean norm

$$|\bar{q}|^2 = |q_1|^2 + |\mathbf{q}|^2 = 1 \tag{A.4}$$

with the Pythagorean theorem $\cos^2\theta + \sin^2\theta = 1$ for a unit circle (and arbitrary angle θ), leads to the relations

$$\begin{aligned} |q_1|^2 &= \cos^2\theta \quad \Rightarrow\ q_1 = \cos\theta \quad \wedge \\ |\mathbf{q}|^2 &= \sin^2\theta \quad \Rightarrow\ |\mathbf{q}| = \sin\theta \end{aligned} \tag{A.5}$$

After defining a unit vector $\mathbf{a}$, which represents the direction of $\mathbf{q}$

$$\mathbf{a} = \frac{\mathbf{q}}{|\mathbf{q}|} = \frac{\mathbf{q}}{\sin\theta} \quad \Rightarrow\ \mathbf{q} = \mathbf{a} \cdot \sin\theta \tag{A.6}$$

the quaternion $\bar{q}$ results as

$$\bar{q} = q_1 + \mathbf{q} = \cos\theta + \mathbf{a} \cdot \sin\theta \tag{A.7}$$

It can be shown that $\bar{q}$ actually represents a rotation by the angle 2θ (without derivation). Therefore, a so-called 'half-angle transformation' is applied to $\bar{q}$

$$\bar{q} = q_1 + \mathbf{q} = \cos\left(\frac{\theta}{2}\right) + \mathbf{a} \cdot \sin\left(\frac{\theta}{2}\right) \tag{A.8}$$

Written in 4-dimensional vector form, the rotational character of a quaternion becomes visible

$$\bar{q} = \begin{pmatrix} q_1 \\ q_2 \\ q_3 \\ q_4 \end{pmatrix} = \begin{pmatrix} \cos(\theta/2) \\ a_x \cdot \sin(\theta/2) \\ a_y \cdot \sin(\theta/2) \\ a_z \cdot \sin(\theta/2) \end{pmatrix} = \begin{pmatrix} q_4 \\ \mathbf{q} \end{pmatrix} = \cos\left(\frac{\theta}{2}\right) + \mathbf{a} \cdot \sin\left(\frac{\theta}{2}\right) \tag{A.9}$$

Therefore, the quaternion $\bar{q}$ represents a single-axis rotation about the axis $\mathbf{a} = (a_x, a_y, a_z)^\mathrm{T}$

by the angle θ, thus

$$\bar{q} = \mathrm{f}(\mathbf{a}, \theta) \tag{A.10}$$

In order to use quaternions for rotation operations such as two consecutive rotations, the product of two quaternions, for example, $\bar{s}$ and $\bar{t}$, is defined as follows [122]

$$\bar{q} = \bar{s} \otimes \bar{t} = (s_1 + s_2\mathbf{i} + s_3\mathbf{j} + s_4\mathbf{k}) \cdot (t_1 + t_2\mathbf{i} + t_3\mathbf{j} + t_4\mathbf{k}) \tag{A.11}$$

In here, $\bar{q}$ is the final attitude obtained after both rotations $\bar{s}$ and $\bar{t}$ have been applied. In other words, the quaternion $\bar{s}$ describes the initial attitude and $\bar{t}$ denotes the attitude change in order to receive the final attitude $\bar{q}$. The mathematical operation given in Eq. A.11 can be translated into matrix form such as

$$\bar{q} = \bar{s} \otimes \bar{t} = \begin{pmatrix} s_1 \cdot t_1 - \mathbf{s} \cdot \mathbf{t} \\ s_1 \cdot \mathbf{t} + t_1 \cdot \mathbf{s} + \mathbf{s} \times \mathbf{t} \end{pmatrix} = \begin{pmatrix} s_1t_1 - s_2t_2 - s_3t_3 - s_4t_4 \\ s_2t_1 + s_1t_2 + s_3t_4 - s_4t_3 \\ s_3t_1 + s_1t_3 + s_4t_2 - s_2t_4 \\ s_4t_1 + s_1t_4 + s_2t_3 - s_3t_2 \end{pmatrix} \tag{A.12}$$

The quaternion product, according to Eq. A.12, can also be used from a different point of view, namely, when comparing two attitudes with a desired reference attitude. For example, this reference attitude can be the Sun-pointing attitude. In this scenario, $\bar{q}$ shall denote the current attitude of the spacecraft-fixed frame $\mathcal{B}$, and $\bar{q}_{\mathrm{ref}}$ shall be the reference attitude. Consequently, the product

$$\bar{q}_{\mathrm{err}} = \bar{q}_{\mathrm{ref}} \otimes \bar{q} \tag{A.13}$$

represents the attitude error between the reference and the current attitude. Therefore, the error quaternion $\bar{q}_{\mathrm{err}}$ describes the attitude of the spacecraft w.r.t. the desired reference attitude. If the Euler axis of $\bar{q}_{\mathrm{err}}$ returns the zero vector, $\mathbf{a} = (0, 0, 0)^{\mathrm{T}}$, the current attitude matches the desired reference attitude.

Bibliography

[1] Crouch T. D. *Wings: a history of aviation from kites to the space age.* WW Norton & Company, 2003. 1

[2] McInnes C. R. *Solar Sailing: Technology, Dynamics and Mission Applications*, pages 121–124. Springer-Praxis Series in Space Science and Technology, Springer-Verlag, Berlin, 1999. 2, 11, 19, 20, 22, 23, 30, 37

[3] Forward R. L. **Gossamer spacecraft survey study. Preliminary report - Historical survey**. Technical report, Forward Unlimited, 18 July 1999 1999. 2

[4] Bastaits R., Rodrigues G., Jetteur P., Hagedorn P., and Preumont A. **Multi-layer adaptive thin shells for future space telescopes**. *Smart Materials and Structures*, **21**(6):064004, 2012. 3

[5] Postman M., Argabright V., Arnold B., Aronstein D., and Atcheson P. et al. **Advanced Technology Large-Aperture Space Telescope (ATLAST): a technology roadmap for the next decade**. *arXiv preprint arXiv:0904.0941*, 2009. 3

[6] Ewing A., Back J., Schuettpelz B., and Laue G. **James Webb Space Telescope Sunshield Membrane Assembly**. In *50th AIAA/ASME/ASCE/AHS/ASC Structures, Structural Dynamics, and Materials Conference, Structures, Structural Dynamics, and Materials and Co-located Conferences, American Institute of Aeronautics and Astronautics, Reston, VA, USA*, 2009. 3

[7] Pellegrino S. **Deployable Membrane Reflectors**. In *2nd World Engineering Congress, Sarawak, Malaysia*, pages 1–9, 2002. 3

[8] Schenk M., Viquerat A. D., Seffen K. A., and Guest S. D. **Review of Inflatable Booms for Deployable Space Structures: Packing and Rigidization**. *Journal of Spacecraft and Rockets*, **51**(3):762–778, 2014. 3

[9] Sakamoto H., Park K. C., and Miyazaki Y. **Evaluation of membrane structure designs using boundary web cables for uniform tensioning**. *Acta Astronautica*, **60**(1011):846–857, 2007. 3, 8

[10] Fang H., Lou M., Huang J., Hsia L., and Kerdanyan G. **Inflatable Structure for a Three-Meter Reflectarray Antenna**. *Journal of Spacecraft and Rockets*, **41**(4):543–550, 2004. 3

[11] Freeland R. E., Bilyeu G. D., Veal G. R., and Mikulas M. M. **Inflatable deployable space structures technology summary**. In *Proceedings of the 49th International Astronautical Congress, Melbourne, Australia*, 1998. IAF-98-1.5.01. 3

[12] Greschik G., Mikulas M. M., and Palisoc A. **Torus-less inflated membrane reflector with an exact parabolic center**. *AIAA Journal*, **42**(12):2579–2584, 2004. 3

[13] Jenkins C.H. (Ed.). *Gossamer spacecraft: membrane and inflatable structures technology for space applications*. Progress in Astronautics and Aeronautics, Vol. 191, American Institute of Aeronautics and Astronautics, Reston, VA, USA, 2001. 3, 4, 8, 10

[14] Wilson A. **A history of balloon satellites**. *Journal of the British Interplanetary Society*, **34**:10, 1981. 3

[15] Freeland R. E., Bilyeu G. D., Veal G. R., Steiner M. D., and Carson D. E. **Large inflatable deployable antenna flight experiment results**. *Acta Astronautica*, **41**(4-10):267–277, 1997. 3

[16] Malone P. K. and Williams G. T. **Lightweight inflatable solar array**. *Journal of Propulsion and Power*, **12**(5):866–872, 1996. 3

[17] Kennedy K. J. **ISS TransHab: Architecture Description**. Technical report, SAE Technical Paper, 1999. 3

[18] Waye D. E., Cole J. K., and Rivellini T. P. **Mars pathfinder airbag impact attenuation system**. In *13th AIAA Aerodynamic Decelerator Systems Technology Conference*, pages 109–119, 1995. 4

[19] Jorgensen J., Louis E., Hinkle J., Silver M., and Zuckermandel B. et al. **Dynamics of an Elastically Deployable Solar Array: Ground Test Model Validation**. In *46th AIAA/ASME/ASCE/AHS/ASC Structures, Structural Dynamics & Materials Conference*, Structures, Structural Dynamics, and Materials and Co-located Conferences. American Institute of Aeronautics and Astronautics, 2005. doi:10.2514/6.2005-1942. 4

[20] Santiago-Prowald J. and Baier H. **Advances in deployable structures and surfaces for large apertures in space**. *CEAS Space Journal*, **5**(3-4):89–115, 2013. 4, 5, 8

[21] Ruggiero E. J. and Inman D. J. **Gossamer spacecraft: Recent trends in design, analysis, experimentation, and control**. *Journal of Spacecraft and Rockets*, **43**(1):10–24, 2006. 4, 11

[22] Quinn D. and Farley R. **Tethered formation configurations - Meeting the scientific objectives of large aperture and interferometric science**. In *AIAA Space*

2001 Conference and Exposition, SPACE Conferences & Exposition. American Institute of Aeronautics and Astronautics, 2001. doi:10.2514/6.2001-4770. 4

[23] Leisawitz D. **NASAs far-IR/submillimeter roadmap missions: SAFIR and SPECS**. *Advances in Space research*, **34**(3):631–636, 2004. 4

[24] Troger H., Alpatov A.P., Beletsky V.V., Dranovskii V.I., and Khoroshilov V.S. et al. *Dynamics of Tethered Space Systems*, pages 1–60. CRC Press/Taylor & Francis Group, Boca Raton, FL, USA, 2010. 4

[25] Pearson J. **The real history of the space elevator**. In *AIAA 57th International Astronautical Congress, IAC 2006*, **13** of *AIAA 57th International Astronautical Congress, IAC 2006*, pages 8723–8729. American Institute of Aeronautics and Astronautics Inc., 2006. 5

[26] Moran J. P. **Effects of Plane Librations on the Orbital Motion of a Dumbbell Satellite**. *ARS Journal*, **31**(8):1089–1096, 1961. 5

[27] Artsutanov Y. **To the Cosmos by Electric Train**. Komsomolskaya Pravda, Leningrad Technological Institute, 1960. 5

[28] Williams J. R. and Adams J. J. **Investigation of Tethered Station Keeping**. Technical Report NASA-TN-D-4258, Langley Research Center, National Aeronautics and Space Administration, 1967. 5

[29] Colombo G., Gaposchkin E.M., and Grossi M.D. et al. **The Skyhook: a Shuttle-borne Tool for Low-orbital-altitude Research**. *Meccanica*, **10**(1):3–20, 1975. 5

[30] Misra A. K. and Modi V.J. **A Survey of the Dynamics and Control of Tethered Satellite Systems**. Proceedings of the NASA/AIAA/PSN International Conference on Tethers in Space, Arlington, VA, USA, pages 667–719, 1986. 5

[31] No T. S. and Cochran Jr J. E. **Dynamics and Control of a Tethered Flight Vehicle**. *Journal of Guidance, Control, and Dynamics*, **18**(1):66–72, 1995. doi:10.2514/3.56658. 5

[32] Wen H., Jin D. P., and Hu H. Y. **Advances in Dynamics and Control of Tethered Satellite Systems**. *Acta Mechanica Sinica*, **24**(3):229–241, 2008. doi.10.1007/s10409-008-0159-9. 5

[33] Forward R. L. **Tether transport from LEO to the lunar surface**. *AIAA/SAE/ASME/ASEE 27th Joint Propulsion Conference, June24-26, 1991, Sacramento, CA, USA*, 1991. doi:10.2514/6.1991-2322. 5

[34] Ziegler S.W. *The Rigid-body Dynamics of Tethers in Space*. PhD thesis, Department of Mechanical Engineering, University of Glasgow, UK, 2003. 5

[35] Sanyal A. K., Shen J., McClamroch N. H., and Bloch A. M. **Stability and Stabilization of Relative Equilibria of Dumbbell Bodies in Central Gravity**. *Journal of Guidance, Control, and Dynamics*, **28**(5):833–842, 2005. doi:10.2514/1.10546. 5

[36] Misra A. K. **Dynamics and Control of Tethered Satellite Systems**. *Acta Astronautica*, **63**(11-12):1169–1177, 2008. 5, 39

[37] Kumar K. D. **Review of Dynamics and Control of Nonelectrodynamic Tethered Satellite Systems**. *Journal of Spacecraft and Rockets*, **43**(4):705–720, 2006. doi:10.2514/1.5479. 5

[38] Cartmell M. P. and McKenzie D. J. **A Review of Space Tether Research**. *Progress in Aerospace Sciences*, **44**(1):1–21, 2008. doi:10.1016/j.paerosci .2007.08.002. 5

[39] Imbriale W.A., Gao S., and Boccia L. *Space Antenna Handbook.* Hoboken: Wiley, 2012. 5

[40] MacEwen H. A. (editor). *Proceedings of SPIE: Highly innovative space telescope concepts*, **4849** of *Proceedings of SPIE - The International Society for Optical Engineering, Bellingham, WA, USA,*. SPIE, 2002. 6

[41] Stimson G. W. *Introduction to Airborne Radar.* SciTech Pub., 1998. 6

[42] Leipold M., Runge H., and Sickinger C. **Large SAR membrane antennas with lightweight deployable booms**. In *28th ESA Antenna Workshop on Space Antenna Systems and Technologies, ESA/ESTEC*, 2005. 6

[43] Roger A. **Future very large space telescopes**. In *Space 2000 Conference and Exposition*, SPACE Conferences & Exposition. American Institute of Aeronautics and Astronautics, 2000. doi:10.2514/6.2000-5304. 6

[44] McClelland D.H. **Solar Concentrators for High Temperature Space Power Systems**. In *Space Power Systems*, Progress in Astronautics and Aeronautics, pages 129–152. American Institute of Aeronautics and Astronautics, 1961. doi:10.2514/5.9781600864780.0129.0152. 6

[45] Cougnet C., Sein E., Celeste A., and Summerer L. **Solar power satellites for space exploration and applications**. In *4th International Conference on Solar Power from Space, SPS '04 - Together with The 5th International Conference on Wireless Power Transmission, WPT 5, June 30, 2004 - July 2, 2004 (ed. H. Lacoste & L. Ouwehand)*, European Space Agency, (Special Publication) ESA SP, pages 151–158. ESA Publications Division, European Space Agency, Noordwyk, The Netherlands, 2004. 6, 7

[46] Gärdsback M. *Deployment control of spinning space webs and membranes.* PhD thesis, Department of Mechanics, Royal Institute of Technology, Stockholm, Sweden, 2008. 6

[47] McInnes C. R. **Space-based geoengineering: Challenges and requirements**. *Proceedings of the Institution of Mechanical Engineers, Part C: Journal of Mechanical Engineering Science*, **224**(3):571–580, 2010. 7

[48] DuPont High Performance Films. **Kapton Technical Data Sheet**, Retrieved 09 April 2014. ”http://www2.dupont.com/Kapton/en_US/ assets/downloads/pdf/HN_datasheet.pdf”. 8

[49] Johnston J. **Finite Element Analysis of Wrinkled Membrane Stuctures for Sunshield Applications**. In *43rd AIAA/ASME/ASCE/AHS/ASC Structures, Structural Dynamics, and Materials Conference*, Structures, Structural Dynamics, and Materials and Co-located Conferences. American Institute of Aeronautics and Astronautics, 2002. doi:10.2514/6.2002-1456. 8

[50] Carey J., Goldstein E., Cadogan D., Pacini L., and Lou M. **Inflatable sunshield in space (ISIS) versus next generation space telescope (NGST) sunshield A mass properties comparison**. In *AIAA Structures, Structural Dynamics and Materials Conference*, 2000. 8

[51] Fang H. and Lou M. **Analytical characterization of space inflatable structures - an overview**. *Collection of Technical Papers - AIAA/ASME/ASCE/AHS/ASC Structures, Structural Dynamics and Materials Conference*, **1**:718–728, 1999. 8

[52] Barton S. A. *A Study of Useful Inflatables.* PhD thesis, Florida State University, 2011. 8

[53] Wright J. L. *Space Sailing.* Gordon and Breach Science Publishers, Philadelphia, 1992. 9

[54] Yamaguchi T., Mimasu Y., Tsuda Y., Takeuchi H., and Yoshikawa M. **Estimation of solar radiation pressure force for solar sail navigation**. In *Proceedings of 61st International Astronautical Congress, Prague, Czech Republic*, 2010. 9

[55] Johnson L., Swartzlander G., and Artusio-Glimpse A. *An Overview of Solar Sail Propulsion within NASA*, Chapter 2, pages 15–23. Springer Praxis Books. Springer Berlin Heidelberg, 2014. 9

[56] Pisacane V. *Fundamentals of Space Systems, 2nd Edition.* Oxford University Press, 2005. 9

[57] Scholz C., Romagnoli D., Dachwald B., and Theil S. **Performance analysis of an attitude control system for solar sails using sliding masses**. *Advances in Space Research*, **48**(11):1822–1835, 2011. 9

[58] Mimasu Y., Yamaguchi T., Matsumoto M., Nakamiya M., Funase R., and Kawaguchi J. **Spinning solar sail orbit steering via spin rate control**. *Advances in Space Research*, **48**(11):1810–1821, 2001. 9, 114

[59] Mettler E., Acikmese A., and Ploen S. *Attitude dynamics and control of solar sails with articulated vanes.* Pasadena, CA: Jet Propulsion Laboratory, National Aeronautics and Space Administration, 2005. 9

[60] Wie B. **Solar sail attitude control and dynamics, part 1**. *Journal of Guidance, Control, and Dynamics*, **27**(4):526–535, 2004. 9, 112

[61] Wie B. **Solar sail attitude control and dynamics, part 2**. *Journal of Guidance, Control, and Dynamics*, **27**(4):536–544, 2004. 9

[62] McInnes C. R. **Delivering fast and capable missions to the outer solar system**. *Advances in Space Research*, **34**(1):184–191, 2004. 10

[63] Siegel A., Phillips S., Dickey M., Lu N., Suo Z., and Whitesides G. **Foldable Printed Circuit Boards on Paper Substrates**. *Advanced Functional Materials*, **20**(1):28–35, 2010. 10, 123

[64] Sinn T., Hilbich D., and Vasile M. **Inflatable shape changing colonies assembling versatile smart space structures**. *Acta Astronautica*, **104**(1):45–60, 2014. 10

[65] Biter W., Hess S., and Oh S. **Development status of electrostatic switched radiator**. In *SPACE TECH. & APPLIC. INT. FORUM-STAIF 2006: 10th Conf Thermophys Applic Microgravity; 23rd Symp Space Nucl Pwr & Propulsion; 4th Conf Human/Robotic Tech & Nat'l Vision for Space Explor.; 4th Symp Space Coloniz.; 3rd Symp on New Frontiers & Future Concepts*, **813**, pages 56–63. AIP Publishing, 2006. 10

[66] Lafleur J. M., Olds J. R., and Braun R. D. **Daedalon: A revolutionary morphing spacecraft design for planetary exploration**. In *1st Space Exploration Conference: Continuing the Voyage of Discovery, Jan 30 - Feb 1*, **2** of *A Collection of Technical Papers - 1st Space Exploration Conference: Continuing the Voyage of Discovery*, pages 1150–1163. American Institute of Aeronautics and Astronautics Inc., 2005. 10

[67] Valasek J. *Morphing Aerospace Vehicles and Structures.* Wiley, 2012. 10

[68] Marker D. and Jenkins C.H. **Surface Precision of Optical Membranes with Curvature**. *Optics Express*, **1**(11):324–331, 1997. 10

[69] Haftka R. T. and Adelman H. M. **An analytical investigation of shape control of large space structures by applied temperatures**. *AIAA Journal*, **23**(3):450–457, 1985. 10

[70] Murphy L.M. and Tuan C. **The formation of optical membrane reflector surfaces using uniform pressure loading**. Technical Report SERI/TR-253-3025, Solar Energy Research Inst., Golden, CO (USA); Nebraska Univ., Lincoln (USA), 1987. 10

[71] Ruggiero E. J. and Inman D. J. **Modeling and vibration control of an active membrane mirror**. *Smart Materials and Structures*, **18**(9):095027, 2009. 10

[72] Patterson K., Pellegrino S., and Breckinridge J. **Shape correction of thin mirrors in a recongurable modular space telescope**. In *Proc. SPIE 7731, Space Telescopes and Instrumentation 2010: Optical, Infrared, and Millimeter Wave, 773121*, pages 773121–773121–12. International Society for Optics and Photonics, 2010. 10

[73] Gaspar J., Mann T., Behun V., Wilkie K., and Pappa R. **Development of Modal Test Techniques for Validation of a Solar Sail Design**. In *45th AIAA/ASME/ASCE/AHS/ASC Structures, Structural Dynamics & Materials Conference*, Structures, Structural Dynamics, and Materials and Co-located Conferences. American Institute of Aeronautics and Astronautics, 2004. doi:10.2514/6.2004-1665. 11

[74] Hill J., Wang K. W., and Fang H. **Advances of Surface Control Methodologies for Flexible Space Reflectors**. *Journal of Spacecraft and Rockets*, **50**(4):816–828, 2013. doi:10.2514/1.a32231. 11

[75] Kornbluh R., Flamm D., Prahlad H., Nashold K., and Chhokar S. et al. **Shape control of large lightweight mirrors with dielectric elastomer actuation**. In *Proc. SPIE 5051, Smart Structures and Materials 2003: Electroactive Polymer Actuators and Devices (EAPAD), 143*, **5051**, pages 143–158. International Society for Optics and Photonics, 2003. doi:10.1117/12.484405. 11

[76] Shirley D. L. **The Mariner 10 mission to Venus and Mercury**. *Acta Astronautica*, **53**(410):375–385, 2003. 11

[77] Mori O., Shirasawa Y., Mimasu Y., Tsuda Y., and Sawada H. et al. **Overview of IKAROS Mission**. In Malcolm Macdonald (editor), *Advances in Solar Sailing*, Springer Praxis Books, pages 25–43. Springer Berlin Heidelberg, 2014. 11, 12, 25

[78] Sohn R. L. **Attitude Stabilization by Means of Solar Radiation Pressure**. *ARS Journal*, **29**(5):371–373, 1959. 11

[79] Robertson R. E. **Radiation Pressure Torques from Spatial Variations in Surface Properties**. *Journal of Spacecraft and Rockets*, **2**(4):605–607, 1965. doi:10.2514/3.28240. 11

[80] Stuck B. W. **Solar Pressure Three-Axis Attitude Control**. *Journal of Guidance, Control, and Dynamics*, **3**(2):132–139, 1980. doi:10.2514/3.55960. 11

[81] Singh S. N. and Yim W. **Nonlinear Adaptive Spacecraft Attitude Control using Solar Radiation Pressure**. *IEEE Transactions on Aerospace and Electronic Systems*, **41**(3):770–779, 2005. doi:10.1109/taes.2005.1541428. 11

[82] Circi C. **Three-Axis Attitude Control using Combined Gravity-Gradient and Solar Pressure**. *Proceedings of the Institution of Mechanical Engineers, Part G: Journal of Aerospace Engineering*, **221**(1):85–90, 2007. doi:10.1243/09544100jaero48. 11

[83] O'Shaughnessy D. J., McAdams J. V., Williams K. E., and Page B. R. **Fire Sail: MESSENGER's use of solar radiation pressure for accurate Mercury flybys**. In *32nd Guidance and Control Conference*, **133**. American Astronautical Society, 2009. 11

[84] Kawaguchi J. and Shirakawa K. **A fuel-free sun-tracking attitude control strategy and the flight results in Hayabusa (MUSES-C)**. In *AAS Flight Mechanics Conference*, pages 07–176, 2007. 11

[85] Macdonald M. and Badescu V. *The International Handbook of Space Technology.* Springer, 2014. 12

[86] Modi V. J. **On the Semi-Passive Attitude Control and Propulsion of Space Vehicles using Solar Radiation Pressure**. *Acta Astronautica*, **35**(23):231–246, 1995. doi:10.1016/0094-5765(94)00271-M. 12

[87] Aliasi G., Mengali G., and Quarta A. A. **Artificial Lagrange Points for Solar Sail with Electrochromic Material Panels**. *Journal of Guidance, Control, and Dynamics*, **36**(5):1544–1550, 2013. 12

[88] Dachwald B. *Low-Thrust Trajectory Optimization and Interplanetary Mission Analysis Using Evolutionary Neurocontrol.* PhD thesis, Universität der Bundeswehr München, Fakultät für Luft- und Raumfahrttechnik, Institut für Raumfahrttechnik, 2003. 24

[89] Mengali G., Quarta A., Circi C., and Dachwald B. **Refined Solar Sail Force Model with Mission Application**. *Journal of Guidance, Control and Dynamics*, **30**(2), 2007. 23

[90] Dachwald B. and Macdonald M. **Parametric Model and Optimal Control of Solar Sails with Optical Degradation**. *Journal of Guidance, Control and Dynamics*, **29**(5), 2006. 24

[91] Demiryont Hulya and Moorehead David. **Electrochromic Emissivity Modulator for Spacecraft Thermal Management**. *Solar Energy Materials and Solar Cells*, **93**(12):2075–2078, 2009. doi:10.1016/j.solmat.2009.02.025. 25

[92] Kanu S. S. and Binions R. **Thin films for solar control applications**. *Proc. R Soc A*, **466**(2113):19–44, 2010. 25

[93] Nikolou M., Dyer A. L., Steckler T. T., Donoghue E. P., and Wu Z. et al. **Dual n- and p-Type Dopable Electrochromic Devices Employing Transparent Carbon Nanotube Electrodes**. *Chemistry of Materials*, **21**(22):5539–5547, 2009. 25

[94] Funase R., Mori O., Tsuda Y., Shirasawa Y., and Saiki T. et al. **Attitude control of IKAROS solar sail spacecraft and its flight results**. In *61st International Astronautical Congress 2010, IAC 2010, September 27 - October 1*, **6**, pages 4720–4725. International Astronautical Federation, IAF, 2010. 26

[95] Ziegler S. W. and Cartmell M. P. **Using Motorized Tethers for Payload Orbital Transfer**. *Journal of Spacecraft and Rockets*, **38**(6):904–913, 2001. doi:10.2514/2.3762. 28

[96] Meyer K., Hall G., and Offin D. *Introduction to Hamiltonian Dynamical Systems and the N-Body Problem*, pages 1–26. Lecture Notes in Computer Science, Springer, Berlin, 2008. 29, 31, 39

[97] Poisson E. *Advanced Mechanics, PHYS*3400*, Chapter 2, pages 47–48. Lecture Notes, Dept. of Physics, University of Guelph, Canada, 2008. 30

[98] Krupa M., Steindl A., and Troger H. **Stability of Relative Equilibria. Part II: Dumbbell Satellites**. *Meccanica*, **35**(4):353–371, 2001. doi:10.1023/a:1010327717603. 32

[99] Hirsch M.W., Smale S., and Devaney R.L. *Differential Equations, Dynamical Systems, and an Introduction to Chaos*, pages 159–188. Academic Press/Elsevier, San Diego, 2004. 32

[100] Inampudi R. K. *Two-Craft Coulomb Formation Study about Circular Orbits and Libration Points.* Ph.D. Thesis, Department of Aerospace Engineering Sciences, University of Colorado, 2010. 36

[101] Schaub H. *Analytical Mechanics of Space Systems, 2nd Edition.* AIAA Educational Series, 2009. 46, 56, 57, 126

[102] Borggräfe A. *Analysis of Interplanetary Solar Sail Trajectories with Attitude Dynamics.* Master Thesis, Institute of Flight System Dynamics, RWTH Aachen University, Germany, 2011. 56, 57

[103] Kuipers J. *Quaternions and Rotation Sequences.* Princeton University Press, 1999. 56, 57, 125

[104] Hanson A. *Visualizing Quaternions.* Morgan Kaufmann, 2006. 56, 125

[105] Bettis D.G. *A Runge-Kutta Nyström Algorithm.* Celestial Mechanics 8. Kluwer Academic Publishers, 1973. 57

[106] Shampine L.F., Gladwell I., and Thompson S. *Solving ODEs with MATLAB*, pages 134–143. Cambridge University Press, 2003. 68, 79

[107] Fresk E. and Nikolakopoulos G. **Full quaternion based attitude control for a quadrotor**. In *European Control Conference (ECC), July 17-19, Zürich, Switzerland*, pages 3864–3869, 2013. 69

[108] Timoshenko S. and Woinowsky-Krieger S. *Theory of Plates and Shells*, Chapter 13, pages 396–428. McGraw-Hill, 1959. 76

[109] Ventsel E. and Krauthammer T. *Thin Plates and Shells: Theory, Analysis, and Applications*, pages 355–358. Taylor & Francis, 2001. 77, 79

[110] Craig R.R. *Mechanics of Materials.* John Wiley & Sons, 2011. 77

[111] Voorthuyzen J. A. and Bergveld P. **The influence of tensile forces on the deflection of circular diaphragms in pressure sensors**. *Sensors and Actuators*, **6**(3):201–213, 1984. 77

[112] Sheplak M and Dugundji J. **Large Deflections of Clamped Circular Plates Under Initial Tension and Transitions to Membrane Behavior**. *Journal of Applied Mechanics, Transactions ASME*, **65**(1):107–115, 1998. 77, 79

[113] Couceiro F., Gamboa P. V., Silva J. M., and Guerman A. D. **Configuration of a thin circular membrane subject to solar pressure**. In *2012 International Conference on Spacecraft Structures, Materials and Mechanical Testing, ICSSMMT 2012, December 27, 2012 - December 28, 2012*, **290** of *Applied Mechanics and Materials*, pages 47–52. Trans Tech Publications, 2013. 79, 80

[114] Sleight D. W. and Muheim D. M. **Parametric studies of square solar sails using finite element analysis**. In *Collect. of Pap. - 45th AIAA/ASME/ASCE/AHS/ASC Struct., Struct. Dyn. and Mater. Conf.; 12th AIAA/ASME/AHS Adapt. Struct. Conf.; 6th AIAA Non-Deterministic Approaches Forum; 5th AIAA Gossamer Spacecraft Forum, April 19, 2004 - April 22, 2004*, **1** of *Collection of Technical Papers - AIAA/ASME/ASCE/AHS/ASC Structures, Structural Dynamics and Materials Conference*, pages 85–97. American Inst. Aeronautics and Astronautics Inc., 2004. 80, 81

[115] DuPont Teijin Films. **Innovative Polyester Films Brochure**, Retrieved 19 November 2013. "http://europe.dupontteijinfilms.com/Download .aspx?pdfid=147". 88

[116] Gill E., D'Amico S., and Montenbruck O. **Autonomous formation flying for the PRISMA mission**. *Journal of Spacecraft and Rockets*, **44**(3):671–681, 2007. 88

[117] Wikipedia: The Free Encyclopedia. 2013 Wikimedia Foundation Inc. **Spider Web**, Retrieved 05 July 2013. "http://upload.wikimedia.org/wikipedia/commons/f/fb/Spider Catenary.jpg". 96

[118] Aoyanagi Y. and Okumura K. **Simple Model for the Mechanics of Spider Webs**. *Physical Review Letters*, **104**(3):038102, 2010. 95

[119] Lockwood E.H. *A Book of Curves*, Chapter 13 - The Tractrix and Catenary, pages 118–124. Cambridge University Press, 1961. 97, 99, 100

[120] West J. L. **Solar sail vehicle system design for the Geostorm Warning Mission**. In *American Institute of Aeronautics and Astronautics, Space 2000 Conference and Exposition,Long Beach, California, USA*, 2000. "http://hdl.handle.net/2014/15866". 112

[121] Lu K., Accorsi M., and Leonard J. **Finite element analysis of membrane wrinkling**. *International Journal for Numerical Methods in Engineering*, **50**(5):1017–1038, 2001. 123

[122] Sidi M. *Spacecraft Dynamics and Control: A Practical Engineering Approach*, Chapter Appendix A, Attitude Transformations in Space, pages 325–326. Cambridge University Press, 2000. 128